

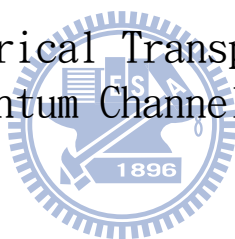
國立交通大學

電子物理系

博士論文

介觀量子通道與開放量子點之電性傳輸

Electrical Transport in
Mesoscopic Quantum Channels and Open Dots



研究生：劉凱銘

指導教授：許世英

中華民國九十九年八月

介觀量子通道與開放量子點之電性傳輸

Electrical Transport in
Mesoscopic Quantum Channels and Open Dots

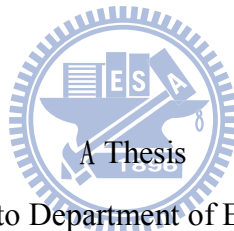
研究生：劉凱銘

Student: Kai-Ming Liu

指導教授：許世英

Advisor: Shih-Ying Hsu

國立交通大學
電子物理學系
博士論文



Submitted to Department of Electrophysics

College of Science

National Chiao Tung University

in partial Fulfillment of the Requirements

for the Degree of

Doctor of Philosophy

in

Electrophysics

August 2010

Hsinchu, Taiwan, Republic of China

中華民國九十九年八月

介觀量子通道與開放量子點之電性傳輸

學生：劉凱銘

指導教授：許世英

國立交通大學電子物理學系博士班

摘 要

在介觀系統裡元件的尺寸接近電子的平均自由路徑與同調性長度，因而量子現象得以彰顯。在這個尺度下，不同的物理與電性傳輸能夠經由不同的元件設計來展現與探討。本論文描述了包含多種不同元件的四組電性量測。結果顯現出元件的物理特性，如結構、長度與電子密度，對於電性傳輸的影響。第一組實驗揭示了電子-電子交互作用對於準一維量子線中著名的零偏壓異常的重要性。量測著重在不同通道長度與電子密度的量子線、電導值小於 $2e^2/h$ 的源汲極偏壓能譜圖(source drain bias spectroscopy)與隨溫度變化的線性電導。電子-電子交互作用對傳輸的影響預期因為量子線通道長度變長或密度降低而增大，而實驗結果顯示 ZBA 的高度與寬度也隨之減小。此外從不同溫度的數據所得到的特徵值與零偏壓異常的寬度呈現出比例關係，這個結果指出電子背向散射是形成零偏壓異常極其重要的原因。在第二組實驗裡，我們探討了在一維通道中雜質對於電子傳輸的影響。側向移動量子通道的技巧與重覆升降溫被運用來改變無序量子通道中雜質的分佈。由於雜質的存在造成量子線的線性電導出現扭曲的階梯與共振振盪，也造成源汲極偏壓能譜圖出現複雜的結構。能譜圖展現出分裂的雙峰結構，但可隨著雜質分佈的改變而逐漸演變單峰結構；這樣的結構很容易與零偏壓異常混淆。但是數據顯示，其能譜圖的變化是來自於雜質所導致的束縛態而非乾淨的準一維通道的固有傳輸特徵。在第三組實驗裡，兩個獨立但同步化的時變電場被用來擾動一開放性量子點。在無外加直流偏壓下，該電場在兩種電路組態-電荷抽運與整流-中產生直流電流。其電流與電場之間的相位差呈現正弦的關係。但不同電路組態下產生的電流對於電場的頻率、環境的耦合與磁場的響應亦有所差異。數據顯示該兩組電流並非由電路效應，如信號耦合或是串擾所造成；而不同的物理機制能由不同的電路組態來分辨。最後一個實驗探討電子連續經過兩個串聯量子接點的傳輸。我們針對兩點電導與直接穿透率(direct transmission)隨電子密度與量子接點間的距離的變化來討論。直接穿透率反應出通過兩量子接點的電流中，電子仍具有同調性的比例。隨著電子密度的降低或是距離的增加，彈道式傳輸逐漸變成歐姆性傳輸，而同時直接穿透率則降至趨近於零。實驗結果印證理論預期——兩個量子系統間的同調性與否決定電子是否能夠以彈道式傳輸通過兩個系統。

Electrical Transport in Mesoscopic Quantum Channels and Open Dots

student : Kai-Ming Liu

Advisors : Dr. Shih-Ying Hsu

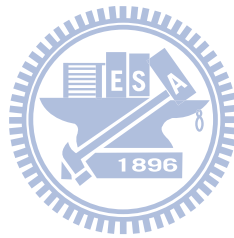
Department of Electrophysics
National Chiao Tung University

Abstract

In mesoscopic regime where the device dimension is comparable to electron mean free path and coherence length, quantum mechanical features manifest. In this regime, different transport characteristics and physics can be revealed by different device designs and arrangements. This dissertation presents four experiments for assortment of devices that evidence the influence of physical properties of devices on the electrical transport.

In the first experiment, the importance of electron-electron interactions on the prominent Zero Bias Anomaly (ZBA) in quasi one dimensional quantum wires (QWs) is verified. Source-drain bias spectroscopy and temperature dependent differential conductance at zero-bias in the range of $G < 2e^2/h$ are demonstrated for a range of wire length and carrier density. The amplitude and width of the ZBA decrease with either decreasing carrier density or increasing channel length, wherein the scattering rate of electrons is expected to increase due to enhanced electron-electron interaction. In addition, the thermal energy scales to the width of ZBA that reveals the essence of electron backscattering. In the second experiment, the influences of impurity on the transport in quasi 1D channel are demonstrated. Lateral shifting technique, imposing an offset between gate voltages applied on a pair of split gates, along with thermal cycling is exploited to vary the impurity arrangement in disordered QWs. Impurity causes distortions and resonances in linear conductance and leads to complicated source-drain bias spectroscopy. The nonlinear conductance presents splitting peaks which resolve back into a single peak with varying gate voltage. This feature may be confusing with the inherent ZBA of QWs, but the result indicates that it is due to resonant states

caused by impurities. In the third experiment, dc currents of an open dot generated from two time dependent electric fields in the absence of external bias are studied. Two different electrical setups, charge pump and rectification respectively, were applied to produce the currents. The frequency, environmental coupling, and magnetic field dependences of the dc currents bear little resemblance in response to the different electrical configurations. The two types of currents are indicated to be produced from different mechanisms but not from classical circuitry effects and can be distinguished. In the final experiment, two-terminal conductance and direct transmitting probability across double quantum point contacts (QPCs) are investigated regarding their dependences on carrier density and separation distance. The transport evolves from being ballistic to being classically ohmic as the carrier density is reduced or the separation is increased and the direct transmission probability decreases correspondingly. The results demonstrate that ballistic transport across two quantum systems depends on coherence in between.



Acknowledgement

For the past years in my graduate research, I have witnessed the growth of knowledge and skills in nanofabrication and electrical measurement for mesoscopic physics in this laboratory. Beginning from scratch, the apparatuses were set up one by one. On this odyssey the impediments would be unconquerable without the support from many people. First of all, I have to thank my father for his financial support and his patience bearing me for staying in school for such a long time. I also deeply from my heart thank my family, **Shu-Yan**, **Jiun-Reng**, **Tung-Lin**, and **Ting-Chi** for their encouragement when I was demoralized. I would not forget the advices given by **Ming-Li** that prompted me to be perseverant. Their backing mobilized me in the research work. As for the nanofabrication, Dr. **Jong-Chin Wu** in National Changhua University provided helpful information and technical guidelines. Much of the lithographic know-how was inherited from his group. His support gave the foundation for our advancement. I am thankful for Dr. **Chon-Saar Chu** that he provided invaluable theoretical support. He is gentle and modest, but every question brought up by him was critical and have urged me to ponder more thoroughly. In the consultation with him, I have learned much about physics as well as writing. In the collaboration with Dr. **Tzay-Ming Hong** and **Jen-Hao Hsiao** in National Tsing Hua University, the discussions have stimulated new ideas and deeper physical insights. I am grateful for the collaborations with **Hsin-Yi Lin** and **Sheng-Hao Juang** who help to make the experiments more efficient and productive. **Ting-Yi Chung** shared six years with me in the same laboratory. His gentleness and humor always soothed tension among the coordinating. He brought laughs when toughness of works was at hand. It is my pleasure working with him. I would like to thank my advisor **Shih-Ying Hsu** who alone wrote for grant and managed the bothersome budgets. She prepared all required apparatuses and was eager seeking supports when additional resource was required. I also thank her for providing the freedom to explore different aspects of physics. The research would never be possible without Dr. **Vladimir Umansky**'s precious heterostructure wafers. For those people who have helped me directly or indirectly but are forgotten to mention here, it is my fault. Finally, I thank god that he let me be buffeted and confronted, but at the same time taught me lessons about life.

Electrical Transport in Mesoscopic Quantum Channels
and Open Dots



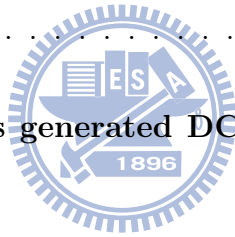
Kai-Ming, Liu

August, 2010

Contents

List of figures	iv
List of tables	viii
1 Introduction	1
1.1 Two dimensional electron gas (2DEG)	2
1.2 Diffusive transport versus ballistic transport	4
1.3 One Dimensional Transport	4
1.3.1 Two-terminal and four-terminal conductances of 1D conductors	4
1.3.2 Quantum point contacts and quantum wires	6
1.3.3 Nonequilibrium transport in quantum wires	9
1.4 Zero dimensional transport-closed quantum dot	10
1.5 Organization of this dissertation	12
2 Experimental techniques	15
2.1 Device fabrications	15
2.2 Measurements	17
2.3 Cryostats	18
2.4 Magnet and dewar	20
3 Zero-bias anomaly and conductance reduction in quantum wires	21
3.1 Introduction	21
3.2 0.7 structure and zero bias anomaly	21
3.3 Physical pictures	23

3.3.1	Spontaneous spin polarization	24
3.3.2	Kondo-type interaction	28
3.3.3	Inelastic backscatterings	31
3.4	Device arrangements	34
3.5	Density and length dependences of the ZBA	34
3.6	The conductance reduction at finite temperatures and biases	40
3.7	Conclusions	44
4	Conductance and spectroscopy of disordered quantum wires	45
4.1	Introduction	45
4.2	Transport features in the presence of impurities	46
4.3	Disordered quantum wires and position controlling	50
4.4	Results and discussion	52
4.5	Conclusions	59
5	Time dependent electric fields generated DC currents in a large gate-defined open dot	60
5.1	Introduction	60
5.2	Electrical configurations	62
5.3	Pumped charge and rectification	63
5.4	Summary	68
6	Ballistic transport in double quantum point contacts in series	69
6.1	Introduction	69
6.2	Device arrangements	70
6.3	Density and length dependences of ballistic transport	71
6.4	Density dependence of quantum interference	78
6.5	Summary	80
7	Conclusions and future work	81
7.1	Summary	81



7.2 Future work	82
A Two QPCs coupled by a 1D channel	84
B Fabrication Recipes	87
B.1 Photolithography, Wet etch, and Ohmic Contacts	87
B.2 E-beam lithography	88
B.3 Insulating Layer	89
C Some Measurement Tips	91
C.1 Ground Loops	91
C.2 Telegraph Noises	92
D Device Inventory	93
Bibliography	97



List of Figures

1.1	Schematic of a GaAs-AlGaAs heterostructure; configurations for Shubnikov-de Haas oscillation and hall measurements; $R_{xx}(B)$ and $R_{xy}(B)$	3
1.2	Illustrations of a quasi-one-dimensional system and various measurement configurations.	6
1.3	Illustration of split gate technique and experimental results of conductance quantization.	8
1.4	Illustration and experimental results of non-equilibrium transport in a quantum wire.	13
1.5	Illustrations of transport in a closed QD and experimental results of coulomb blockade oscillations.	14
2.1	Design of 4" masks of photolithography in reduced scale.	16
2.2	Two optical microscopy images of a completed device. Magnifications are (a)100X (b)600X.	17
2.3	Schematic drawings for measurement setup.	18
2.4	Schematic drawings of the refrigerators.	19
3.1	$G(V_{sg})$ at various magnetic fields and temperatures; source-drain bias spectroscopy.	22
3.2	Linear conductance as a function of side gate voltage against top gate voltage and channel length presented by Reilly <i>et al.</i>	24
3.3	Polarization detection via magnetic focusing devices presented by Rokhinson <i>et al.</i>	25

3.4	Magnetic energy spectroscopy and source-drain transconductance spectroscopy in a quantum wire presented by Graham <i>et al.</i>	26
3.5	Numerical calculations of local density, potential, and conductance by spin-density functional theory by Starikov <i>et al.</i>	27
3.6	Noise factor as a function of averaged conductance in parallel magnetic fields from 0–7.5 T presented by Dicarlo <i>et al.</i>	28
3.7	Illustration of the Kondo scattering processes.	30
3.8	Linear conductance as a function of T/T_k , T_k as a function of V_g , evolution of of the ZBA with in-plane B presented by Cronewet <i>et al.</i>	31
3.9	Illustrations of e-ph and e-e scattering.	32
3.10	Theoretical calculations of non-equilibrium conductance with e-e scattering considered presented by Meidan <i>et al.</i>	32
3.11	Linear conductance $G(V_{sg})$ and micrographs of QWs of various lengths. . .	36
3.12	Linear conductance vs. split gate voltage and source drain bias voltage for various V_{tp} in a 0.5 μm quantum wire.	37
3.13	Source-drain bias spectroscopies of a quasi zero length quantum wire. . . .	38
3.14	Source-drain bias spectroscopies of quantum wires of several lengths at 0.3 K for $V_{tp}=0$	40
3.15	Semilogarithmic plot of f_a vs. $\frac{T_a}{T}$ for a L=quasi-zero QW against a series of V_{sg} at $V_{tp}=0$; activation temperature vs. split gate voltage at $V_{tp}=0$ for three devices.	41
3.16	$(G_{peak}^{ZBA}, e\Delta V_{sd}^{ZBA})$, $(G(0), \text{scaled } T_c)$, and $(G(0), \text{scaled } T_a)$ on the same plot for two L=quasi-zero QWs.	43
4.1	Conductance G for an electron waveguide plotted as a function of the width W of the channel with an attractive impurity in presence, presented by Chu <i>et al.</i>	47
4.2	Conductance of a QPC when a local potential minimum is in presence presented by Tekman <i>et al.</i>	48

4.3	G vs. E_F of a QW with a Gaussian impurity for three different impurity positions; the conductance of a QPC with long-range disorder in the presence for different impurity configurations. (Presented by Vargiamidis <i>et al.</i> and Takagaki <i>et al.</i>)	49
4.4	Potential contour of 2DEG and a QPC; conductance as a function of gate voltage for different impurity configurations presented by Nixon <i>et al.</i>	50
4.5	Conductance of a QW when edge roughness is in presence, presented by Csontos <i>et al.</i>	50
4.6	Schematic illustrations of the setup for lateral position shifting.	51
4.7	$G(V_g)$ and source-drain bias spectroscopies for two unintentionally disordered QWs at 0.3 K against the lateral shifting bias ΔV_g	53
4.8	Linear conductance $G(V_g)$ and source drain bias spectroscopy against $\Delta\tilde{V}_g$, of a disordered QW in the presence of strong conductance oscillations at 0.3 K.	55
4.9	Linear conductance $G(V_g)$ and source-drain bias spectroscopies of a clean quantum wire in two separate cooldowns at 0.3 K.	56
4.10	Linear conductance $G(V_g)$ and source-drain bias spectroscopy of a clean quantum wire against differential gate voltage ΔV_g	57
4.11	$G(V_g)$ and nonlinear conductance in two separate cooldowns of a QW with a small local widening at 0.3 K.	58
5.1	Illustrations of two electric configurations.	63
5.2	Dot resistance as a function of gate voltage V_{qpc2} when QPC1 is confined in various numbers of transmission mode.	64
5.3	A typical plot of the measured $I_{dc}(\Delta\phi)$; log-log plot of $I_p(V_{ac})$ and $I_r(V_{sd,ac})$. 65	
5.4	I_p and rescaled current I_p^* as a function of frequency for a an open dot having different transmission mode numbers in QPC1 and QPC2.	66
5.5	DC current I_r as a function of frequency for various mode number.	67
5.6	Dot resistance R_{dot} , I_p , and I_r as a function of perpendicular magnetic field B.	68

6.1	SEM Images and schematics of gate configuration for three different devices.	71
6.2	Quantized conductance of QPC1 as a function of split gate voltage.	72
6.3	Calculated 2D and 1D carrier density versus top gate voltage.	73
6.4	Conductance of two serially connected QPCs as a function of V_{sg1} against a series of V_{tg}	74
6.5	Normalized transmission probability T_d/N versus top gate voltage V_{tg} . . .	76
6.6	G_s^* vs. V_{qpc1} when QPC2 is controlled at $N_{qpc2} = 2$	77
6.7	Normalized direct transmission T_d/N as a function of edge-to-edge distance between two QPCs.	77
6.8	G_{12} as a function of V_{B-R} and V_A	79
6.9	Conductance variation ΔG_{12} as a function of V_A and V_{sd} for $V_{tp} = 0$	80
A.1	Conductance of the $0.8 \mu m$ QW as a function of gate voltage V_{L-R}	85
A.2	Conductance of confinements C1 and C2 as a function of V_A	86
B.1	(a) Layout of the device used to test the current leakage. (b) I-V of the insulating layers for different dosages at 77 K.	90
B.2	Thicknes of PMMA insulator as a function of exposed dosage.	90

List of Tables

1.1	Some important properties of 2DEG	4
D.1	Structures of 2DEG 5-70 and 50-66.	93
D.2	Structures of 2DEG 5-98 and 5-99.	93
D.3	Device list.	96

Chapter 1

Introduction

The invention of semiconductor transistors has completely changed human being's life, as well as our understanding of physics.[1] Since the introduction of the first transistor in 1950s, the techniques of semiconductor fabrications has advanced to an extent that was never imagined before. A modern integrated circuit chip of about $1 \times 1 \text{ cm}^2$ contains more than hundred millions of transistors. The physical dimension of a CMOS transistor is now about tens of nanometer, much less than one micron. At room temperature and in practical applications, the electrical properties are dominantly based on the classical Boltzmann transport. On the other hand, the scenario changes at very low temperatures when the electron-phonon scattering is not important. Compared with normal metals, the mean free path of semiconductors can be much longer, and the dimension of transistors can be small enough that electrons keep the phase during the travel across a device. In addition, with the flexibility of techniques, such as the matured semiconductor heterostructures [2] and the advanced lithographies, physicists are now equipped with powerful tools to explore the rich physics of electrons, many of which are direct manifestations of quantum mechanics. One of the most prominent is the quantum hall effect (QHE) in two dimensional electron gas (2DEG). [3] Others are conductance quantization, universal conductance fluctuations, etc. [4, 5] In this chapter, basics of mesoscopic transports in different dimensional regimes will be reviewed. Following up are a brief discussion of intricate features that incorporate many-body effects and the motivation of this thesis.

1.1 Two dimensional electron gas (2DEG)

2DEGs have been widely used for studying mesoscopic systems. In brief, 2DEG formed at the interface of two semiconductors by appropriately matching the lattice constants and band gaps. GaAs/AlGaAs is one typical and widely used heterostructure. The energy gap of AlGaAs is larger than GaAs. When these two crystals are in contact, electrons move from AlGaAs to the lower Fermi states in GaAs, leaving positive charged donors behind. The space charges give rise to an electrostatic potential and the energy band bends, forming a narrow quantum well along the growth direction (along \hat{z} axis). By carefully doping and quantum well engineering, carriers can occupy only one state below the Fermi level along \hat{z} axis. At the quantum well, a conducting quasi two dimensional layer is formed at the interface of GaAs and AlGaAs as shown in Fig. 1.1(a). The motion in \hat{z} is forbidden, however the carriers travel freely in other two directions.

Two important properties of 2DEG are the carrier density n_s and mobility μ , because they relate directly to electrical transport; n_s is typically from $\sim 2 \times 10^{11} \text{cm}^{-2}$ to $2 \times 10^{12} \text{cm}^{-2}$ while μ is generally several $10^6 \text{cm}^2/\text{V} \cdot \text{s}$. To determine the carrier density and mobility of 2DEG, one study the Shubnikov-de Haas Oscillation and Hall effect. The substrates are fabricated as so called Hall bar as shown in Fig. 1.1(b). The longitudinal resistance $R_{xx} = V_{xx}/I$ while the transverse resistance $R_{xy} = V_{xy}/I$. Fig. 1.1(c) shows a typical result of $R_{xx}(B)$ and $R_{xy}(B)$, where B is an out-of-plane magnetic field. The magnetic field provides effectively an additional dimensional constraint and highly degenerate *Landau Levels* form below the Fermi energy. Quantum hall effect is the manifestation of resistance steps at $\frac{1}{i} \left(\frac{h}{e^2} \right)$ in R_{xy} at high magnetic fields where $i = 1, 2, \dots$. The steps correspond to the discrete edge states supplying current flow between transverse contact leads. Each resistance maximum of the R_{xx} oscillations and the riser between two plateaus of R_{xy} correspond to fully filled Landau levels. The finite width of oscillations and smooth transitions between plateaus are due to the potential fluctuations in the 2DEG.[6]

n_s can be calculated by

$$n_s = \frac{2e}{h} \left(\Delta \frac{1}{B} \right)^{-1} \quad (1.1)$$

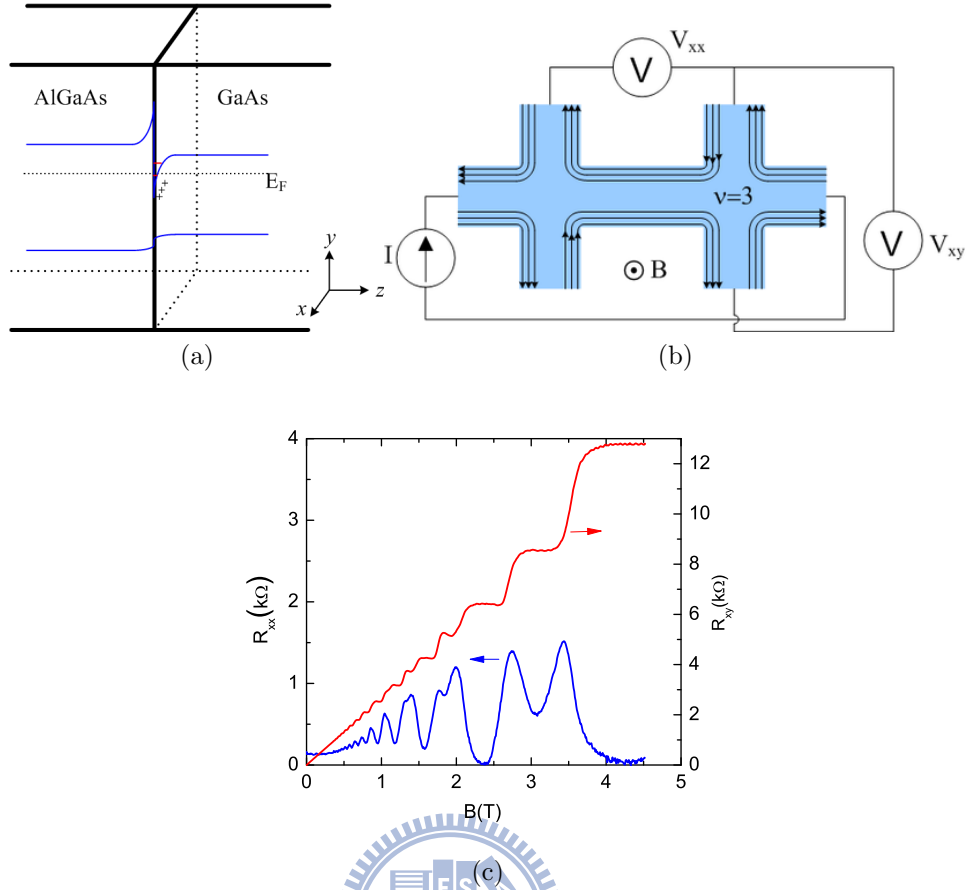


Figure 1.1: (a) Schematic of a GaAs-AlGaAs heterostructure and its band diagram. (b) Sketch of configurations for Shubnikov-de Haas oscillation and hall measurements. The solid lines near the edge of the hall bar stand for discrete edge states induced by the magnetic field. (c) $R_{xx}(B)$ and $R_{xy}(B)$ of 2DEG. The result is obtained from our 2DEG 5-70.

, where $\Delta \frac{1}{B}$ is the period of R_{xx} oscillations as a function of inverse of magnetic field, $1/B$. n_s can also be calculated by Hall measurement at low magnetic fields where the quantum hall effect is still negligible when Landau levels are not developed.

$$n_s = \left| e \frac{dR_{xy}}{dB} \right|^{-1} \quad (1.2)$$

The mobility is given by,

$$\mu = |en_s \rho_0|^{-1} \quad (1.3)$$

where ρ_0 is the sheet resistance. Knowing n_s and μ , many properties of 2DEG can be obtained. Table.1.1 shows some of the most important characteristics of 2DEG.

Throughout this thesis, one GaAs/ $\text{Al}_x\text{Ga}_{1-x}\text{As}$ heterostructure substrate (5-70) grown

Fermi wave vector	$k_F = (4\pi n_s / g_s g_v)^{1/2}$
Fermi wavelength	$\lambda_F = 2\pi / k_F$
Fermi velocity	$v_F = \hbar k_F / m^*$
Scattering time	$\tau = m^* \mu_e / e$
Mean free path	$\ell_m = v_F \tau$

Table 1.1: Some important properties of 2DEG

using molecular beam epitaxy at the Weizmann Institute in Israel was used for device fabrication. Mobility is approximately $1.7 \times 10^6 \text{ cm}^2/\text{V} \cdot \text{s}$ and n_s is $2.4 \times 10^{11} \text{ cm}^{-2}$ corresponding to the elastic mean free path ℓ of about $14 \mu\text{m}$ at helium temperatures.

1.2 Diffusive transport versus ballistic transport

In metals, the electrical properties are usually governed by diffusive transport, where the mean free path ℓ_m is much smaller than the device size. The electrical ‘resistance’ reflects the macroscopic characteristics of materials by $R = \frac{L}{\sigma A}$, where L is the length, A is the cross sectional area, and σ is the conductivity of the bulk material. In semiconductors, and more specifically in 2DEGs, the mean free path ℓ_m and the phase breaking length ℓ_ϕ can be reached to more than several μm while the device size is merely a few hundreds nm.[7] The electrons travel across the device without being scattered and losing the coherence. The electrons transport *ballistically* and the wave nature such as interference, discrete energy levels etc. could be revealed. In this regime, quantum transmissions and reflections govern the overall transport and conductance characterizes directly the electrical transport as conductance is proportional to total transmission probability.

1.3 One Dimensional Transport

1.3.1 Two-terminal and four-terminal conductances of 1D conductors

In 1957 and 1970, Landauer proposed an elegant formula expressing the conductance of a perfect 1D conductor with a scatterer inside. The conductor contains one conducting

channel and the conductance is

$$G = \left(\frac{2e^2}{h} \right) \frac{T}{R} \quad (1.4)$$

T and R are the transmission and reflection probabilities in the presence of the scatterer, respectively.[8, 9] This is the well known Landauer formula. Later, Buttiker generalized the result to the multi-channel case, where the conductor contains arbitrary number of conducting channels N in both source and drain leads.[10]. As shown in Fig. 1.2(a), electrons incident from i -th mode on the left lead have the probability of tunneling into j -th mode on the right lead, T_{ji} and reflecting back into k -th mode on the left lead R_{ki} . The whole system can be described by a $2N \times 2N$ scattering matrix \mathbf{S} :

$$\mathbf{S} = \begin{pmatrix} r & t' \\ t & r' \end{pmatrix} \quad (1.5)$$

t , t' , r , and r' are $N \times N$ submatrices containing elements of all possible combinations of transmission and reflection coefficients. Summing over currents in all channels, the conductance of the scatter is

$$G = \frac{I_{tot}}{(\mu_A - \mu_B)/e} = \frac{2e^2}{h} \frac{\sum_{i=1}^N T_i \frac{2 \sum_{i=1}^N v_i^{-1}}{\sum_{i=1}^N (1 + R_i - T_i)^{-1}}}{\sum_{i=1}^N (1 + R_i - T_i)^{-1}} \quad (1.6)$$

$T_i = \sum_{j=1}^N T_{ij}$ is the total transmission of electrons tunneling into mode i from all other modes, and similarly $R_i = \sum_{j=1}^N R_{ij}$ is the total reflection of electrons scattering from all other modes into the incident mode. μ_A and μ_B are the chemical potentials in the leads. However, there is once a very puzzling issue about the conductance. As a simple illustration, consider equation 1.4 for a perfect conductor as the scatterer. In this case $R=0$ and $T=1$, the conductance becomes infinite and is not physical. The resolution came to what potentials the voltage probes measured. In many experiments, such as electrical measurement of quantum wires and quantum dots, both the electrical current and voltage leads are located in the same reservoirs. As shown in Fig. 1.2(b), the white voltage probes

measure the chemical potentials at the reservoirs μ_1 and μ_2 . However, the theoretical derivations considered the potentials inside the leads, as the gray probes indicate in the same figure. The chemical potentials of the leads are μ_A and μ_B . $\mu_{1(2)}$ is usually not equal to $\mu_{A(B)}$ due to the piling up charges at the inner junctions at the leads and the scatterer. The conductance measured by the latter setup is *four-terminal conductance*, while in the earlier case it is *two-terminal conductance*. The two-terminal conductance reduces simply from equation 1.6 by replacing μ_A and μ_B with μ_1 and μ_2 .

$$G_{2term} = \frac{I_{tot}}{(\mu_1 - \mu_2)/e} = \frac{2e^2}{h} Tr(tt^\dagger) \quad (1.7)$$

To correctly obtain four-terminal conductance, one would intuitively consider exploiting multi-terminal measurement. However the configurations raise issues of probe invasiveness or nonlocality. Experimental studies of nonlocality can be found in literatures.[11, 12, 13]

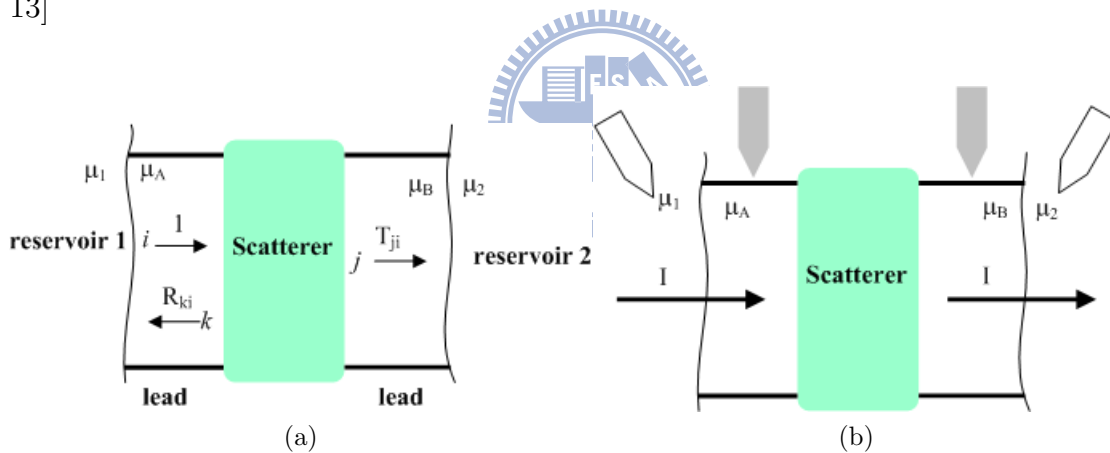


Figure 1.2: (a) Schematic illustrations of a quasi-one-dimensional system. Each leads contain N perfect conducting channels. (b) Various measurement configurations. The gray probes measure the local chemical potentials μ_A and μ_B . The white probes measure the chemical potentials at the reservoirs.

1.3.2 Quantum point contacts and quantum wires

The *split gate* techniques are often exploited for the experimental realization of 1D channels. As the illustration shown in Fig. 1.3(a), a pair of Ti/Au gates separated by a gap is fabricated on the surface of 2DEG substrates. Electrons beneath the gates are depleted by applying a negative voltage on the split gates. The electrical potential barriers squeeze

the electrons forming a *point contact*. The energy is quantized along the transverse direction (\hat{y} axis) establishing discrete subbands and confining the electron motions to along \hat{x} axis. The length of the slit L is much shorter than ℓ_m , therefore the electrons travel ballistically inside the channel. The width of the gap W is a few electron wave length wide. Such structure was referred to as a *quantum point contact* (QPC) for a short constriction, or a *quantum waveguide/quantum wire* (QW) for a longer one. Since electrons inside the constriction only scatter spectacularly on the potential edges, each subband stands for a perfect conducting channel, i.e. each subband has a unity transmission. In connection with eq. 1.7, the total transmission of the confined QPC is just the number of subbands n below the Fermi energy and the conductance is just the integer multiples of $2e^2/h$, $G = n \cdot (2e^2/h)$. The energy of the n -th subband can be expressed as

$$E_n = V_0 + E_n^y + \frac{\hbar^2 k_x^2}{2m^*} \quad (1.8)$$

V_0 is the potential in the center of the constriction, $E_n^y = \hbar\omega_c(n + \frac{1}{2})$ for a parabolic potential and $E_n^y = \frac{n^2\hbar^2}{8m^*W}$ for a hard wall potential. By decreasing the gate voltage to more negative values, the density or the width of QPC is decreased lifting the subband energy. As soon as one subband is pushed to be higher than the Fermi energy E_f , the conductance drops one $2e^2/h$ lower. Sweeping the gate voltage effectively varies the width of QPC as well as the number of subbands below E_f . The conductance shows steps as a function of the gate voltage as shown in Fig. 1.3(b) demonstrating fascinating *conductance quantization*. The very first experimental demonstration of conductance quantization was reported by Wharam *et al.* and van Wees *et al.* [14, 15] Since then, extensive studies on one dimensional transport have been performed.

The conductance quantization is due to perfect transmission of 1D subbands. However, the traveling waves would be backscattered if the channel contains some physical scatterers revealing more complicated features. Scatterers can be geometrical discontinuities, potential fluctuations due to randomly distributed ionized donors, or lattice dislocations (or defects). One example of geometrical discontinuity is bended quantum waveguides. There are significant similarities between classical electromagnetic waveg-

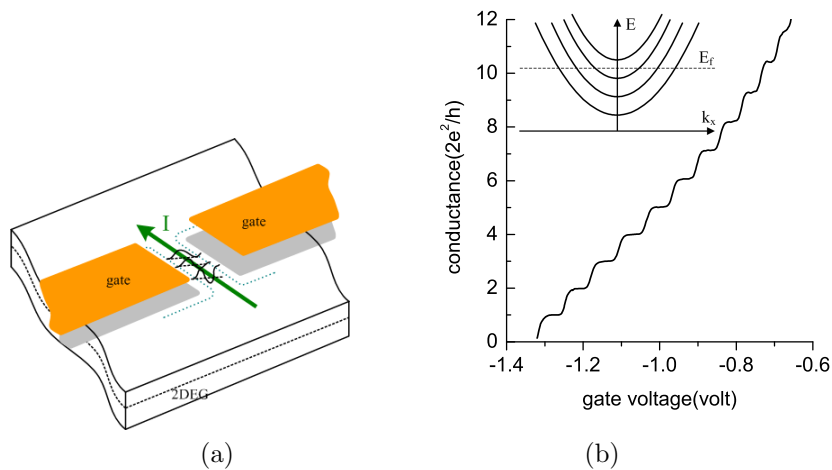


Figure 1.3: (a) Illustration of split gate technique. The gray areas indicate the depletion areas after applying a negative voltages on the gate. (b) Conductance as a function of split gate voltage, showing clear conductance steps. Inset: Dispersion of the quantized subbands.

uides and quantum waveguides. For instance, both have discrete transmitting modes and can be theoretically analyzed by *scattering method* and *mode matching* method.[5, 4, 16] They were expected to have similar transport characteristics. A classical bended microwave waveguide were well known to have transmission resonances. The incident wave is transmitting on the resonance, but reflected when the frequency is off resonant. Wu *et al.* demonstrated that conductance of a double bended quantum wire exhibits resonances for $G < G_0$ due to the shape discontinuity.[17, 18] The effects of impurity on transport were also investigated extensively by many theorists. Chu *et al.* reported that a repulsive impurity smears the conductance quantization, while an attractive impurity may introduce resonances.[19] Intuitively, an attractive impurity shall induce a local potential minimum inside the channel and quasi-bound states are expected to exist. The argument was confirmed by Bagwell[20] and many other groups. Another source of scattering is the averaged potential fluctuations due to the randomly distributed ionized donors. The potential fluctuates in space and may cause imperfections inside the quantum wires. Conductance quantization would be suppressed and resonances were induced in a quantum wire shorter than the correlation length of such potential fluctuations.[12, 21, 22] In the latter chapter, the influence impurity on transport will be discussed in detail.

1.3.3 Nonequilibrium transport in quantum wires

So far the discussions are in linear regime, i.e. the source drain bias is small enough that the I-V curve is linear. When a finite dc bias V_{sd} is applied across the QW, the energy window of source and drain opens up and the conductance becomes nonlinear due to the energy gap of QWs. New plateaus at half integer multiples of $2e^2/h$ would exist and information of energy level spacing may be extracted. For simplicity, it is reasonable to assume that the applied bias drops *linearly* across the QW. As shown in Fig. 1.4(a) the right going ($>$) electrons inject into the channel with energy $\mu_1 + eV_{sd}/2$ while the left going ($<$) electrons are inject with $\mu_2 - eV_{sd}/2$. There are three subbands below E_f at zero bias. The current flow of the QW reflects the summation of both left and right going electron waves:

$$I(V_{sd}) = \frac{2e}{h} \sum_n \left[\int_0^{\mu_1 + eV_{sd}/2} T_n^>(E, V_{sd}) dE - \int_0^{\mu_2 - eV_{sd}/2} T_n^<(E, V_{sd}) dE \right] \quad (1.9)$$

The numbers of subbands below the chemical potentials at left and right leads differ for large enough V_{sd} . (1) When $\mu_1 + eV_{sd}/2$ reaches the 4th subband bottom, the right-going electrons have one additional transmitting channel; (2) when $\mu_2 - eV_{sd}/2$ reaches the 3rd subband bottom, the left-going electrons have one less channel for transmission.[23, 24] In the former case, the conductance increases one-half $G_0 = 2e^2/h$ reaching $3.5G_0$; in the latter case, the conductance reduces one half G_0 dropping to $2.5G_0$. Whether case 1 or 2 would take place depends on the energy difference between E_f and the subband bottoms. Therefore, at large enough V_{sd} , the trace of conductance shows steps at $(n+1/2)G_0$, where $n=0,1,2,\dots$ etc.[25, 26] Fig. 1.4(b) shows conductance versus split gate voltage V_{sg} for a series of V_{sd} . *Half plateaus* lying between integer plateaus begin to emerge at $V_{sd} \sim 0.7$ mV. For $V_{sd} \gtrsim 1$ mV, integer plateaus vanish indicating eV_{sd} is larger than one level spacing.

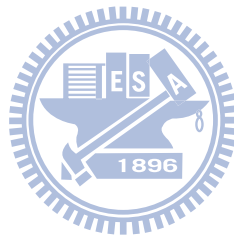
Measurement of such non-linear conductance can be exploited to extract the information of subband level spacing.[27, 28] Differentiating the traces in Fig. 1.4(b) and mapping the data into 3D plot, Fig. 1.4(c) shows the contour of dG/dV_{sg} as a function of V_{sg} and V_{sd} . The large black areas between white bands represent plateaus. The band labeled by $n_i^{+(-)}$ indicates the alignment of the i -th subband bottom with the source

(drain) chemical potential. The source drain bias where two bands intercept is approximately the level spacing between i -th and $(i+1)$ -th subbands. Measurement can be done in a somewhat alternative way. By sweeping V_{sd} while V_{sg} is fixed and measuring the differential conductance $G = dI/dV_{sd}$, the so called *source-drain bias spectroscopy* is exploited. Martin-Moreno et al. theoretically investigated the spectroscopy in the frame of *non-interacting particles*. A bell shaped $G(V_{sd})$ for a specific V_{sg} was predicted.[28]

1.4 Zero dimensional transport-closed quantum dot

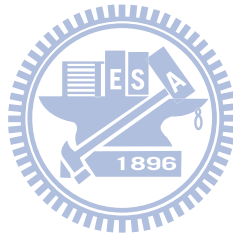
Imposing constrictions on both the longitudinal and transverse directions, electrons are confined in space forming so called-quantum dot (QD). In the absence of Zeeman splitting, the spin degenerate states of the localized electrons are discretely quantized with an energy $E(N)$. As shown in Fig. 1.5(a), the electrons have to tunnel through two barriers from source to drain. Considering *sequential tunneling*, the tunneling current reaches a maximum whenever there is a state lying between the source and drain chemical potentials. Otherwise, the tunneling is blocked and current becomes very small referred to as *Coulomb Blockade*. The energy of the states can be controlled by a capacitively coupled gate V_g . By sweeping V_g , the measured current oscillates as a function of V_g , as illustrated in Fig. 1.5(c), which is referred to as *Coulomb Blockade Oscillations*. Each current peak stands for a state falling in between the source and drain chemical potentials. The period of the oscillations depends on the competition between the level spacing of a QD, $\Delta E(N + 1, N) = E(N + 1) - E(N)$ and the charging energy $E_c \sim e^2/C_{tot}$. E_c is the electrostatic energy that the system requires for adding one electron. C_{tot} is the sum of all capacitive couplings to the dot, for instance C_{tot} equals to $C_g + C_s + C_d$ based on the model circuit shown in Fig. 1.5(b). With states being spin degenerate, the gate voltage difference between two conductance peaks is $\Delta V_g = \alpha e/C_g$ for a QD occupied with an *odd* number of electrons and is $\Delta V_g = \alpha (\Delta E(N + 1, N)/e + e/C_g)$ for a QD occupied with an *even* number of electrons.[29] Fig. 1.5(d) is the experimental result of a $0.2 \times 0.6 \mu m^2$ square QD where the Coulomb Blockade Oscillation is observable. There are substantial realizations of QDs of different types and QDs is itself a major field in low dimensional

physics. Plenty of reviews can be found. There are some good reviews about charging effect and quantum properties in laterally confined QDs [29, 30, 31] and the recent progress in few electrons QDs. [32, 33]



1.5 Organization of this dissertation

This chapter introduced essentials of mesoscopic systems basically in a single particle picture. In the following chapters, discussions extend to more complicated systems, and also to many-body physics. Chapter 2 describes the rudiments of experimental practice. Chapter 3 discusses the dependence of transport on physical properties in quantum wires. Chapter 4 demonstrates the effect of impurities on the linear and non-linear conductances of quantum wires. Chapter 5 describes a measurement of DC currents generated from two time-dependent fields in an open quantum dot. Chapter 6 presents the study of double quantum point contacts coupled in series. Chapter 7 is the final conclusion and future directions. In appendix A, some preliminary data of transport in QPCs laterally coupled via a quantum channel is presented. Appendix B contains detailed fabrication recipes. Appendix C is some suggestions for measurement learned from experience. Appendix D lists all studied samples.



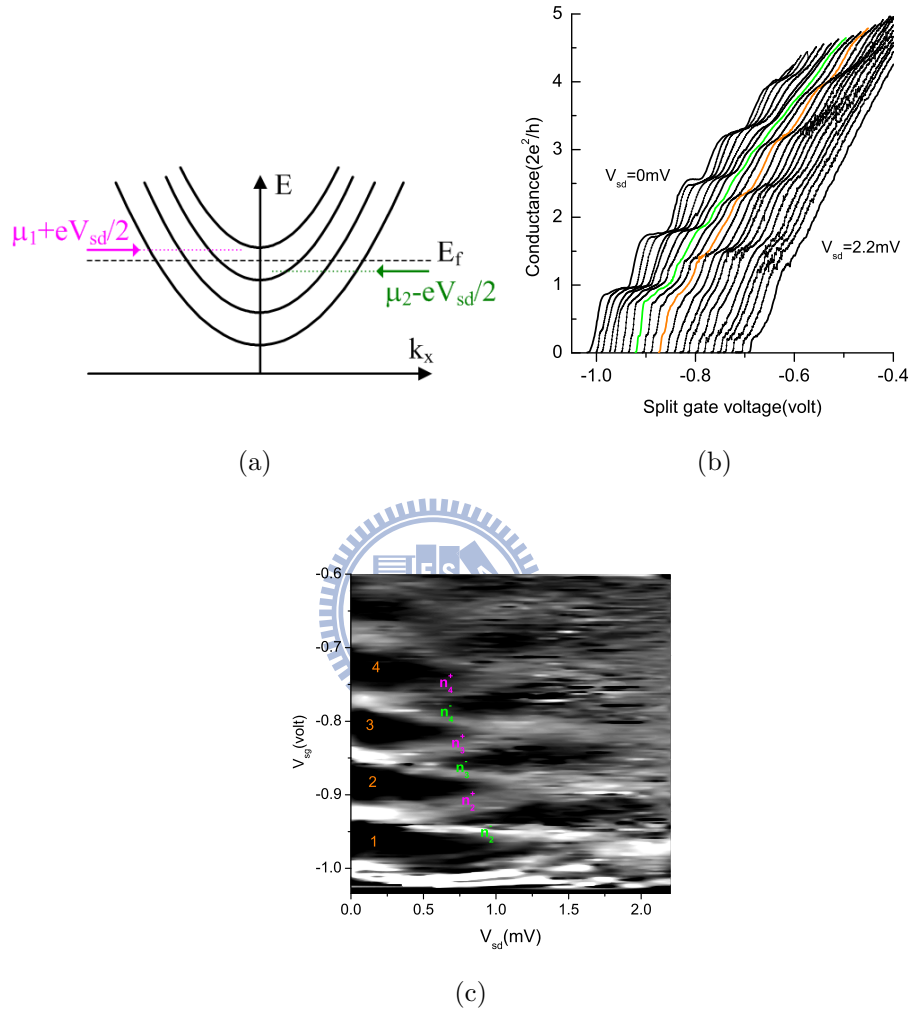


Figure 1.4: (a) Illustration of transport in a finite source drain bias in a quantum wire. (b) Conductance of a QW $G(V_{sg})$ for $V_{sd}=0$ to 2.2mV in steps of 0.1 mV at 0.3 K. Traces are offset for clarity. (c) Contour plot of dG/dV_{sg} as functions of V_{sg} and V_{sd} . White(black) represents high(low) value of dG/dV_{sg} . Numbers label the integer plateaus. A Band of $n_i^{+(-)}$ indicate the alignment of a subband bottom with source(drain) chemical potential. The result was obtained from one of our quantum wire with a channel length of 0.5 μm .

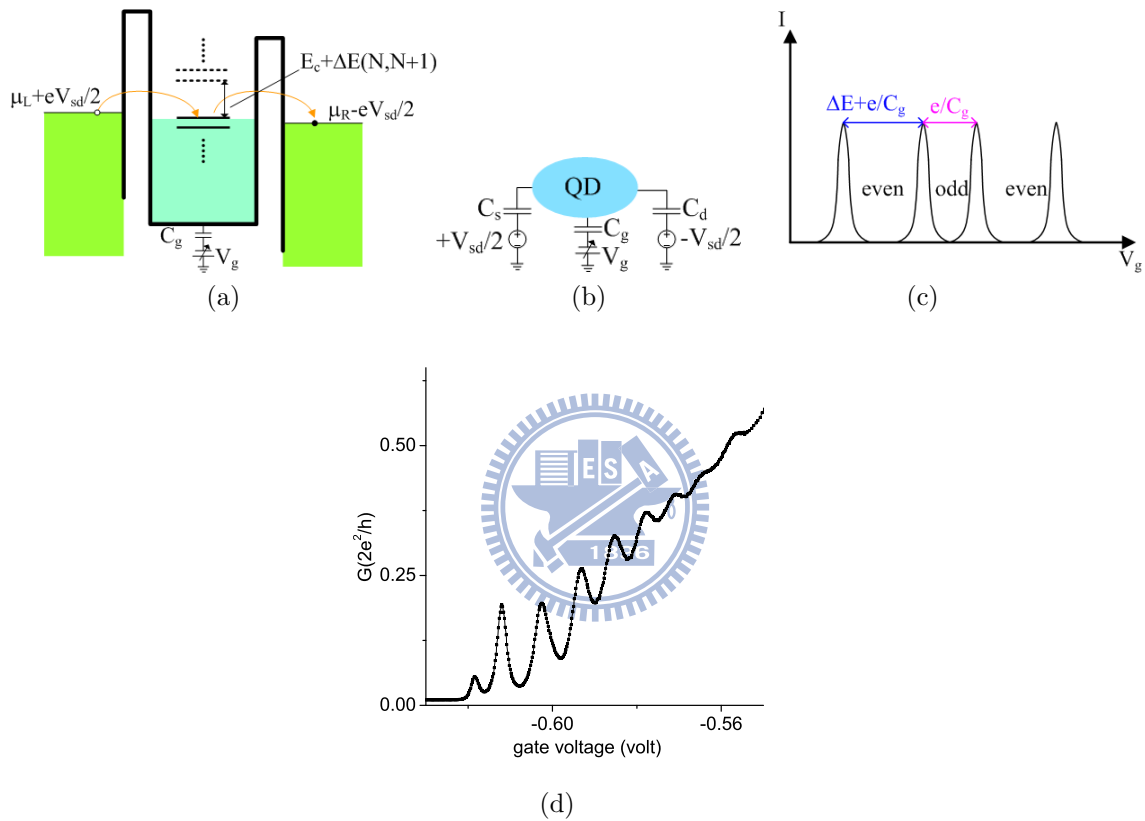


Figure 1.5: (a) Illustration of potential profile and tunneling processes in a quantum dot. (b) Equivalent circuit of a quantum dot and its environments. (c) Schematic illustration of Coulomb blockade oscillations. (d) Conductance vs. gate voltage from one of our fabricated square QDs with a lithographic area of $0.2 \times 0.6 \mu\text{m}^2$ showing coulomb blockade oscillations.

Chapter 2

Experimental techniques

2.1 Device fabrications

The fabrications contain many processes. They principally include three stages: (a) mesa, (b) ohmic contacts, and (c) gates. Photolithography was exploited to transfer large scale and repeating patterns. On the other hand, e-beam lithography is necessary for small scale patterns since the resolution is higher and is more flexible for prompt modifications.

Photolithography

Resist AZ5214E was mostly used. The primary advantage is that it can be used as a negative tone resist for image reversal forming a better undercut on the edge which is beneficial for lift-off after the thin-film deposition. Broken pieces of substrates coated with photoresist were exposed with Near UV by the commercial mask aligning and exposing system built by ABM Inc. The exposed resist was developed in AZ 300 or diluted AZ 400K (20% concentration in DI water). After transferring the pattern: (a) the broken chips were wet etched for the isolation between devices forming so called *mesa*; (b) layers of Ni, Au, and Ge were deposited followed by *lift-off*. The substrates were then *annealed* in a furnace. With proper parameters, the metals diffused into GaAs forming alloy with the substrate. The alloy establishes electrical contact with 2DEG referred to as *ohmic contact*; (c) Ti and Au were deposited followed by lift-off referred to as *gates*. Repetitive

large Ti/Au gates were fabricated before proceeding to fabrication of smaller gates by e-beam lithography. The detailed recipe and procedures are listed in Appendix B.1. Fig. 2.1 is an example of 4" masks in reduced scale for several experiments.

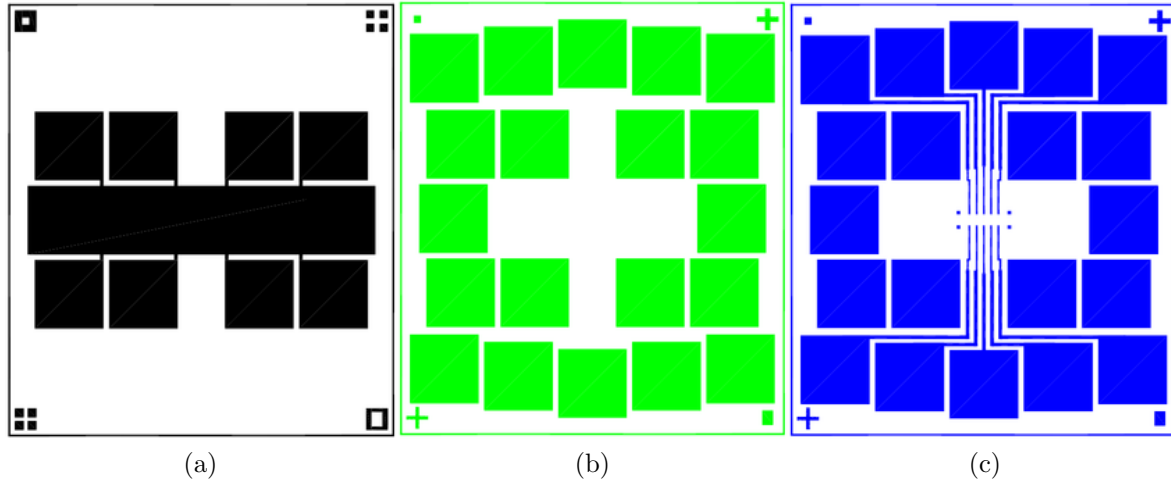


Figure 2.1: Design of 4" mask of photolithography for (a) mesa (b) ohmic contact, and (c) gate in reduced scale.

E-beam Lithography



Fabrication of smaller gates by e-beam lithography follows similar procedures. The desired patterns vary from experiment to experiment, thus e-beam lithography is more suitable. Commercial resist PMMA 5A (molecular weight: 495K, concentration: 5%, manufactured by MicroChem Corp.) was spin coated on substrates. The prebaked resist was then exposed by focused electron beam. The electron beam was generated in Hitachi S-3000H Scanning Electron Microscope installed with Nano Pattern Generation System (NPGS). The beam was positioned by NPGS, transferring the patterns edited by the software DesignCAD2000. After the exposure, the resist was developed in MIBK diluted by IPA by a ratio of 1:3. Deposition of Ti-Au and lift-off followed the development. The detailed recipe is included in Appendix B.2. Gates were fabricated first with Ti/Au \sim 80 nm in thickness, followed by the fabrication of metallic leads which ensures the electrical contact between the devices and the bonding pads. In this step, the thickness of Ti-Au was \sim 150-200nm. Thicker resist was required for better yields of the leads after the lift-off, e.g. 10% PMMA. Besides the split gates which control the width of QWs, a top gates could be

fabricated to control the density of carrier. A layer of dielectric insulates the split gates from the top gates. The dielectric layer was fabricated by overexposing PMMA. Detailed recipes and some testing results in term of current leakage are included in Appendix B.3. Figs. 2.2(a)-(b) show two images of a completed device by an optical microscope.

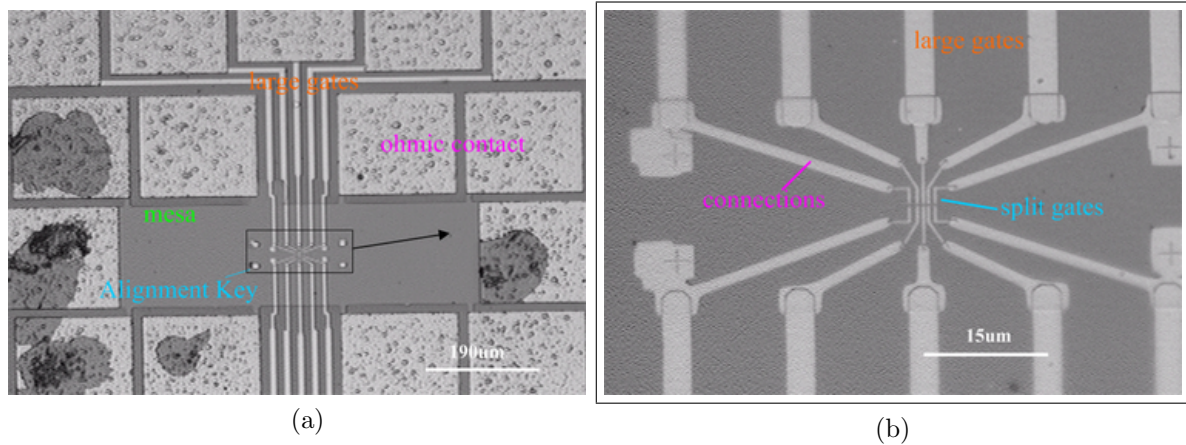
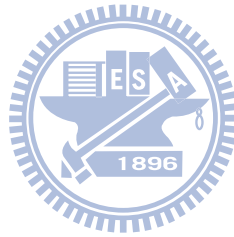


Figure 2.2: Two optical microscopy images of a completed device. Magnifications are (a)100X (b)600X.

2.2 Measurements



The samples, as well as some flexible PCBs (plastic circuit board) were attached on a sample holder made by copper using GE varnish. Gold wires were bonded from the gates and ohmic contacts to the gold pads on the PCBs. The holder was mounted on the fridges. The electrical signals were acquired at the room temperatures through the manganin wires in the fridges. Most of the measurements were done by *four-wire voltage bias* mode. An excitation voltage of 11-51 Hz supplied by a commercial lock-in amplifier (Signal Recovery, Model 7265) was applied on two ohmic contacts. The current I_{ac} flowing through the device was converted to a voltage signal by a current preamplifier (DL Instruments, Model 1211) and fed back to the lock-in amplifier. The voltage drop across the sample V_{ac} was amplified by a voltage preamplifier (Standard Research System, Model: SR560). Both monochromatic signals were locked by the lock-in amplifiers and read by a computer through the protocol IEEE-488. The differential conductance is $G = I_{ac}/V_{ac}$. A homemade circuit box supplied by two batteries serves for sweeping a dc

voltage V_{dc} . The output voltage of the box automatically sweeps back and forth between two voltage limits. V_{dc} was applied on the device in series with V_{ac} for the source-drain bias spectroscopy measurement. Gate voltage can be easily applied by a battery or a commercial signal generator. Fig. 2.3 shows the schematic drawings for the measurement configurations. With proper tuning and configuration, the optimized signal fluctuation is ~ 700 fA at ~ 40 Hz.

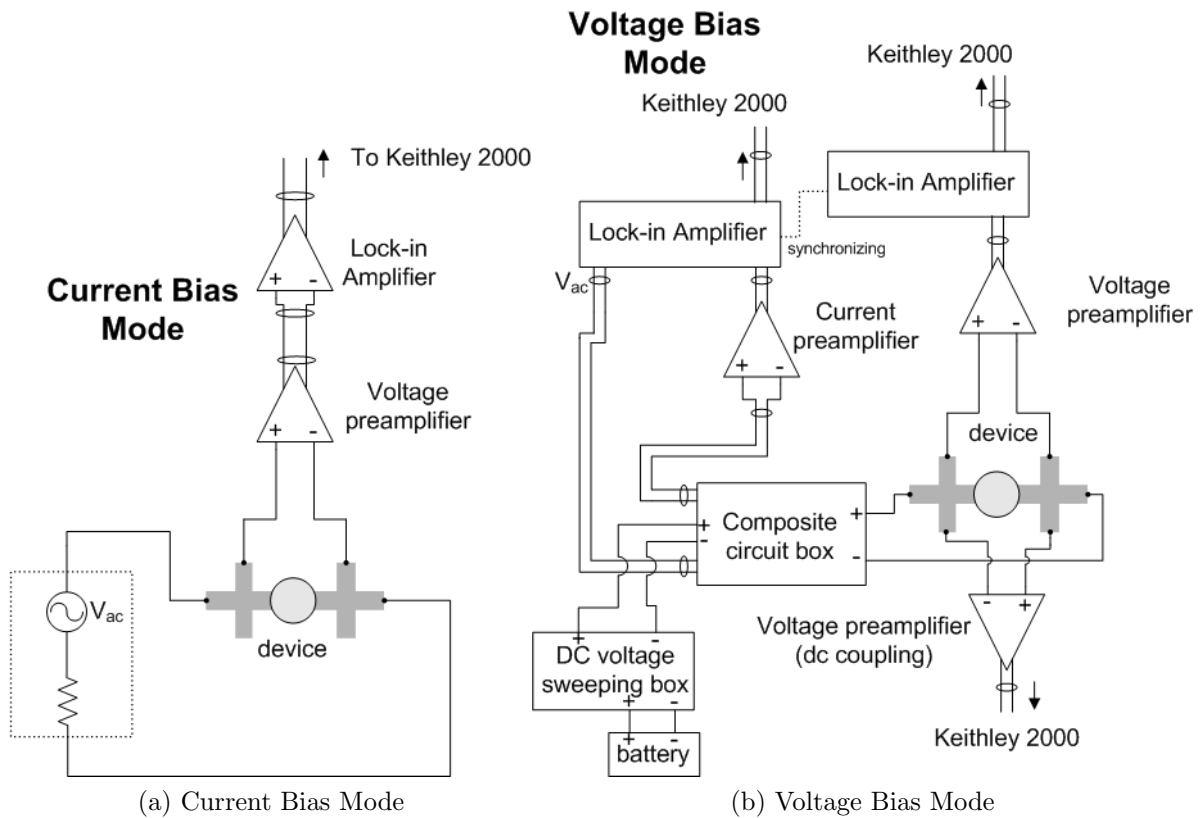


Figure 2.3: Schematic drawings for measurement setup.

2.3 Cryostats

The measurements were done at low temperatures in a pumped ^3He cryostat or a dilution refrigerator. The close-cycle pumped ^3He fridge, model Heliox VT, was manufactured by Oxford Instruments. The base temperature is 0.28 K while the holding time with the sample holder mounted on the ^3He Pot and 24 manganin wires installed is about 12 hours. The temperature with $100 \mu\text{W}$ heat load is $\lesssim 0.4$ K. Three calibrated thermometers

supplied by the manufacturer were installed and monitored by the temperature controller ITC 503 built by Oxford Instruments. Allen Bradley type sensor (100Ω , 1.6–250 K) was at the Sorb; RuO_2 resistor ($2.2\text{ k}\Omega$, 0.25–10 K) and Cernox 1050 AA (1.5–300 K) were at ^3He Pot. An additional calibrated RuO_2 ($1.3\text{ k}\Omega$) resistor type sensor was installed on the sample holding rod. The temperature stability is within $\pm 3\text{ mK}$ for $T \lesssim 1.2\text{ K}$. During the operations, ^3He is absorbed from the tank at room temperature and condensed at ^3He Pot by keeping the temperature of Sorb at $\sim 40\text{ K}$, as shown in Fig. 2.4(a). The base temperature is reached by releasing the heat load at Sorb and vaporising the liquified ^3He .

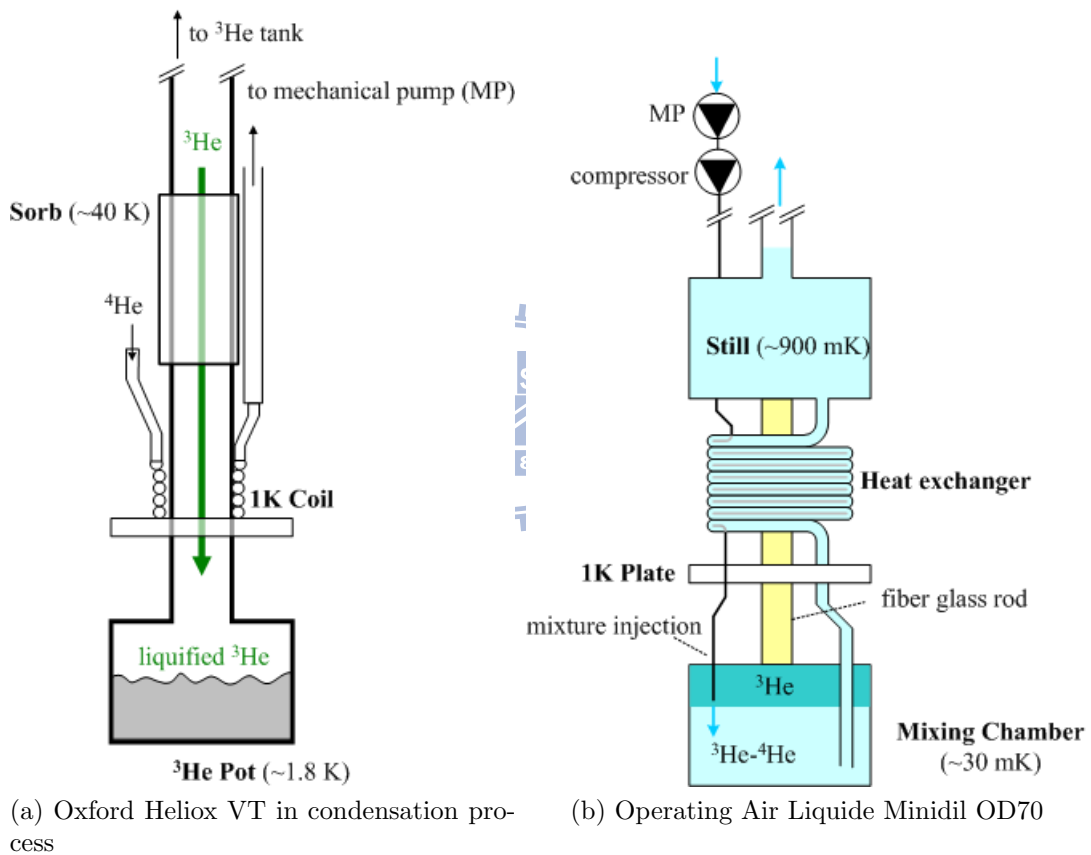


Figure 2.4: Schematic drawings of the refrigerators.

The $^3\text{He}/^4\text{He}$ dilution refrigerator, model Minidil OD 70, was manufactured by Air Liquide France. Minidil OD 70 has a base temperature of 30 mK. 24 manganin wires were installed running from a Fischer connector at room temperature to the sample holding rod. The circulation rate of the mixture is $\sim 30\ \mu\text{mol}/\text{s}$; the cooling power at 100 mK is around $15\ \mu\text{W}$. The temperature was monitored and controlled by temperature controller

TRMC2 resistance bridge which required its application being installed on a computer. Four thermometers were installed on the fridge: one PT 100 type sensor on the 4 K screen; one RuO₂ type at the still level; one RuO₂ type at the mixing chamber; one RuO₂ type at the sample holding rod. Two heaters of 500 Ω and 1 $k\Omega$ were installed at the still and mixing chamber respectively. 1 K pumping pot is absent in this system and it is not necessary to heat the still during the operation. The pumped mixture is compressed and precooled in the Joule-Thomson stage. The condensed mixture is heat exchanging with the outgoing mixture and finally re-inject to the mixing chamber. Fig. 2.4(b) illustrates the functioning of the fridge.

2.4 Magnet and dewar

A superconducting magnet produced by American Magnetics Inc. was used to apply magnetic field up to 9 T. The magnet was made by NbTi solenoids with 10 Henry measured inductance, $\pm 0.1\%$ homogeneity over 1cm diameter spherical volume, and 1172 *Gauss/Amp* field to current ratio. The current source, IPS-120, was provided by Oxford Instruments. The storage dewar was manufactured by Precision Cryogenic Systems Inc. with a liquid nitrogen jacket for screening the radiation in order to reduce the helium consumption. The average helium consumption rate was ~ 0.38 liter/hour when the superconducting magnet was installed and Minidil OD70 was inserted in the dewar.

Chapter 3

Zero-bias anomaly and conductance reduction in quantum wires

3.1 Introduction

The transport in quantum wires can mostly be understood in single particle picture as discussed in chapter one. However, experimentalists have presented observations that cannot be described by single particle physics. The peculiar features were often observed in the regime of low carrier density or for conductance less than $2e^2/h$. The observations have brought a new direction for studying many-body interactions in semiconductors. In this chapter, the dependence of these mysterious phenomena on the physical properties of devices is described. The electron-electron interaction has a central role in these peculiarities.

3.2 0.7 structure and zero bias anomaly

The linear conductance is quantized into integer multiples of $G_0 = 2e^2/h$ due to the transmission of spin-degenerate 1D subbands within a noninteracting electron picture. However, Thomas et al. found an extra conductance shoulder at $\sim 0.7G_0$ at low temperatures in *zero* magnetic field. The peculiar shoulder, 0.7 anomaly, was associated with spontaneous polarization.[34, 35, 36] As shown in Fig. 3.1(a), the anomaly conductance

decreases from $\sim 0.8G_0$ at 0 T to $\sim 0.6G_0$ at 9 T where Zeeman splitting is about to be important. The anomaly is robust against the increasing temperature. As temperature is raised such that the quantization plateaus are suppressed, the anomaly is more clearly seen as shown in Fig. 3.1(b). Another peculiar feature is the ‘zero bias anomaly’ (ZBA) observed in the source drain bias spectroscopy. A dc source-drain voltage V_{sd} across a confined QW was swept with the differential conductance $G = dI/dV_{sd}$ being measured. ZBA, as shown in Fig. 3.1(c), is referred to as the series of conductance peak centered at zero-bias. Cronenweert *et al.* reported that the linear conductance as a function of temperature can be scaled to a universal equation.[37] Additionally, ZBA was reported to split in magnetic fields in correspondence with Zeeman splitting. Extensive studies, either theoretical or experimental, have been intrigued by these findings. The 0.7 anomaly which usually accompanies a conductance reduction near the first plateau, a lowered conductance at high temperatures, was mostly attributed to spin related mechanisms. [35, 36, 37, 38, 39, 40, 41, 42, 43, 44, 45, 46, 47, 48, 49, 50, 51] One dimensional Kondo physics was proposed to describe the scaling of conductance to a universal form and the splitting of the ZBA in magnetic fields.[37, 48, 49, 50, 51]

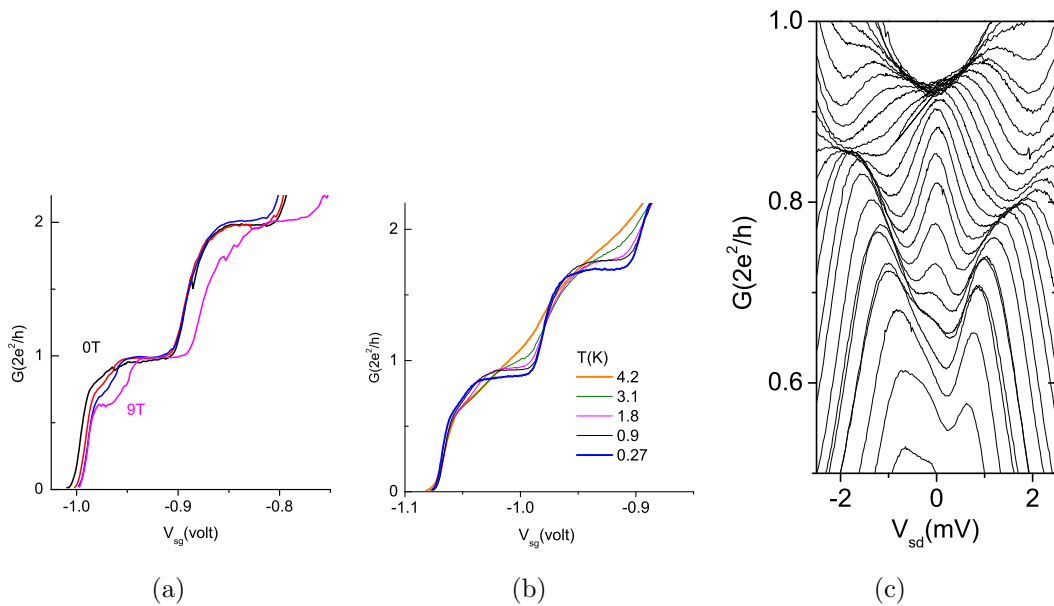


Figure 3.1: (a) $G(V_{sg})$ of a QW with quasi-zero length for in-plane magnetic field $B=0, 4, 7$ and 9 T at 100 mK. (b) $G(V_{sg})$ of a QW at various temperatures for $B=0$. (c) An example of source-drain bias spectroscopy of a QW at $T=0.3$ K. Each trace is for a fixed V_{sg} .

In spite of the substantial works, the mechanisms of 0.7 anomaly and ZBA are much subtle and still under debate. There were inconsistencies among experiments. In more recent reports, the authors claimed that 1D Kondo physics does not fully explain the intricate behaviors of the ZBA.[52, 53, 54] In some devices, the splitting of a zero-bias conductance peak is absent in magnetic fields as high as 10T and at $G < 0.5G_0$, where the channel is fully spin-polarized.[53] In a few devices, splitting occurs in magnetic fields, but two split peaks can resolve back into a single peak by laterally shifting the quantum wire.[53, 54] Additionally, zero-bias conductance peak splitting is almost linearly dependent on the split gate voltage.[54] These findings contradict features of Kondo physics, and further commitment would be required for comprehensive understanding. Comparing the spectroscopies from separate experiments gives some hints on the formation of these anomalies. From Refs.[37, 53, 54, 55, 56], it is worth to notice that the shape, amplitude, and width of the ZBA vary from sample to sample with different 2DEG, device structures, and electric fields. A lateral shift of the QW by electrical means actually changes the microscopic electric field. It has been reported that backscattering in QWs can be controlled by tuning a non-uniform local potential through side gates, implying that electron scattering is sensitive to the details of the potential profile.[57] Therefore, it is reasonable to conjecture that ZBA would be influenced by the physical properties of QWs, such as width, length, or carrier density.

3.3 Physical pictures

The discovery of the 0.7 anomaly and the ZBA implies that electrons are not uncorrelated with each other and inter-particle interactions may be important. Attempts have been made to find a feasible scenario to the findings, however a consensus still lacks. These myriad approaches are diversified and can be categorized into three major pictures: (a) Spontaneous spin polarization, (b) 1D Kondo-type interaction, and (c) inelastic scatterings, as reviewed in detail in the following paragraphs. Spontaneous spin polarization predominantly assumed to be the cause of 0.7 anomaly, while Kondo-type model was associated with the ZBA. These two models actually contradict to each other, since

Kondo-type model requires unbroken time reversal symmetry. The realization of spin-polarization in a non-magnetic semiconductor would be plausible, since physicists have been looking forward to integrate magnetisms into industrial applications.

3.3.1 Spontaneous spin polarization

The notion of spin-polarization in QWs was first proposed by Thomas *et al.*[34] that the 0.7 anomaly evolves to the $0.5G_0$ plateau when the spin degeneracy is lifted. The width of the ‘0.7’ G_0 plateau is linearly dependent with the in-plane magnetic field. Later, Reilly *et al.* reported that the conductance of the anomaly is closer to $0.5G_0$ in a long QW of 2 μm compared with shorter QWs (0.5 μm and quasi-zero in length).[35] The 0.7 anomaly was also reported to be dependent on the carrier density. With increasing the top gate voltage and correspondingly increasing the carrier density, the anomaly moves closer to $0.5G_0$ as shown in Figs. 3.2(a) and (b).[35, 36, 43]

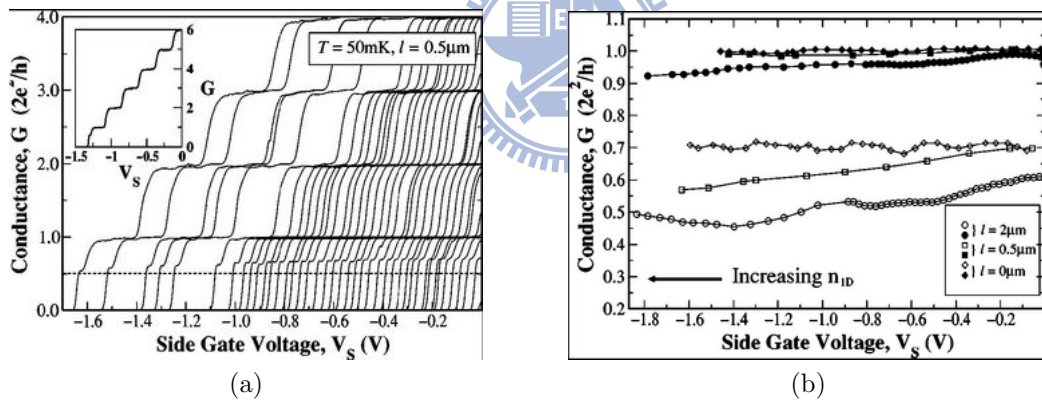


Figure 3.2: (a) Conductance of a $l=0.5 \mu\text{m}$ QW as a function of side gate voltage V_S for V_T (top gate voltage)=560–1500 mV (right to left). (b) Open symbols: anomaly conductance as a function of top gate voltage for QWs with different lengths. Solid symbols: $N=1$ plateaus near G_0 . (After Reilly *et al.*, Ref.[35].)

Spontaneous spin polarization can be realized in a GaAs/AlGaAs two-dimensional-hole-gas (2DHG). Rokhinson *et al.* adopted electron-focusing technique to inject a current from a injector QPC to the detector QPC as shown in Fig. 3.3(a). Due to spin-orbit interaction, the spin degenerated subbands are split. As shown in Fig. 3.3(b), by monitoring the voltage across the detector QPC, two peaks corresponding to spin-up and spin-down are observed when both injector and detector are set at G_0 . When the spin-up subband

of the injector QPC is lifted above the Fermi-energy, e.g. the $G_i=0.66G_0$ trace, only the spin-down peak is observable.[58]

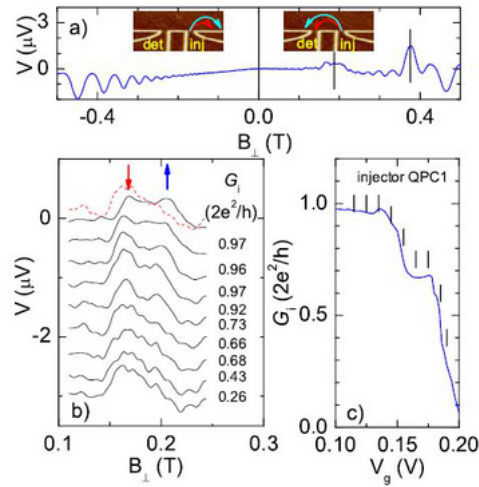


Figure 3.3: Polarization detection via magnetic focusing. (a) The voltage across the detector QPC as a function of the perpendicular magnetic field B_{\perp} . A current of 0.5 nA flows through the injector QPC. The positions of the first two magnetic focusing peaks are marked with vertical lines. The trajectories of the ballistic holes for positive and negative B_{\perp} are shown schematically in the insets. (b) The first focusing peak is measured at different injector conductances with the detector tuned into the middle of the $2e^2/h$ plateau. (c) The gate voltage characteristic of the injector QPC. Vertical lines mark the positions where the curves in (b) are taken. (After Rokhinson *et al.*, Ref.[58].)

Many theoretical proposals have been made to explain the spontaneous spin polarization of 1D electron gas. Reilly *et al.* proposed that spin splits in the QW and the energy of split increases with *increasing* carrier density. Therefore, as the spin gap opens up with the increasing top gate voltage of a QW, the anomaly conductance evolves to $0.5G_0$. [35, 36, 44] The density dependent spin gap may be described by a more microscopic scenario—the deviated tendency of populating the subbands with opposite spins. [59] Graham *et al.* observed that there is energy rearrangement for $\sigma \downarrow$ energy levels when $\sigma \uparrow$ meets $\sigma \downarrow$ in strong in-plane magnetic fields. [60] The energy displacement manifests as discontinuities of these $\sigma \uparrow$ subbands in the transconductance spectroscopies as shown in Fig. 3.4(a) where this features of $1 \uparrow$ and $2 \downarrow$ are highlighted by the dashed frame. Later, the $\sigma \downarrow$ was suggested to be rapidly populating for the V-shape splitting of dc bias spectroscopy shifting to a finite dc bias. [61] For the dc bias spectroscopy in magnetic fields where spin energy rearrangement happens, one of the bias branches was found to

be missing for $1 \uparrow$. [62] Level pinning on $\sigma \downarrow$ was suggested. Both analogs of fast populating and branch missing were found in 0.7 anomaly at $B=0$. E.g., as shown in Fig. 3.4(b), the μ_s branch is missing for $G(V_{sd} = 0) = 0.7G_0$ compared with the expected pattern shown in the right panel.

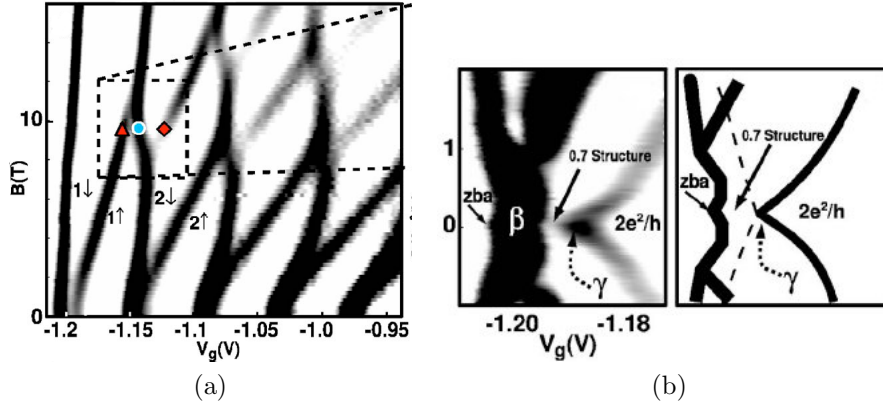


Figure 3.4: (a) Grey-scale diagram of dG/dV_g as a function of V_g for $B = 0$ to 16 T. White represents conductance plateaus, and dark lines correspond to a subband populating. (b) Left panel: Grey-scale of dG/dV_g at $B=0$ as a function of V_{sd} . The left branch is absent. Right panel: Schematic illustration for the expected pattern of the spectroscopy. (After Graham *et al.*, Ref.[62].)

The 0.7 anomaly was suggested to originate from the combination of the aforementioned effects and thermal depopulation. This proposal was supported later by Chen *et al.* by showing that $G(V_g)$ and $\frac{\partial G}{\partial V_g}(V_g)$ as a function of temperature and V_{sd} present odd-even behavior in magnetic fields.[53]

‘Spin density functional theory’ (SDFT) calculation was widely used to numerically investigate the local electron density and self-consistent potential of QWs for the two opposite spins.[63, chap. 7] Exchange and correlation of electrons were usually included in the calculation.[38, 39, 40, 41, 43, 64] Density of one spin was proposed to be larger than the other in the center of a QW as shown in Fig. 3.5(a) by Starikov *et al.* although there are still disagreements among works. The energy potential for $\sigma \uparrow$ is higher than $\sigma \downarrow$ correspondingly as shown in Fig. 3.5(b), and the 0.7 anomaly feature was reproduced due to deviation of transmission between spins, Fig. 3.5(c).

Spin polarization implies two discrete subbands below the Fermi energy for $G < G_0$. Kristensen *et al.* reported that the 0.7 anomaly develops an ‘anomalous subband’ in the transconductance spectrum $\frac{\partial G}{\partial V_g}(V_{sd})$. [55] The linear conductance ($V_{sd} = 0$) in

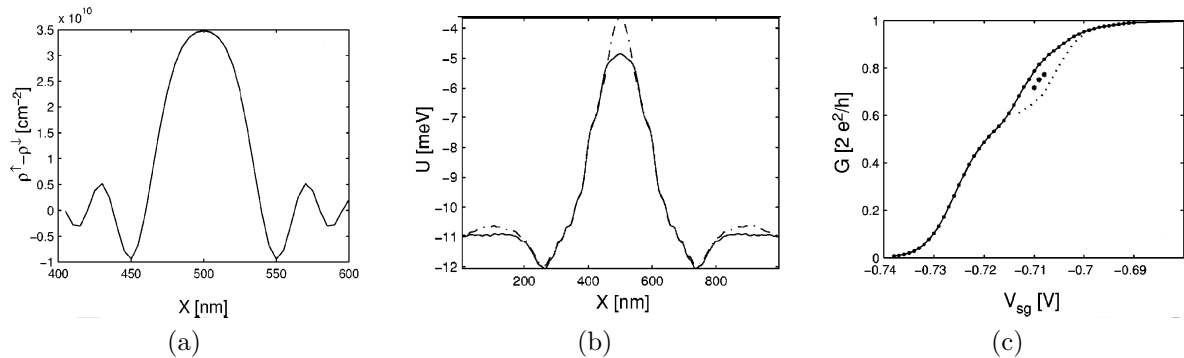


Figure 3.5: (a) Local spin density along the longitudinal axis in the middle of a QW. (b) Self consistent total potential for $\sigma = \uparrow$ (solid) and $\sigma = \downarrow$ (dashed) along longitudinal axis. (c) Numerical results for conductance vs. gate voltage. (solid line) (After Starikov *et al.*, Ref.[39].)

the vicinity of the first plateau decreases with increasing temperature corresponding to thermal excitation. The authors suggested that an extra level exists in addition to the integer plateau. The reducing conductance with increasing temperature as well as the observed conductance shoulder in the non-linear conductance was associated with electron depopulating from the extra energy level. The scenario was explored in another way by studying the shot noise. Besides the $1/f$, telegraph and amplifier noises, the measured noises $S_I(V_{sd})$ are dominant by thermal noise $4k_B T_e g(V_{sd})$ and partition noise $S_I^P(V_{sd})$, where T_e is the electron temperature. The noise factor $\mathcal{N} = \frac{1}{2} \sum \tau_{n,\sigma} (1 - \tau_{n,\sigma}) \propto S_I^P(V_{sd})$, where $\tau_{n,\sigma}$ is the transmission of n -th subband for spin σ . For spin-degenerate case, the shot noise is expected to minimize to zero on a plateau, and maximize as 0.25 for odd integer multiples of $\frac{1}{2}G_0$. Roche *et al.* and Dicarolo *et al.* observed that the shot noise was reduced at the 0.7 anomaly.[65, 66] As shown in Fig. 3.6(a), \mathcal{N} reaches zero for $G = G_0$ and $2G_0$ and \mathcal{N} is suppressed at $G \approx 0.7G_0$. Additionally, the asymmetric single dome of \mathcal{N} becomes symmetric double domes with respect to $0.5G_0$ at $B_{\parallel} = 7.5T$ as shown in Fig. 3.6(b) when spin degeneracy is lifted.

Contradictorily, Thomas *et al.* and Pyshkin *et al.* observed that the 0.7 anomaly approaches $0.5G_0$ also at low density regime.[67, 68] In low density regime, the coulomb interaction dominates over kinetic energy. To reach a minimal total energy for the system (QW), the electrons become crystalized forming the prominent ‘Wigner Crystal’.[69] Klironomos *et al.* proposed that electrons form a zig-zag crystal in a realistic devices.

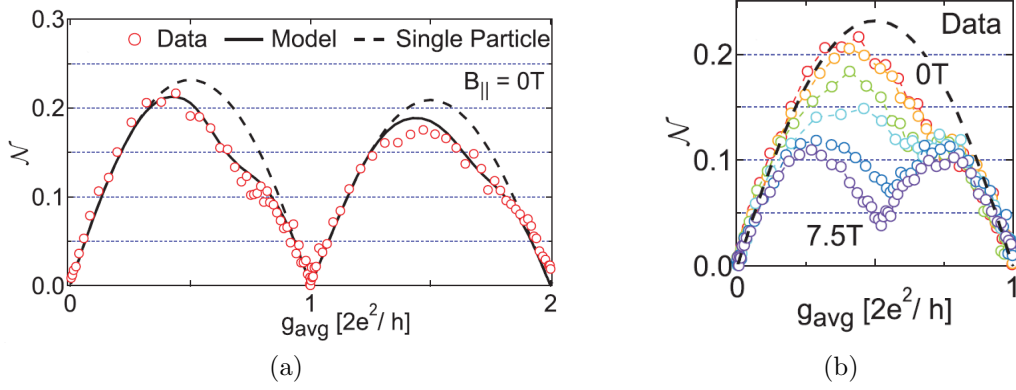


Figure 3.6: (a) Experimental \mathcal{N} as a function of averaged conductance g_{avg} at $B_{||} = 0$ along with model curves (solid and dashed lines). (b) Experimental \mathcal{N} as a function of g_{avg} in the range $0-1(2e^2/h)$ at various $B_{||}$. (After Dicarlo *et al.*, Ref.[65].)

The distance between two particle chains depends on carrier density as well as the type of exchange interaction. When the QWs form a *ferromagnetic* ground state, the system is spin polarized.[70]



3.3.2 Kondo-type interaction

In parallel to spin polarization, Cronenweert *et al.* observed results similar to Kondo effect in QDs.[37] Kondo effect originally describes the logarithmically diverging resistivity at low temperatures in metals doped with dilute magnetic impurities. Begin from Anderson model, one can derived the Hamiltonian for a QD by appropriate basis transformation and approximations. $H_S \approx H_D + H_{LR} + H_S^{(2)}$. Only singly occupied states remain during the basis transformation, since a QD occupied by an odd number of electrons is considered. H_D and H_{LR} are the Hamiltonians of the QD and leads; '(2)' stands for a second order approximation. The Kondo Hamiltonian $H_S^{(2)}$ incorporates two-particle scatterings and reads

$$H_S^{(2)} = \sum_{\nu\nu',\alpha\alpha'} J_{\alpha\alpha'} \mathbf{S}_d \cdot \mathbf{S}_{\nu\alpha,\nu'\alpha'} + \sum_{\nu\nu',\sigma,\alpha\alpha'} W_{\alpha\alpha'} c_{\nu\alpha\sigma}^\dagger c_{\nu'\alpha'\sigma} \quad (3.1)$$

$J_{\alpha\alpha'}$ represents the energy of exchange scatterings, and $W_{\alpha\alpha'}$ represents the energy of potential scatterings. Notice that the first term incorporates spin-spin interaction that

allow spin to flip.[71]

$$\mathbf{S}_d \cdot \mathbf{S}_{\nu\alpha,\nu'\alpha'} = \frac{1}{4} \sum_{i=x,y,z} \sum_{\sigma\sigma',\sigma_1\sigma'_1} (c_{d\sigma}^\dagger \tau_{\sigma\sigma'}^i c_{d,\sigma'}) (c_{\nu\alpha\sigma_1}^\dagger \tau_{\sigma_1\sigma'_1}^i c_{\nu'\alpha'\sigma'_1}) \quad (3.2)$$

Eq. 3.2 is anti-ferromagnetic with the anti-parallel spins for the lowest energy state where $\tau_{\sigma\sigma'}^i$ is the Pauli spin matrices. Exploiting perturbation calculation, it was found that the tunneling rate which is 3rd order in J , $\Gamma_{RL}^{(3)}$, gives rise to the logarithmic divergence in transmission. Fig. 3.7 is the illustration of one of the 3rd processes. The scattering incorporates a medium virtual state and two spin-flips. The density of state at the Fermi level is enhanced due to Kondo resonance. The predicted prominent features of Kondo effect in QDs: (a) Conductance follows a universal form $G(T/T_k) = G_0 \left[\frac{(T_k^*/T)^2}{1+(T_k^*/T)^2} \right]^s$, with $T_k^* = T_k / (2^{1/s} - 1)^{1/2}$ and $s \approx 0.2$ for spin-1/2 system. T_k is the Kondo temperature which follows $\ln(T_k/\sqrt{\Gamma U}) = \pi\varepsilon_0(\varepsilon_0 + U)/\Gamma U$, where U is the charging energy; ε_0 is the single-particle state energy; Γ is the tunneling rate.[72] (b) Kondo resonance takes place at Fermi level, resulting in ZBA by sweeping V_{sd} . (c) The ZBA splits and is suppressed with Zeeman splitting in magnetic fields. There is one thing worth mentioning. Although Kondo effect in QDs requires a singly occupied state as the magnetic impurity, the spin degeneracy should still be conserved. Therefore, spontaneous spin polarization and Kondo effects cannot coincide.

Surprisingly, Cronenweert *et al.* reported measurement results of QWs that were very similar to Kondo Effects in QDs. As shown in Fig. 3.8(a), the experimental data of $G(T/T_k)$ all fall into the same trace in the form of

$$G_{KL}(T) = G(0) \left[1/2 \cdot \left[1 + (2^{1/s} - 1)(T/T_{KL})^2 \right]^{-s} + 1/2 \right] \quad (3.3)$$

where $s=0.22$. The Kondo temperature extracted from fits of this equation are exponentially dependent with the gate voltage; Fig. 3.8(b). ZBA was observed as well, and suppressed in a magnetic field as high as 6 T. [37]

The observations have brought extended discussions about the possibility of spin impurity in a non-magnetic GaAs quantum wire. Interestingly by SDFT calculation, Hirose

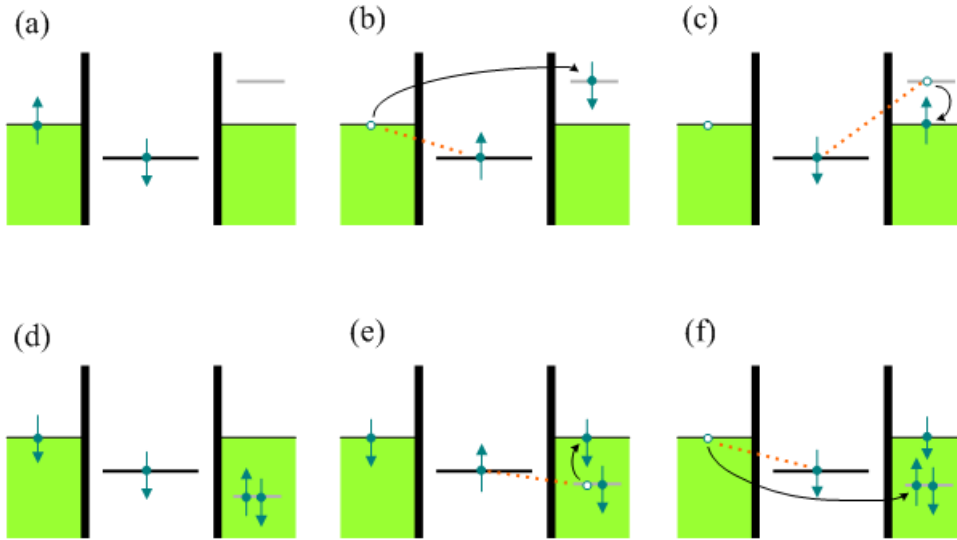


Figure 3.7: Illustration of the two scattering processes (a)–(c) and (d)–(f) that add up and give a logarithmically diverging contribution to the scattering. (a) and (d): initial states; (b) and (e): intermediate states; (c)–(f): final states. The scatterings include two spin-flip.[71]

et al. reported that the energy level of $\sigma \uparrow$ not only deviates from $\sigma \downarrow$, but also includes a local potential minimum along the transport direction, a $\sigma \uparrow$ quasi-bound state, near the pinch-off.[49] The results inspired application of Anderson model in QWs, and the experimental discoveries were reproduced numerically.[48, 50] The extended Anderson model was also utilized to study the shot-noise reduction problem. Golub *et al.* reproduced numerical results comparable to the experiments in Ref.[65] and Ref.[66]. The noise suppression at 0.7 anomaly was suggested to due to the recovery of Kondo resonance in low magnetic fields, since transmissions of both conducting channels reach unitary limit ($G_i \approx e^2/h$). Hsiao *et al.* proposed an alternative scenario for the formation of a quasi-bound state in QWs.[51] Including spin-orbit coupling induced from the out-of-plane electric field $E_z(x)$, which is generated from the applied gate voltage, the effective potential may contain a local minimum. The quasi-bound state was suggested to be more robust in longer QWs or with larger split gate voltages due to stronger nonhomogeneity of E_z .

The magnetic impurity inside a QW was claimed to be existing by the results of the experiment of two coupled QPCs.[73, 74, 75] The authors observed that the conductance of a detector QPC presents a resonance peak when a second QPC reaches pinch-off.

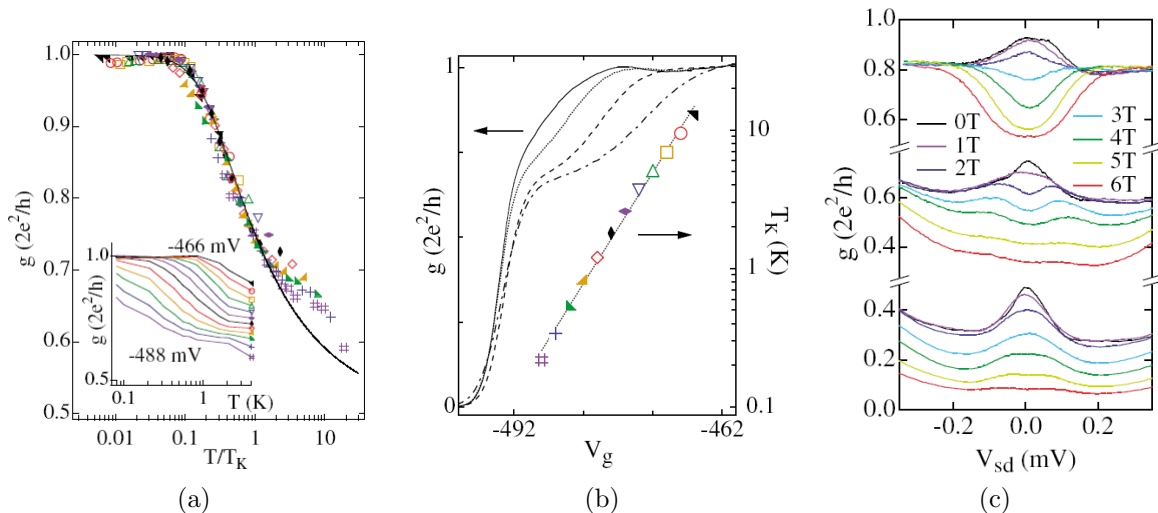


Figure 3.8: (a) Linear conductance as a function of scaled temperature T/T_k . (b) T_k (right axis) obtained from the fits of $g(T/T_k)$ as a function of gate voltage V_g . (c) Evolution of the ZBA with in-plane B for various V_g . (After Cronewett *et al.*, Ref.[37].)

The mechanisms of coupling between the two QPCs were proposed and described by Puller *et al.*[76] The authors claimed that a magnetic moment in a QPC would induce an enhancement in the density of state in another QPC through tunnel coupling.

3.3.3 Inelastic backscatterings

In contrast to the Kondo temperature dependence of the conductance close to the 0.7 anomaly, Kristensen *et al.* reported thermal activated dependence.[55] Considering electron-phonon scattering [Fig. 3.9(a)] and the backscattered current

$$\delta I = -2e \int_{-\infty}^{\infty} [\tau_R^{-1}(E)f_R(E) - \tau_L^{-1}(E)f_L(E)] dE \quad (3.4)$$

Seelig *et al.* reproduced exponential temperature dependence for $T \lesssim T_A$ from Fermi-golden rule approach.[77] $\tau_{R(L)}^{-1}$ is the rate that the right-moving electrons being scattered into left moving states. Negative conductance correction δG due to the increased bias associated with ZBA was also suggested due to the increased available electrons for backscattering.

Lunde *et al.* considered backscattering caused by electron-electron scatterings shown in Fig. 3.9(b) and applied Fermi's golden rule to simulate the backscattered current.

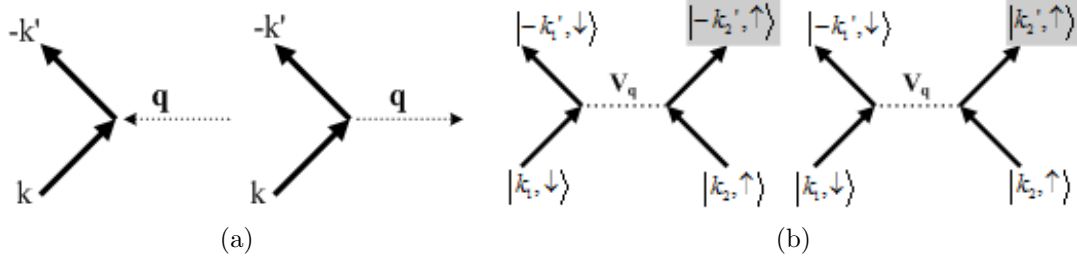


Figure 3.9: (a) e-ph scatterings considered in Ref.[77]. (b) e-e scatterings considered in Ref.[78]. k, k', k_i , and k'_i are positive.

Negative δG as a function of temperature and voltage bias was also suggested.[78] Similar calculations were extended to three-particle scattering, and exponential dependence of the conductance was found.[79] Alternatively, Meidan *et al.* modeled a single-mode QW as an interacting Tomonoga-Luttinger-Liquid(TLL) and the contact leads as a noninteracting TLL. Two-particle scattering was found to be relevant for large bias voltage and enhanced by the Coulomb interaction for low carrier density. ZBA was reproduced due to the increasing backscattering current with increasing V_{sd} as shown in Fig. 3.10.[80]

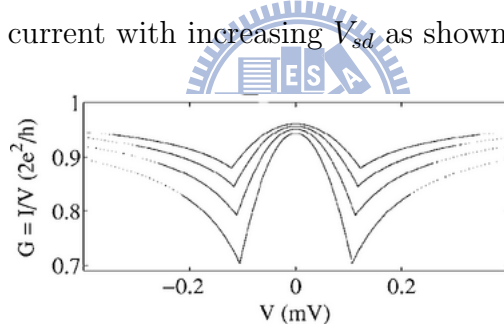


Figure 3.10: $G = dI/dV_{sd}$ as a function of V_{sd} , in the presence of single-electron and two-electron scatterings. Different traces are plotted at a fixed Fermi energy ranging from 5 K (the lowest curve) to 8 K in steps of 1 K. The GaAs parameters for this simulation are $L=1 \mu\text{m}$ and $T=80 \text{ mK}$. (After Meidan *et al.*, Ref.[80].)

Rech *et al.* considered equilibration due to weak e-e scattering inside an *infinitely long* QW. Particle current equation $\frac{2e^2}{h}V = I - e\dot{N}^R$, as well as the energy current equation $j_E^R[l] + j_E^L[r] = j_E - \dot{E}^R$ were derived. \dot{N}^R is the rate of the number change of right-movers that are scattered to be left-movers due to e-e scattering. \dot{E}^R is the rate of energy transfer of right movers, j_E is the net energy current of the right movers, and $j_E^{R(L)} [l(r)]$ is the energy current of right (left) movers in the left (right) lead. Applying distribution function in the stationary reference frame to evaluate the final result, a quadratic temperature dependence of the negative conductance correction δG was suggested.[81] The calculation

was also extended to study the case where the length is finite while the equilibration is partial.[82]

Notice that so far, the negative conductance correction due to backscattering does not relate to electron spins. Proposals that have to do with spin were made as well. Tokura *et al.* considered backscattering due to magnon scattering in a 1D spin anti-parallel electrons.[45] In analogy with Ref.[45] Aryanpour *et al.* modeled a QW by 1D itinerant electrons with spin-spin near-neighbor interaction $H_S = \sum_p (J_0 \alpha_p^2 \vec{s}_p \cdot \vec{s}_p + J_1 \alpha_p \alpha_{p+1} \vec{s}_p \cdot \vec{s}_{p+1})$, resembling a magnetic lattice.[83] With the use of Monte Carlo approach, the author reproduced 0.7 anomaly features with respect to in-plane magnetic field and temperature and suggested incoherent scattering as the origin of the 0.7 anomaly.

For a purely 1D system, it has been well established that the Hamiltonian $H = H_0 + V$ can be bosonized given the approximation of linearizing the dispersion at the Fermi energy. The behaviors of the electrons look like collective excitations of two different quasi-particles, charge and spinon. $H = H_\rho + H_\sigma$. $H_\nu = \frac{1}{2\pi} \int dx \left[u_\nu K_\nu (\pi \Pi_\nu(x))^2 + \frac{u_\nu}{K_\nu} (\nabla \phi_\nu(x))^2 \right]$ where $\nu = \rho$ (charge) and σ (spinon). K_ν is the interaction factor, u_ν is the velocity, and Π_ν and ϕ_ν are the field operators of conjugate momentum and displacement, respectively.[84] The spin-charge separation is unique to the TLL. Matveev suggested that the electrons in a QW form Wigner Crystal near the pinch-off due to the relatively low density and high repulsive energy and can be modeled by antiferromagnetic spin chain; $H_\sigma = \sum_l J \mathbf{S}_l \cdot \mathbf{S}_{l+1}$. The authors derived that spin-charge separation approach is still valid in Wigner Crystal. By analyzing the energy dissipation, the resistance of a low density QW is found also to separate into two parts, $R = R_\rho + R_\sigma$. $R_\rho = h/2e^2$ while R_σ depends on the relative strengths of J and temperature T . For $T \lesssim J$ the spin sector travels through the QW without being scattered and $R_\sigma = 0$. On the other hand, for $T \gg J$ the bosonization is violated and the spin-sector is backscattered giving $R_\sigma = h/2e^2$ and the conductance approaches e^2/h . The temperature dependence on the backscattered current was expected to be thermally activated $R_\sigma \sim \exp(-\frac{\pi J}{2T})$. The low temperature conductance of a QW with a *finite* length was suggested lying between e^2/h and $2e^2/h$ which was associated with the 0.7 anomaly because of partially bosonized electrons due to effectively weak

interaction.[46, 47]

3.4 Device arrangements

In the following, we focus on the source-drain bias spectroscopy and temperature dependent differential conductance at zero-bias of QWs in the range of $G < G_0$. QWs with different channel lengths and carrier densities are studied. The ZBA is found to be suppressed by either increasing channel length or decreasing electron density. The temperature dependence of differential conductance at zero-bias follows well the thermal activation behavior below a cutoff temperature. Moreover, a correlation among the activation temperature, cutoff temperature, and ZBA width is found. The results indicate that the conductance reduction at finite temperatures and finite biases should be connected by the same physics, and imply that electron scattering plays a dominant role in both ZBA and temperature dependent conductance.

Electron beam lithography along with thermal deposition were used to fabricate metallic gates on the (100) plane of the substrate. A quasi one dimensional quantum wire can be formed by depleting the 2DEG 93 nm beneath the negatively biased split gates pair. The length (L) of the QWs ranges from quasizero to 5 μm , while the nominal gap width is kept constant at 0.45 μm . A metallic top gate (tp) was fabricated on top of the split gates, isolated by a 100 nm thick dielectric layer of cross-linked polymethylmethacrylate, to control the carrier concentration. Measurements were performed mainly in Heliox VT ^3He cryostat and occasionally in the Minidil OD70 dilution refrigerator. Differential conductance measurement was carried out by four-probe ac lock-in technique at 51 Hz with a small excitation voltage of 10 μV .

3.5 Density and length dependences of the ZBA

When a negative voltage is applied to a pair of split gates, the potential depletes the 2DEG to form a 1D channel resulting in a typical quantized conductance. Conductance versus split gate voltage of four samples with different QW lengths, quasi-zero, 0.5, 0.8,

2, and 5 μm , are plotted in Fig. 3.11, revealing that there are conductance plateaus due to the transmission of 1D subbands for QWs. The plateaus can be aligned exactly to the integer multiples of G_0 by subtracting the series resistance of bulk 2DEG from the data, such as in Ref.[67] by Thomas *et al.* Here, we present the raw data since the series resistance does not affect our results. For QWs of various lengths, quantized plateaus are well developed for $L \leq 2 \mu\text{m}$, implying that the mean free path is much longer than the channel length. For a $L=5 \mu\text{m}$ QW, the quantization steps remain the same, but the quantized conductance is lower compared with the $L \leq 2 \mu\text{m}$ QWs, indicating that the QW is slightly diffusive. The presented transport for QWs with lengths less than 2 μm is indeed within the ballistic regime. Occasionally, charges can be trapped in samples during the cooling process and serve as extra scatterers to degrade conductance plateaus. This would not apply, however, to our work. The systematic behaviors reported here were obtained from 13 samples through many thermal cycles. It should be noted that transport behaviors depend on the geometry of the QW inside, but not outside of the channel. For example, no significant difference is noted between the T-bar and straight-bar split gates. This is reasonable because the depletion regions isolate a confined QW from the 2D electron sea.

Electron transport is sensitive to carrier density, which can be effectively tuned by biasing the top gate voltage V_{tp} in the heterostructures, in either 1D or 2D.[85] Transconductance spectroscopy, which is referred to as the half-plateau method, showed that carrier density is effectively changed by tuning V_{tp} . [86] In Figs. 3.12(a)-(c), three conductance traces for a $L=0.5 \mu\text{m}$ QW with $V_{tp}=+0.4$, -0.1 , and -1.45 V at $T=0.3$ K are shown as black lines. The threshold V_{sg} of the pinch-off voltage becomes less negative from left to right, implying that carrier density is decreased with decreasing V_{tp} . Once the carrier density is substantially reduced, the quantized plateaus disappear while a quasi-shoulder appears at $\sim 0.5G_0$ (Fig. 3.12(c)). Some corresponding conductance traces at different temperatures are also plotted in Figs. 3.12(a)-(c). Both Figs. 3.12(a) and 3.12(b) show that when temperature is increased from 0.3 K to 4.2 K conductance decreases in the vicinity of the first plateau. A quasi-shoulder forms near $0.7G_0$ while the plateaus are

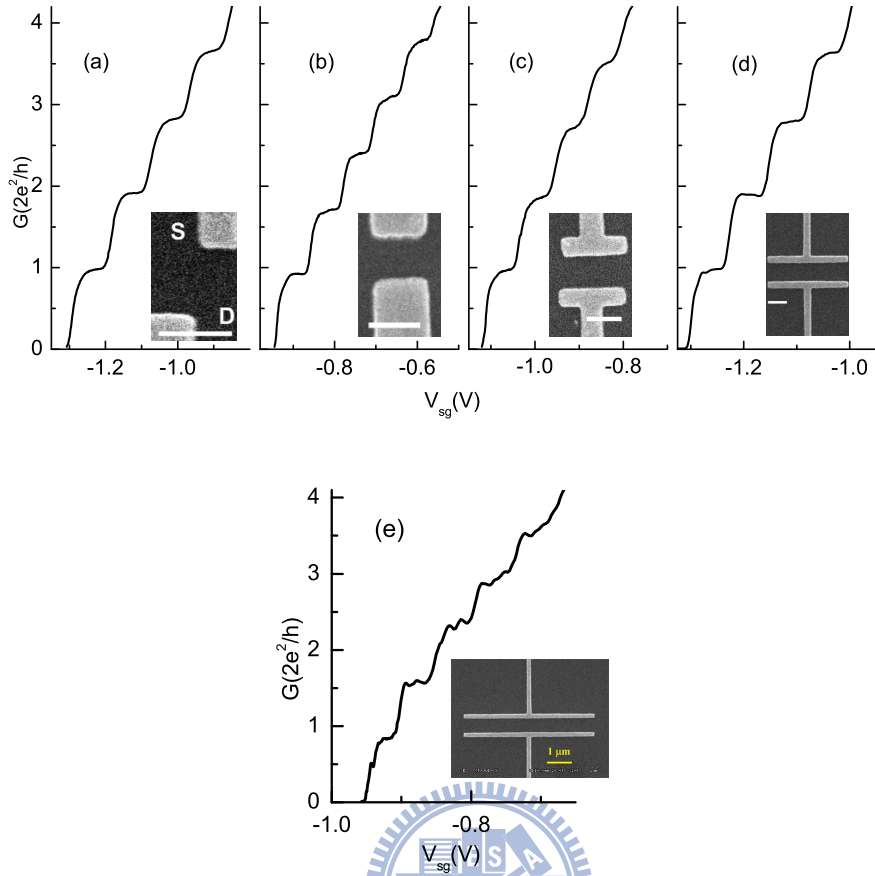


Figure 3.11: $G(V_{sg})$ and micrographs of QWs of various lengths: (a) quasi-zero, (b) $0.5 \mu\text{m}$, (c) $0.8 \mu\text{m}$, (d) $2 \mu\text{m}$, and (e) $5 \mu\text{m}$. The scale bars in (a)–(d) (white bars in the insets) indicate a length of $0.5 \mu\text{m}$. The yellow scale bar in (e) indicates a length of $1 \mu\text{m}$. The top gate is grounded for all four datasets.

washed out. The phenomenon is a typical feature of the 0.7 anomaly.[37] For the same QW with more negative V_{tp} in Fig. 3.12(c), conductance traces at different temperatures remain almost the same. Notice that the curves of higher temperatures are horizontally shifted for clarity in Fig. 3.12(c). As expected, conductance is not sensitive to temperature in the sample with low carrier density, while a clear temperature induced conductance reduction around $0.7G_o$ occurs in the sample with high carrier density.[67]

We investigated the source-drain bias spectroscopy by sweeping a dc source-drain voltage V_{sd} across a confined QW and measuring the differential conductance $G=dI/dV_{sd}$. Figs. 3.12(d)-(f) show the spectroscopies $G(V_{sd})$ against V_{sg} of this sample for the three identical top gate voltages at $T=0.3 \text{ K}$. For $V_{tp}=+0.4\text{V}$ in Fig. 3.12(d), the differential conductance exhibits clearly a series of single peak centered at $V_{sd}=0$ for $G<G_o$ refer-

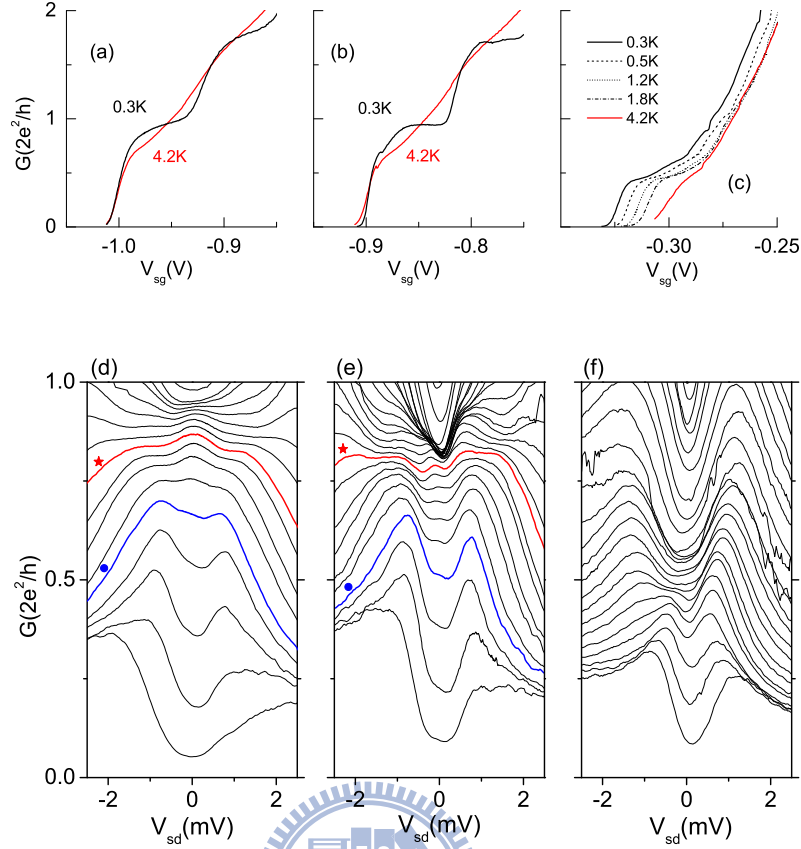


Figure 3.12: (a)-(c): Zero-bias differential conductance versus split gate voltage of a $L=0.5 \mu\text{m}$ QW for $V_{tp} =$ (a) $+0.4 \text{ V}$, (b) -0.1 V , and (c) -1.45 V , respectively, at various temperatures. (d)-(f): Source-drain bias spectroscopies of the same sample at the same top gate voltages at 0.3 K . (d) $V_{tp} = +0.4 \text{ V}$. V_{sg} is from -938 to -1002 mV in 4 mV steps. Red (star-labeled) and blue (dot-labeled) traces indicate $V_{sg} = -970$ and -986 mV , respectively. (e) $V_{tp} = -0.1 \text{ V}$. V_{sg} is from -819 to -900 mV in 3 mV steps. Red (star-labeled) and blue (dot-labeled) traces indicate $V_{sg} = -873$ and -891 mV , respectively. (f) $V_{tp} = -1.45 \text{ V}$. V_{sg} is from -280 to -324 mV (top to bottom) in 2 mV steps.

ring to as ZBA, e.g. the star-labeled and the neighboring curves. The feature is novel and distinguishable from the bell shaped structure of the non-linear conductance of the transmission of the subbands.[28] Based on the source-drain bias spectroscopies of numerous samples at a series of V_{tp} , ZBA becomes weaker with decreasing carrier density. Specifically, the ZBA at $V_{tp} = -0.1 \text{ V}$ (Fig. 3.12(e)) is narrower than at $V_{tp} = +0.4 \text{ V}$ (Fig. 3.12(d)), and disappears entirely at $V_{tp} = -1.45 \text{ V}$ (Fig. 3.12(f)). We characterize the width of a ZBA by ΔV_{sd}^{ZBA} , the source-drain voltage difference between the “peak” and the “bottom” of the ZBA. From the star-labeled curve to the dot-labeled curve in Fig. 3.12(d), ΔV_{sd}^{ZBA} decreases from $\sim 750 \mu\text{V}$ to $\sim 280 \mu\text{V}$ with decreasing V_{sg} . Beyond the

dot-labeled curve, the ZBA is absent for $V_{sg} < -986$ mV. Similar trend holds in Fig. 3.12(e). The width drops from ~ 250 μ V (the star-labeled curve) to ~ 160 μ V (the dot-labeled curve) and the ZBA disappears for $V_{sg} < -891$ mV. As to the sample with the lowest carrier density in Fig. 3.12(f), no ZBA is present for all split gate voltages.

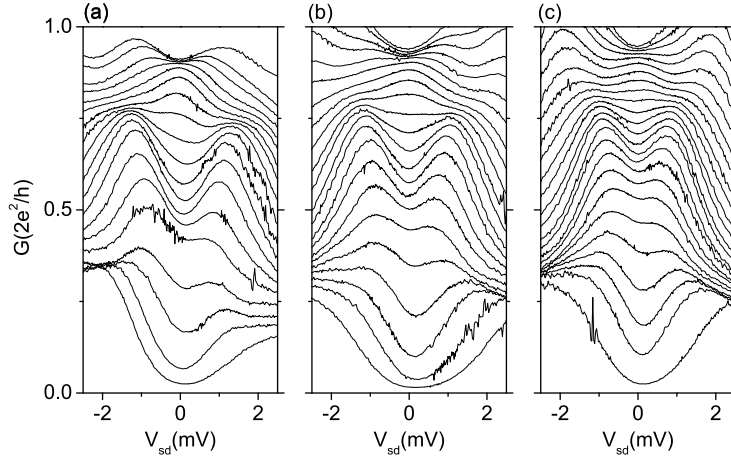


Figure 3.13: Source-drain bias spectroscopies of a quasi zero length QW at various V_{tp} at 0.3 K. (a) $V_{tp} = +0.2$ V. V_{sg} is from -1375 to -1429 mV in 3 mV steps. (b) $V_{tp} = -0.5$ V. V_{sg} is from -945 to -1008 mV in 3 mV steps. (c) $V_{tp} = -1$ V. V_{sg} is from -660 to -710 mV (top to bottom) in 2 mV steps.

Similar evolution of the ZBA as a function of V_{tp} is reproducible in other samples. Fig. 3.13 shows the spectroscopies of a $L \sim 0$ quantum wire for three different V_{tp} . The ZBA is the strongest for $V_{tp} = +0.2$ V in Fig. 3.13(a). With V_{tp} decreased to -1 V, the ZBA becomes much weak in amplitude and width Fig. 3.13(c) shown. The observations evidence that ZBA is suppressed by decreasing the carrier density.

A robust 0.7 anomaly along with the absence of ZBA in ultra-low-disordered QWs was reported by Reilley *et al.*[36] They suggested that carrier density induced enhancement in spin splitting results in a spin gap.[36] The observation of the systematic evolution of ZBA with respect to carrier density inspires an alternative thought. From electron-electron interaction (EEI) perspective, a system of lower carrier density has, in general, stronger EEI. It was well established that EEI contributes a Coulomb anomaly in the density of states which brings about a tunneling conductance gap at $T=0$ and a negative tunneling conductance cusp at finite temperatures.[87, 88] This could suppress the ZBA in a low

carrier density QW. One would expect that the ZBA depends on QW geometry which affects EEI. To investigate the influence of QW length on the effect, we systematically studied the source-drain bias spectroscopies of QWs with quasi-zero $\leq L \leq 5 \mu\text{m}$.

The results presented in Fig. 3.12 imply that there will be a weak but non-zero ZBA for a $L=0.5 \mu\text{m}$ QW at $V_{tp}=0 \text{ V}$. Here, we present $G(V_{sd})$ against V_{sg} for other five samples with $L=\text{quasi-zero}, 0.25, 0.8, 2, \text{ and } 5 \mu\text{m}$, at $V_{tp}=0$ and $T=0.3 \text{ K}$ in Fig. 3.14. The $L=\text{quasi-zero}$ QW has a very strong ZBA. In Fig. 3.14(a), ΔV_{sd}^{ZBA} decreases from $\sim 1.2 \text{ mV}$ (the star-labeled curve) to $\sim 290 \mu\text{V}$ (the dot-labeled curve) with decreasing V_{sg} . The $L=0.25 \mu\text{m}$ QW has a slightly weaker ZBA (Fig. 3.14(b)). Both QWs have a relatively wider and taller conductance peak in their spectroscopy curves compared with the $L=0.5 \mu\text{m}$ QW (Fig. 3.12). ZBA completely disappears in the other three QWs of $L=0.8, 2, \text{ and } 5 \mu\text{m}$ shown in Figs. 3.14(c)-(e). Therefore, the ZBA is suppressed by increasing QW length. These data are not consistent with Koop *et al.*, who reported no length dependence of ZBA for QWs ranging in length from 0.1 to $0.45 \mu\text{m}$. [89] It is slightly difficult to distinguish the difference of ZBA among our QWs in the range of 0.2 to $0.5 \mu\text{m}$. By also including the data for the quasi-zero and longer QWs, however, we provide a full picture of the evolution of ZBA with respect to QW length. The $L \leq 2 \mu\text{m}$ QWs are at least a few times shorter than the mean free path and hence, the diffusive scattering is negligible. In all of these samples, the differential conductance traces at zero-bias demonstrated many clear quantized conductance plateaus. This feature is robust to thermal cycling, indicating that the ballistic transport is not affected. It has been suggested that spin polarization can be enhanced in long QWs to split the ZBA. [41, 35] In our long QWs, we did not observe any splitting of the zero-bias conductance peak. We suggest that the increase in QW length allows for additional scattering of conducting electrons, which results in enhanced EEI and correspondingly, a diminished ZBA. For the $L=5 \mu\text{m}$ QW, the lowered quantized conductance could be attributed to diffusive scattering. As the conductance quantization is sustained, however, the transport is mostly ballistic. In this case, we believe that the increased channel length still plays a dominant role in suppressing ZBA.

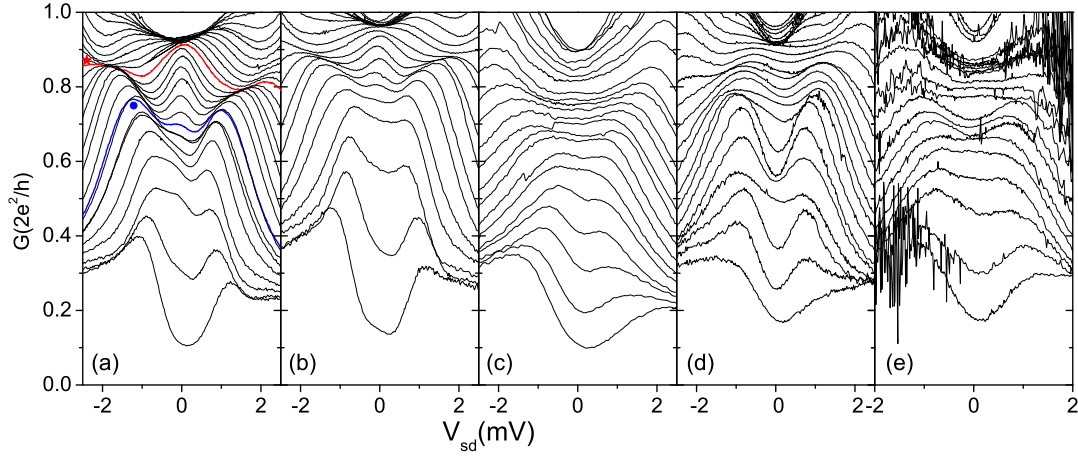


Figure 3.14: Source-drain bias spectroscopies of QWs of several lengths at 0.3 K for $V_{tp}=0$. (a) L =Quasi-zero. From top to bottom, V_{sg} decreases from -1450 to -1558 mV in 4 mV steps. Red and blue traces indicate $V_{sg}=-1498$ (star-labeled) and -1526 mV (dot-labeled), respectively. (b) $L=0.25 \mu\text{m}$. V_{sg} is from -914 to -1002 mV in 4 mV steps. (c) $L=0.8 \mu\text{m}$. V_{sg} is from -570 to -612 mV in 2 mV steps. (d) $L=2 \mu\text{m}$. V_{sg} is from -810 to -858 mV in 2 mV steps. (e) $L=5 \mu\text{m}$. V_{sg} is from -920 to -958 mV in 2 mV steps.

3.6 The conductance reduction at finite temperatures and biases



One more interesting phenomenon is that ZBA seems to be accompanied by a temperature induced conductance reduction for $G < G_0$. Fig. 3.12 shows the representing behavior for all other samples in the study of carrier density effect. The correlation between the ZBA and the temperature induced conductance reduction will be determined in this section. Three $G(T)$ traces of a L =quasi-zero QW are plotted in the inset of Fig. 3.15(a) to show the typical temperature dependent conductance behavior. The zero-bias differential conductance decreases with increasing temperature. Although temperature dependence of the 0.7 anomaly has been intensively studied for quite some time, the results vary widely.[37, 52, 53, 55, 90] Among them two types were mostly proposed, Kondo-like[37] and activated temperature dependent behaviors.[52, 53, 55, 90] Numerical fittings using both Kondo-like model Eq. 3.3 and thermal activation models to the data are shown as dashed and solid lines in the inset of Fig. 3.15(a), respectively. Although numerical fit

using this model can describes part of data, there is no systematic relation between the fitting parameter T_{KL} and split gate voltage.) Both models seem to describe experimental results well at low temperatures. The applicable temperature range, however, is wider and the fitting parameters obtained from the fit exhibit a systematic variation in the activation model. Hence, we adopted the activation model to analyze the data.

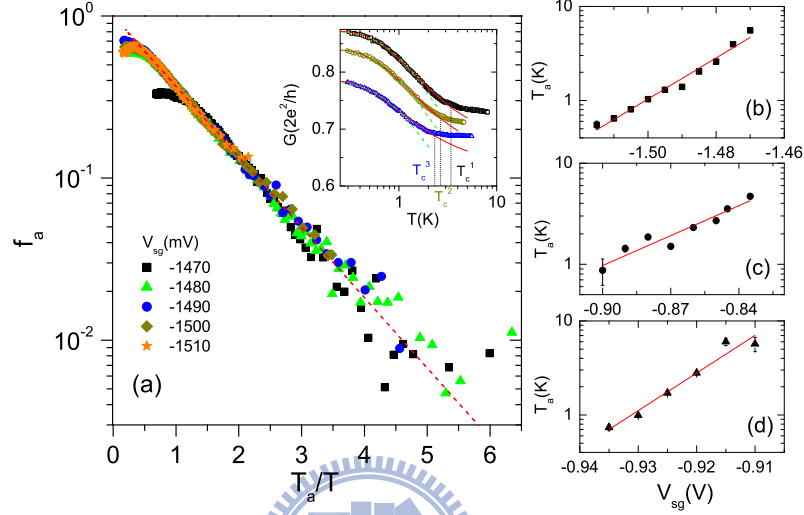


Figure 3.15: (a) Semilogarithmic plot of f_a vs. $\frac{T_a}{T}$ for a L =quasi-zero QW against a series of V_{sg} at $V_{tp}=0$. (see text) The dashed line is the least square root linear fit. Inset: Three typical traces of measured $G(T)$, along with the simulated curves of the activation model (solid lines) and Kondo-like model (dashed lines). The cutoff temperature at which $G(T)$ deviates from activation behavior is located and indexed as T_c^i for a split gate voltage V_{sg}^i . (b)-(d): Activation temperature vs. split gate voltage at $V_{tp}=0$ for (b)-(c) two L =quasi-zero QWs and (d) a $L=0.5 \mu\text{m}$ QW. Lines were fitted using the linear least square root regression method.

The temperature dependent conductance based on the thermal activation model is expressed as

$$G(T) = G(0) \left(1 - C \cdot e^{-T_a/T}\right) \quad (3.5)$$

where $G(0)$ is the measured conductance at the base temperature. T_a and C are the fitting parameters.[55] Rearranging the equation, f_a defined as $\frac{1}{C} \left(1 - \frac{G(T)}{G(0)}\right)$ equals $e^{-\frac{T_a}{T}}$. Semilogarithmic plots of f_a versus T_a/T for a L =quasi-zero QW against a series of V_{sg} at $V_{tp}=0$ are presented in Fig. 3.15(a) to confirm the typical thermal activation behavior. After scaling T by T_a in this semilogarithmic Arrhenius plot, all traces generally collapse onto a universal curve following a linear relation down to $\sim 0.2T_a$ ($T_a/T \sim 5$). The dashed

line is the least square root linear fit. Thermal activation behavior is valid up to a “cutoff” temperature, T_c . In Fig. 3.15(a), traces of f_a show a downward trend deviating from the linear fit at low values of T_a/T . T_c was determined by finding the temperature at which the data begins to deviate from the fit. As an example, T_c for three V_{sg} is labeled in the inset of Fig. 3.15(a). The evolution of T_c with respect to either V_{sg} or $G(0)$ is obtained for $G < G_o$. As $G(0)$ decreases, T_c decreases and so does T_a . T_a increases with increasing V_{sg} from sub-Kelvin for $G(0) \sim 0.5G_o$, to a few Kelvin in the vicinity of the first plateau. The activation temperature, as a function of V_{sg} for three samples, is shown in Figs. 3.15(b)-(d). Other samples, except those with either low carrier density or long channel length, exhibit similar behavior with an exponential dependence of the activation energy on split gate voltage, which is consistent with previous experimental findings by other groups.[52, 53] Bruus *et al.* proposed that the observed activated behavior in G is related to the thermal depopulation of a subband with a gate voltage dependent subband edge.[90] The power law relation between the activation energy and split gate voltage was experimentally obtained by Bruus *et al.*[55, 90]

It is quite interesting that there is not only a correlation between T_a and T_c , but also a close relation between T_a or T_c and the ZBA width for $G \lesssim 0.9G_o$. The relations can be clearly demonstrated by scaling $(G(0), T_c)$, $(G(0), T_a)$ extracted from the temperature dependent conductance, and $(G_{peak}^{ZBA}, \Delta V_{sd}^{ZBA})$ extracted from the source-drain bias spectroscopy on the same plot as shown in Figs. 3.16(a) and (b) for two L=quasi-zero QWs. G_{peak}^{ZBA} is the conductance at the ZBA peak at the base temperature. In Fig. 3.16(a), three traces of $(G(0), 2k_B T_c)$, $(G(0), 5.5k_B T_a)$, and $(G_{peak}^{ZBA}, e\Delta V_{sd}^{ZBA})$ collapse onto one curve for one sample. Likewise in Fig. 3.16(b), three traces of $(G(0), 3k_B T_c)$, $(G(0), 7k_B T_a)$, and $(G_{peak}^{ZBA}, e\Delta V_{sd}^{ZBA})$ collapse also onto one curve for the other sample. Although the factors are slightly different, the scenario is robust. Three characteristic quantities, T_c , T_a , and ΔV_{sd}^{ZBA} , decrease monotonically with decreasing zero-bias differential conductance.

While the 0.7 anomaly manifests at high temperatures, it is also observable at finite source-drain biases at low temperatures, seen as bunches of curves e.g. for $|V_{sd}| \gtrsim 0.6$ mV in Figs. 3.16(a) and (b). For a specific V_{sg} , increasing $|V_{sd}|$ from zero-bias reduces the

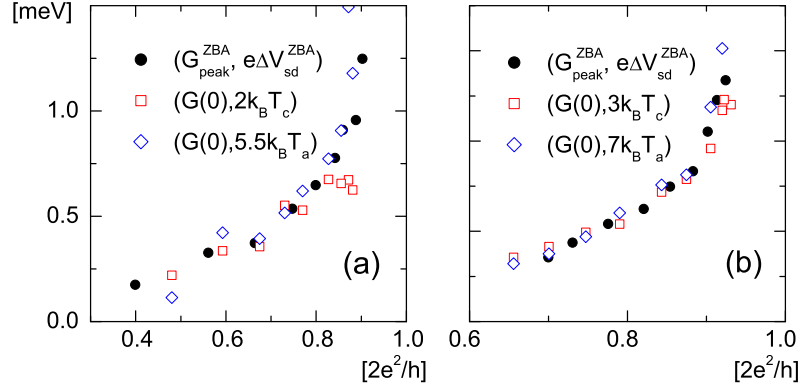


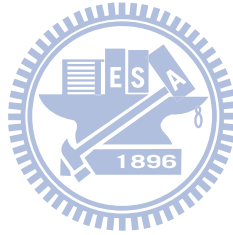
Figure 3.16: $(G_{peak}^{ZBA}, e\Delta V_{sd}^{ZBA})$, $(G(0), \text{scaled } T_c)$, and $(G(0), \text{scaled } T_a)$ on the same plot for two L=quasi-zero QWs.

conductance, while the relation of G versus V_{sd} forms the ZBA. The fact that the three traces obtained from two different measurements match suggests that the temperature and bias induced conductance reductions are strongly correlated.

Theoretical works suggested that conductance decreases with increasing energy scale (either bias voltage or temperature) under the consideration of backscattering.[77, 78] Increasing either the bias or temperature enlarges the momentum space of integration and henceforth increases backscattered current or resistance. Calculations showed that multiple-electron backscattering becomes frequent as the source-drain bias increases, leading to a reduced conductance, manifesting as ZBA, whereas enhanced EEI prompts strong multiple-electron scattering to weaken the ZBA.[78, 80] On the other hand, several groups have suggested that electron-electron scattering brings about a reduced conductance at elevated temperatures.[47, 78, 79, 80, 91, 92] The temperature induced conductance correction δG was suggested to follow an activation law.[79] Thermal activated dependence of conductance can also be predicted by taking the backscattering of electrons mediated by acoustic phonons into account.[77] The same mechanism can describe the negative correction to conductance by the finite source-drain bias in ZBA as well. The theoretical proposals provide a picture that electron backscattering results in ZBA and temperature dependent conductance, which may explain our results.

3.7 Conclusions

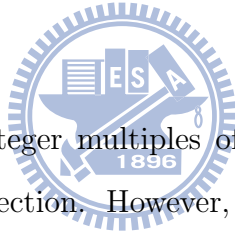
We provided evidence that ZBA depends systematically on physical properties of QWs. The amplitude and width of the ZBA decrease with either decreasing carrier density or increasing channel length, wherein the scattering rate of electrons is expected to increase. The ZBA is totally suppressed by strong scattering, in a either very low carrier density or long QW. The activation model is preferable for describing the temperature dependent conductance reduction. Moreover, the conductance dependence on temperature departs from the activation model at a cutoff. Scaling of the cutoff energy, activation energy, and ZBA width indicates that the temperature and bias induced conductance reductions are affected by the same physics. Theoretical predictions taking electron backscattering into account are in accordance with our results. We believe that electron scattering has a central role in characterizing the ZBA in QWs.



Chapter 4

Conductance and spectroscopy of disordered quantum wires

4.1 Introduction



Conductance quantization of integer multiples of G_0 requires a perfect conductor, i.e. a unit transmission without reflection. However, real devices in nature always to some extent contain imperfections. When scatterers present in a quantum wire (QW), the electrons would be backscattered and interferences would occur.[19, 93, 94, 95] Lattice defects, randomly distributed ionized donors, or edge roughness can be sources of impurity. The effects of impurities on the transport have been widely explored theoretically. It has been shown that impurities induce quasi-bound states.[96] The quasi-bound state gives rise to conductance oscillations[19, 96, 97, 98, 99, 100, 101] due to the interference between incident and reflected electrons. Additionally and more subtly, the quasi-bound states offset the pinch-off voltage due to the additional resonant levels[93, 101, 102]. In previous experiments, the linear conductance resonances in unintentionally disordered QWs were attributed to a single impurity[97], interface roughness[103], random potential fluctuations[12, 22], and length resonances[104]. However, experimental observations directly associated with the aforementioned predictions are rare.

In this chapter, we present the linear conductance, and additionally the source-drain

bias spectroscopies of clean and disordered QWs against thermal cycling and lateral shifting which change the impurity configurations. When the impurity arrangements are changed, the fine structures in linear conductance and the spectroscopy alter accordingly. Theoretical predictions are in congruence with the experimental results. It is also found that the resonant state in spectroscopies influences the characteristics of the zero bias anomaly of QWs.

4.2 Transport features in the presence of impurities

Since the discovery of conductance quantization in GaAs/AlGaAs quantum wires, enormous amount of theoretical works have been contributed to discuss the transport in the presence of impurities. Most of them were numerical calculations, since it is difficult to acquire analytical resolutions. However, similar results and consensuses were deduced about the effect of impurity on the transport. These features are rephrased in the following briefly:

- Conductance quantization is degraded.
- Conductance of plateaus is lowered.
- Additional structures occur due to multiple scattering electron waves.
- The fine structures are sensitive to the impurity configurations.
- Quasibound states are developed and conductance resonance appears.
- Subband energy may be shifted.

In the following, some of the most prominent proposals and numerical works are reviewed in detail. Due to the effects of impurities, the conductance quantization is degraded in the forms of lowered plateau conductance and smearing of steps. Additionally, additional fine structures due to multiple scatterings of electron waves were suggested.[19, 22, 93, 94, 95, 98, 100, 102] Chu *et al.* considered an isotropic scatterer placed 5 nm away from the center of a 1D channel. [19] Making use of quantum scattering theory and Landauer formula, the conductance as a function of channel width was

calculated. Conductance dips are perceptible for a weak *attractive* impurity. [Fig. 4.1(a)] Resonant peaks and plateau smoothing are visible for stronger impurity. [Fig. 4.1(b)] For a repulsive scatterer, only plateau smoothing was perceptible. The conductance is lower than multiples of $2e^2/h$ of perfect transmission (dashed lines). Similar results were also reported by Bardarson *et al.* in a more recent report for a spatially extending Gaussian-type impurity.[100] Tekman *et al.* reported more thorough numerical calculations of conductance of QW with different geometries. The influences of surface roughness, quasibound states, and impurities on transport were also investigated by the authors.[98]

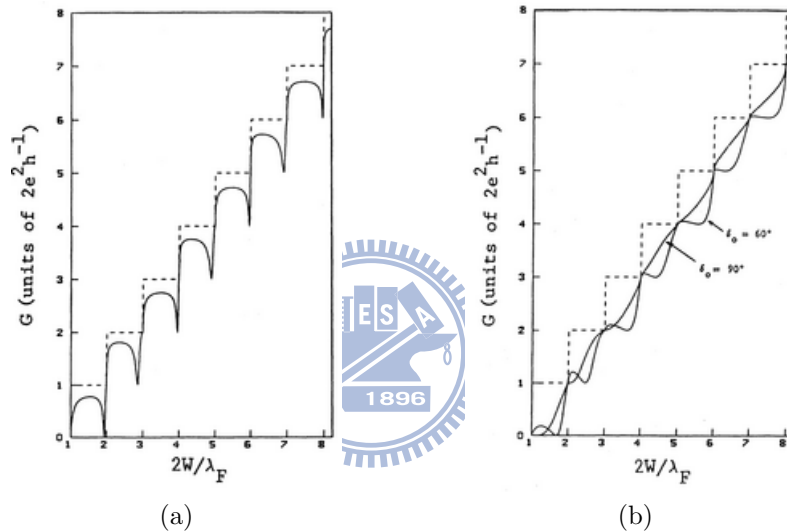


Figure 4.1: Conductance G for an electron waveguide plotted as a function of the width W of the channel for an attractive impurity. (a) Phase shift $\delta_0 = 30^\circ$. (b) $\delta_0 = 60$ and 90° . (After Chu *et al.*, Ref. [19].)

When electrons are scattered by a defect in a quantum channel, there is probability that the incident wave is scattered to higher modes which can be evanescent. Bagwell proposed that the electrons scattered to the evanescent modes are effectively localized since the wavefunction decays spatially rather than propagates. Therefore quasibound states develop accordingly due to the presence of impurity.[20] Linear conductance exhibits peaks and dips reflecting the transmission resonances in the presence of an impurity. Similar propositions about the quasibound states were also made by Gurvitz *et al.*[96] and Levinson *et al.*[99] from alternative calculation approaches and for more general cases of impurities. Tekman *et al.* demonstrated that the conductance reveals resonant tunneling

peaks when there were quasibound states as shown in Fig. 4.2.[98]

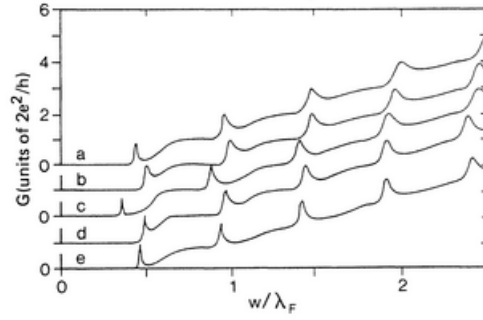


Figure 4.2: Resonant tunneling effects on the conductance of a QPC due to the widening, the potential well, or attractive impurity at the center of the constriction. (After Tekman *et al.*, Ref. [98].)

Vargiamidis *et al.* considered a Gaussian-type impurity in an infinitely long QW. The impurity was modeled as $V_i(x, y) = \frac{\hbar^2 \gamma}{2m^*} \delta(y - y_i) e^{-x^2/d^2}$. y is along the transverse direction, while x is along the longitudinal direction.[101] As shown in Fig. 4.3(a), the authors demonstrated that the conductance step shifts to more lower energy as the impurity is displaced away from the center of the QW (from $y_i/w = 1/12$ to $5/12$). The results indicated that the subband bottom is altered with respect to the position displacement of impurities. The subband shifting with respect to impurity configurations and positions was also reported in Ref. [105] by Takagaki *et al.*, Ref. [93] by Marel *et al.*, and Ref. [98] by Tekman *et al.*. In Ref. [105], the quantum channel was divided into $N_x \times N_y = 32 \times 32$ two dimensional grids. Incorporating arbitrarily long range impurities $V_{imp}(\mathbf{r}) = U_i \exp(-|\mathbf{r} - \mathbf{r}_0|/r_d)$ where U_i was randomly distributed between $(-\Gamma/2, \Gamma/2)$ across the lattice sites, the mode matching method and transfer matrix methods gave the conductance of the QPC. As shown in Fig. 4.3(b), the quantization step shifts and the line shape varies for different impurity configurations.

Hitherto, the discussions of impurity are without a priori knowledge of its physical origins. It was sensible that scientists attempt to investigate the influence of physical defects on transport. One of the most intuitive and unavoidable sources of scatterers is the ionized donors in the doping layer separated from 2DEG by a barrier. Adopting Thomas-Fermi approximation and considering randomly distributed donors on the δ -doping layer, Nixon *et al.* numerically calculated the averaged potential in 2DEG.[21, 22]

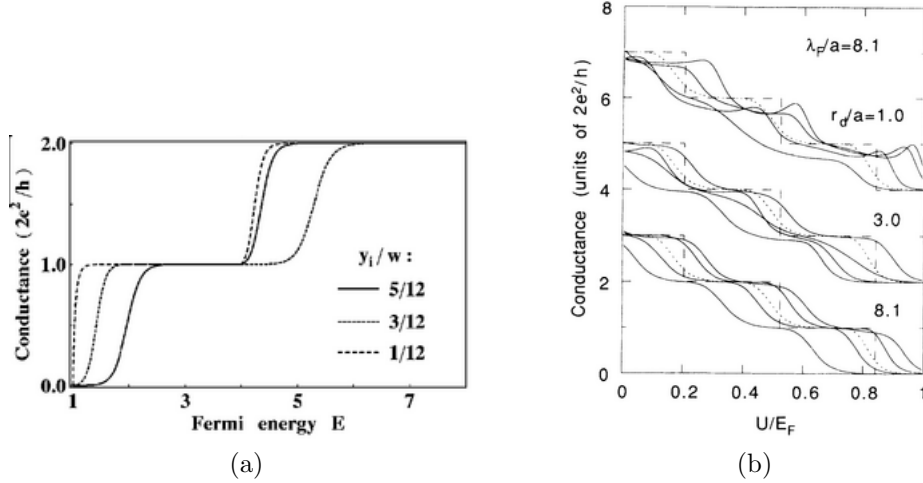


Figure 4.3: (a) G vs. E_F through a Gaussian impurity of strength $\gamma = 2.5 \times 10^6 \text{cm}^{-1}$ and $d=0.7w$ in a QW of width w , for three different impurity positions (y_i/w). (After Vargiamidis *et al.*, Ref. [101].) (b) The conductance of a QPC in the presence of long-range disorder. The dotted line represents the conductance for a perfect sample, while different impurity configurations are assumed for the solid lines. The spatial extension and number of scatterers are characterized by r_d/a (After Takagaki *et al.*, Ref. [102].)

The potential is not uniform, and contains fluctuations as shown in Fig. 4.4(a). When the length of the channel was longer than the correlation lengths of fluctuations, the conductance quantization was predicted to break down. Similar arguments were made by Takagaki *et al.* in Ref.[102]. It is possible that a potential minimum exists inside the QPC due to the potential fluctuations [Fig. 4.4(a)], and conductance resonance stands a chance. As shown in the two lower traces of $G(V_g)$ in Fig. 4.4(b), conductance peaks and dips are visible due to the existence of local potential well. The authors also suggested that the ionized donors redistribute after a thermal cycling and a different potential map would be produced.

The effects of boundary roughness on the transport have also been studied for quite some time.[94, 95, 106, 107] Recently, Csontos *et al.* modeled the roughness by dividing a QW into a large amount of segments, and applying randomly distributing weak variation of width along the transport direction.[107] The average width variation was 8 nm. With increasing QW length, the step conductance was lowered, conductance dips appeared at the subband energy, and fine conductance oscillations were visible.[Fig. 4.5] The authors suggested that the conductance dips result from the intraband scattering at the subband

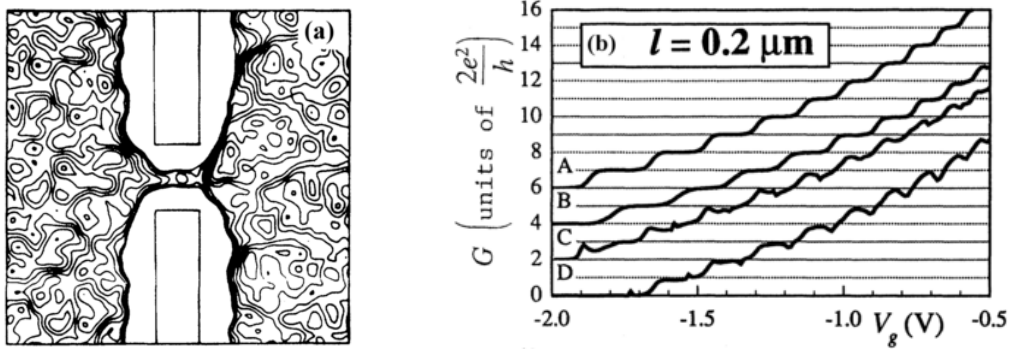


Figure 4.4: (a) Gate pattern on surface and density of electrons in 2DEG for a point contact with gap of $0.3 \mu\text{m}$ and length of $0.2 \mu\text{m}$. Contours start from zero and are $4.2 \times 10^{14} \text{ m}^{-2}$ apart, corresponding to an energy spacing of 1.5 meV. (b) Conductance G as a function of gate voltage V_g for a $0.2 \mu\text{m}$ QPC. A is in the absence of potential fluctuations. The other curves are for different impurity configurations. (After Nixon *et al.*, Ref. [22].)

thresholds.

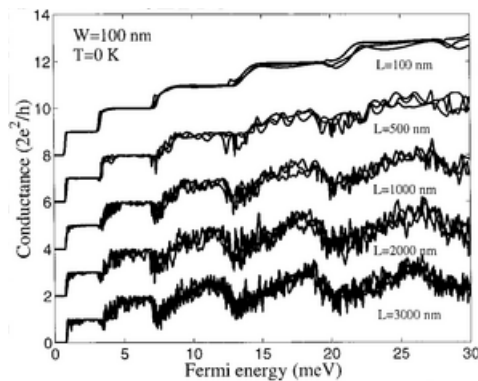


Figure 4.5: Conductance calculated at $T = 0 \text{ K}$ for 100 nm wide quantum wires of various lengths. For each length, three curves correspond to three different roughness distributions. (After Csontos *et al.*, Ref. [107].)

4.3 Disordered quantum wires and position controlling

Lateral shifting technique by independently biasing the split gates was adopted to systematically control the position of QWs as well as the impurity arrangement. Controlling the position of QWs was supported by the theoretical calculations.[108, 109] As shown in Fig. 4.6, the asymmetric electric field shifts the potential minimum to the other side from the $y=0$ axis. (illustrated by the thick gray line) Shifting the position of the QWs

effectively imposes various impurity configurations, since the impurities are expected to distribute randomly. The split gates are offset by a voltage bias, ΔV_g . Without being mentioned throughout the chapter, $V_g + \frac{1}{2}\Delta V_g$ was applied on one gate, and $V_g - \frac{1}{2}\Delta V_g$ was applied on the other. The position offset is linearly dependent with ΔV_g . [108, 109] This technique has been widely used in experimental studies of random telegraph noises in QWs. [110, 111, 112] The noises were associated with the deep center defects and as the QWs were shifted the characteristics of these noises changed.

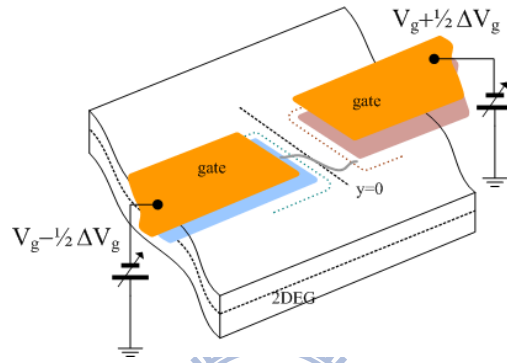


Figure 4.6: Schematic illustrations of the setup for lateral position shifting.

Measurements were performed in the pumped ^3He cryostat with a base temperature of 0.27 K. Although the mean free path ℓ_e of the bulk 2DEG were much longer than the QW channel length, samples with long split gate length of several micrometers being closely fabricated in parallel were found to be disordered, for example the two pairs of split gates separated by $\sim 0.4 \mu\text{m}$ shown in the inset of Fig. 4.7(a). The disorderliness reduces with increasing separation distance. The impurities were suspected to arise from the damage in the 2DEG due to the locally concentrated backscattered electrons of high energies during the pattern transferring in e-beam lithography. The lithographic width of the samples is about $0.45 \mu\text{m}$ while the length covers quasi-zero, 0.2, and $0.5 \mu\text{m}$. Unlike the devices affected by deep center defects in other reports, the results here show no random telegraph noises. For comparisons, results of a $0.3 \mu\text{m}$ QW, intentionally disordered by imposing a small local widening, and a low-disordered quasi zero length QW were studied as well. The presented results are the typical features based on measurements of ten disordered and three clean QWs.

4.4 Results and discussion

Figs. 4.7(a) and 4.7(b) show the linear conductance of two unintentionally disordered QWs. Traces of $G(V_g)$ are plotted against the lateral shifting voltage ΔV_g and are offset in turn in 50 mV steps. The plateau conductance is much lower than the expected integer multiples of G_0 in both devices indicating that electrons are partially backscattered. As a consequence, more steps are present in a smaller conductance range. For instance, more than eight steps are visible in the range of $0 < G < 5G_0$ on the $\Delta V_g = 0$ trace for sample A in Fig. 4.7(a). The higher subband conductance shows slight distortions. Sample B is much more disordered with lower quantization conductance, more distortions, and more missing steps. One thing worth being noticed is that the traces are expected to be evenly spaced if the subband energies remained unchanged with respect to the position of the impurities, i.e. the pinch-off voltage should be unchanged. However, in both figures, traces are closer to each other at the positive ΔV_g side but looser at the other. In a clean QW (discussed in the latter paragraphs), the conductance traces are more evenly spaced. This indicates that the threshold energies of subbands vary with the position of impurities, or effectively with the impurity configurations. In addition, a couple of conductance resonances are observable for $G < G_0$ for sample B in Fig. 4.7(b). The results are in congruence with the prediction that the quasi-bound states in a QW given rise by the impurities lead to conductance resonance and alter the subband threshold voltage.[19, 98, 99, 96, 100, 101]

The source-drain bias spectroscopy was investigated by sweeping a dc source-drain voltage V_{sd} across a confined QW and measuring the dynamic conductance $G = dI/dV_{sd}$. Fig. 4.7(c) shows the spectroscopy, $G(V_{sd})$ against a series of V_g , of sample A at $\Delta V_g = -0.6$ V. It demonstrates a series of single peak centered at $V_{sd} = 0$ for $G < G_0$, which resembles the ZBA of QWs. However, this structure is not the same as the ZBA of QWs since the single peak evolves into double splitting peaks by shifting the QW to the other side at $\Delta V_g = +0.6$ V as shown in Fig. 4.7(d). On the contrary, splitting of the ZBA was not observed in a clean QW against various ΔV_g as shown in Figs. 4.10(b)-4.10(c). The energy difference of the splitting in Fig. 4.7(d), ϵ_d , is not a constant. ϵ_d decreases with decreasing V_g for $0.72G_0 < G < G_0$, and begins to increase for $G \lesssim 0.72G_0$. The peak

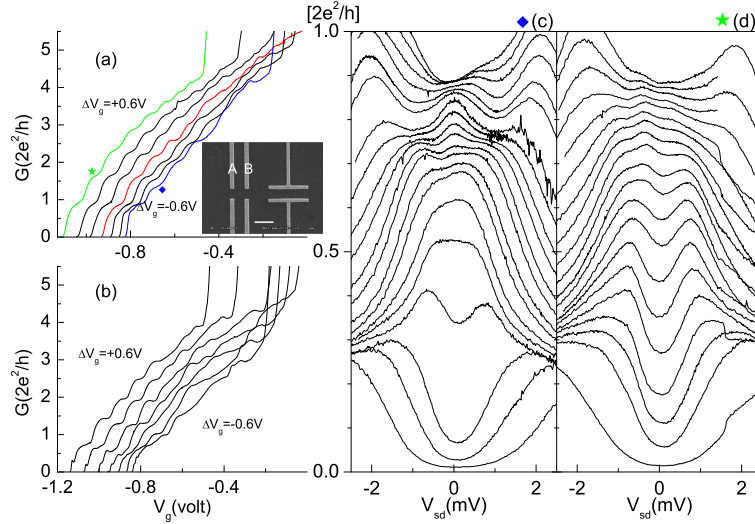


Figure 4.7: $G(V_g)$ and source-drain bias spectroscopies for two unintentionally disordered QWs at 0.3 K. (a) Sample A. $G(V_g)$ versus the differential gate voltage. $\Delta V_g = +0.6$ V (leftmost, labeled by a star) ~ -0.6 V (rightmost, labeled by a diamond) in 0.2 V steps. The traces are offset in turn by 0.05 V. Inset: Micrograph of the disordered QWs A and B. The white scale bar equals a length of 1 μm . (b) Sample B. $G(V_g)$ versus ΔV_g for the same conditions, and traces are offset by the same manner. (c) Source-drain bias spectroscopy of sample A for $\Delta V_g = -0.6$ V. $V_g = -900 \sim -969$ mV in 3 mV steps. (d) Source-drain bias spectroscopy of sample A for $\Delta V_g = +0.6$ V. $V_g = -900 \sim -960$ mV in 3 mV steps.

splitting was generally observable in the disordered QWs, and is believed not to be an inherent feature of QWs, such as the ZBA.

In the presence of impurities, electrons have the probability to be scattered into non-propagating evanescent modes. The mechanism effectively creates localized electrons close to the impurities. Quasibound states would be developed and conductance resonances are expected. [20, 96] Fig. 4.8 presents results of a disordered QW that has strong tunneling resonances. Here, a different voltage biasing approach was adopted. V_g was applied on the upper gate and $V_g + \Delta \tilde{V}_g$ was applied on the lower one. Weak conductance oscillations are discernible along the conductance trace of $\Delta \tilde{V}_g = 0$ in Fig. 4.8(a), besides the five quantized plateaus. A strong resonant peak emerges by shifting the QW to $\Delta \tilde{V}_g \leq -0.1$ V, while the peak conductance tends to pin at $0.5G_0$. The superimposing resonances are stronger for the negative $\Delta \tilde{V}_g$. The effect of resonances on the source-drain bias spectroscopy is presented in Figs. 4.8(c)-4.8(e) for $\Delta \tilde{V}_g = +0.3, 0$, and -0.3 V. Surprisingly, The ZBA of QWs is seen in all three spectroscopies for $G < G_0$, coexisting with the splitting peaks due

to the resonant states. The concurrence of the ZBA and resonant peaks forms a triple-peak structure which was also noticed by Sfigakis *et al.*[52] E.g. two strong satellite peaks appear at the sides of the ZBA at $V_{sd} \sim \pm 0.8$ mV on the dot-labeled curve of $V_g = -383$ mV in Fig. 4.8(d). The amplitude and width of the ZBA are affected by the resonant peaks. The satellite peaks appear at larger $|V_{sd}|$, e.g. at ~ 1.9 mV in Fig. 4.8(c) of $\Delta\tilde{V}_g = +0.3$ V, and at ~ 1.8 mV in Fig. 4.8(e) of $\Delta\tilde{V}_g = -0.3$ V. Comparing Fig. 4.8(d) with Figs. 4.8(c) and 4.8(e), the ZBA is weaker and suppressed more rapidly with decreasing V_g at $\Delta\tilde{V}_g = 0$ in Fig. 4.8(d). The result indicates that the existence of the resonant peaks due to the resonant states nearby the $V_{sd} = 0$ suppresses the ZBA. The evolution of the split peaks with respect to V_g , e.g. as the dashed lines in Fig. 4.8(d), resembles the diamond structure of the tunneling spectroscopy of zero-dimensional states. Similar evolution of the satellite peaks is also observable in Fig. 4.8(e) for either $G < G_0$, or $G_0 < G < 1.75G_0$ for the higher subband.

Interestingly, the triple-peak structure appears also at the higher conductance regime for $1.55G_0 < G < 1.75G_0$ at $\Delta\tilde{V}_g = -0.3$ V. The central peak is weaker compared with the strong *single* peak observed in the same range in the clean QW in Fig. 4.9(d). The appearance of the central peak at such high conductance regime implies that the ZBA is not unique for low conductance regime on which most groups focused. Notice that groups of crossed traces appearing in all three graphs indicates strong conductance resonances in finite V_{sd} regime. Consider a QW in the presence of resonant states induced by impurities as shown in Fig. 4.8(b). Aligning of a resonant level with the chemical potential of the source or drain increases the tunneling probability, as well as the differential conductance $G = \frac{dI}{dV_{sd}}$. Finite V_{sd} would be required to align the chemical potential with a resonant state when the QW is not initially in resonance, resulting in the evolutions of splitting peaks with respect to V_g in the spectroscopies and conductance resonances at finite V_{sd} . Although this is an oversimplified scenario, it provides a qualitatively appropriate explanation to our results.

Linear conductance, $G(V_g)$, of a quasi-zero in length QW in two separate cooling processes are shown in Figs. 4.9(a)-4.9(b). Both traces reveal non-oscillating conductance

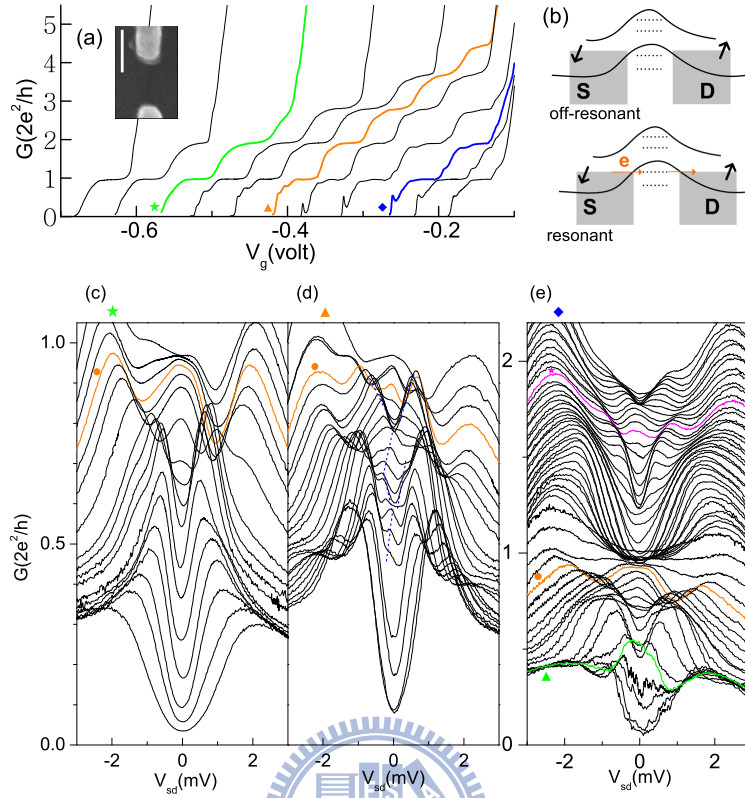


Figure 4.8: (a) $G(V_g)$ against $\Delta\tilde{V}_g$ of a disordered QW in the presence of strong conductance oscillations at 0.3 K. $\Delta\tilde{V}_g = +0.5$ (leftmost) ~ -0.5 V (rightmost) in 0.1 V steps. Inset: Micrograph of the device. The scale bar has a length of $0.4 \mu\text{m}$. (b) Scenario for the observed split peaks due to the presence of resonant levels in a QW. The thick lines stand for the last two subbands of a QW; the dotted lines stand for the resonant levels induced by impurities. (c)-(e): source-drain bias spectroscopies for various $\Delta\tilde{V}_g$. (c) $+0.3$ V, (d) 0 V, and (e) -0.3 V. Dashed lines are visual guides for the evolution of conductance peaks as functions of V_g and V_{sd} .

and clear quantization steps without distortions, indicating that the sample is low disordered. The plateaus can be aligned exactly to the integer multiples of G_0 by subtracting a serial resistance of about 300Ω from the data, such as in [67] by Thomas *et al.* We present the raw data here since the series resistance does not affect our results. Fig. 4.9(c) shows the spectroscopy in the first cooling operation. The dynamic conductance exhibits clearly a series of single peak centered at $V_{sd}=0$ for $G < G_0$ referring to as ZBA. The ZBA is reproducible after thermal cycling, as shown in Fig. 4.9(d) for the second cooling process. The half plateaus and the 0.7 anomaly at finite biases are visible as bunches of curves (opposed to crossing traces due to resonant states) at $G \sim 1.5G_0$ and $G \sim 0.8G_0$, for

$V_{sd} > 1.4$ mV and $V_{sd} > 0.7$ mV, respectively.

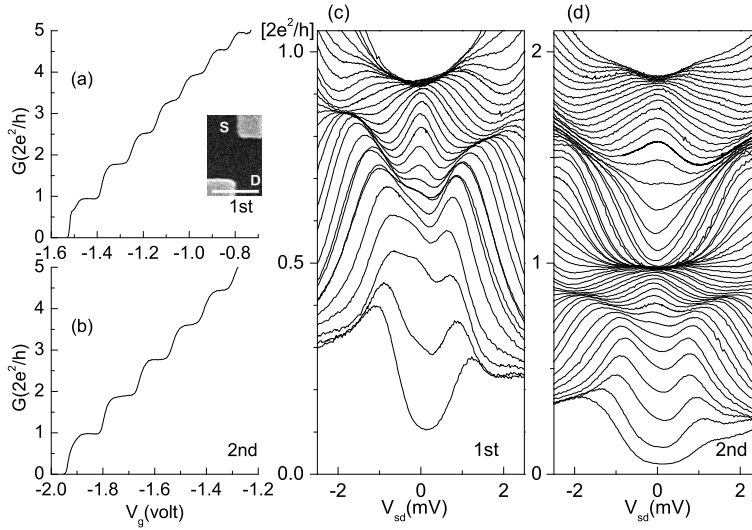


Figure 4.9: Zero-bias differential conductance G vs. split gate voltage $G(V_g)$, (a)-(b), and source-drain bias spectroscopies, (c)-(d), in two separate cooldowns at 0.3 K of a *clean* quantum wire. Traces of $G(V_{sd})$ in (c) and (d) are for discrete consequential split gate voltages in 4 mV steps. (c) $V_g = -1.450 \sim -1.558$ V. (Top to bottom) (d) $V_g = -1.720 \sim -1.944$ V. Inset in (a): Micrograph of the device. The white scale bar indicates a length of 0.5 μm .

Since 2DEG is generally not free from disorder [113], lateral shifting was applied to further scrutinize the quality of the sample. Fig. 4.10(a) shows conductance traces against a series of ΔV_g . Similarly, the traces are offset in turn by 50 mV step. For $\Delta V_g = 0$, the trace demonstrates more than fourteen clear quantization steps. The traces are much uniformly spaced compared with Figs. 4.7(a) and 4.7(b). It implies that the pinch-off voltages are the same for different ΔV_g . A slight conductance oscillation appears around the sixth and seventh steps for $\Delta V_g = +0.2$ and $+0.4$ V. Except this small disturbance, the conductance quantization remains unaltered with respect to the lateral shifting, confirming that the device is quite clean. Figs. 4.10(b)-4.10(c) show the spectroscopies of the QW at two opposite positions, $\Delta V_g = +0.6$ and -0.6 V. Both figures demonstrate ZBA for $G < G_0$. The ZBA is slightly weaker in Fig. 4.10(b), however, there is no additional structure, such as satellite peaks, compared with the disordered QWs. The varying ZBA characteristics are understandable. It is known that the characteristics of the ZBA are sensitive to electron scattering, which is affected by the local electric field, density, or physical

geometry of a device.[114] For a pair of ideally symmetric split gates, one would expect the ZBA to be identical for these two ΔV_g . However, we believe that the deviation is due to the asymmetry of the realistic gate edge, which is beyond the experimental resolution. The random potential fluctuation due to ionized donors is another possibility that causes asymmetric local field.[22] Nevertheless, the result shows that the ZBA is a rather robust feature of low-disordered QWs.

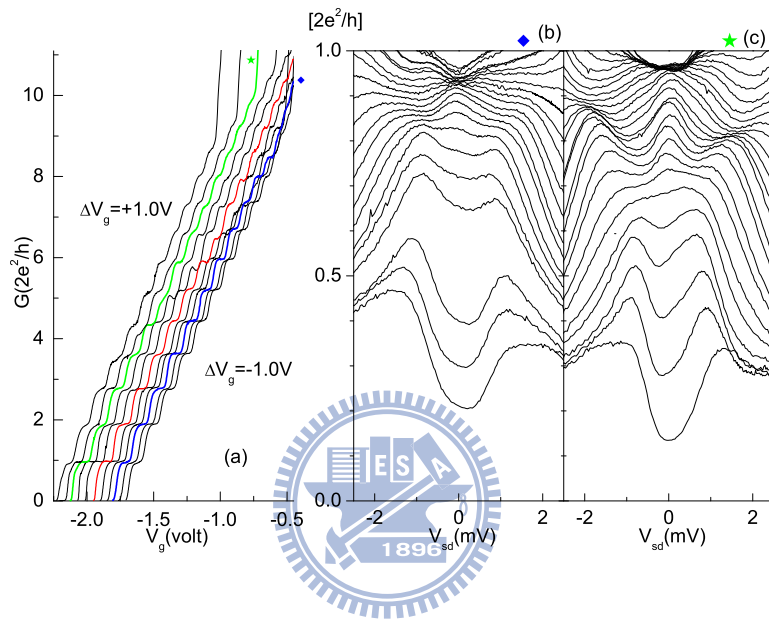


Figure 4.10: $G(V_g)$ of the clean quantum wire against differential gate voltage ΔV_g . From left to right, $\Delta V_g = +1.0 \sim -1.0$ V in 0.2 V steps. The traces are offset in turn by 0.05 V for clarity. (b)-(c): source-drain bias spectroscopies for $\Delta V_g = -0.6$ and $+0.6$ V respectively. (b) $V_g = -1.846 \sim -1.934$ V in 4 mV steps. (c) $V_g = -1.848 \sim -1.964$ V in 4 mV steps.

To further confirm the influence of impurities on the transport in QWs, a ‘standalone’ (opposed to the closely packed samples) pair of $0.3 \mu\text{m}$ split gates intentionally imposed with disorder is also studied. As shown in the inset of Fig. 4.11(a), the QW contains a small local widening. The electric potential generated by the applied gate voltage is expected to be lower in the widened area. Electrons traveling across the QW would be backscattered due to mode mismatch resulting in effectively an attractive impurity in a QW. We estimate the additional depletion region besides the lithographic area to be $75 \sim 100$ nm from other experiments. The device is not expected to be developing a quantum dot, since the dent is also about 100 nm in length. The argument is confirmed by the absence of charging effect for $G < G_0$. In Figs. 4.11(a) and 4.11(b) of two

cooling processes, only the first quantized plateau sustains in the linear conductance. For $G > G_0$, conductance plateaus were distorted and missing. The fine structures of linear conductance are different between thermal cyclings. The traces in Fig. 4.11(b) have several resonances which are weak in Fig. 4.11(a).

The spectroscopy appears to be altering between the thermal cycling and presenting features of disordered QWs. In Fig. 4.11(c), double splitting-peaks are observable for $G < G_0$ and the energy difference of splitting decreases with decreasing V_g . The ZBA is not observable. On the contrary, the single peak structure is visible for $0.84G_0 < G < G_0$ in Fig. 4.11(d) for the second cooling operation. The conductance shoulder visible at $\sim 0.74G_0$ at zero-bias rises with increasing V_{sd} , and becomes visible as a resonant peak for $V_{sd} \gtrsim 0.88$ mV (crossings of traces). The deviations between two cooldowns are comprehensible by the fact that the ionized donors redistribute between thermal cycles, resulting in the different averaged potential fluctuations [22] which alter the impurity arrangement, and correspondingly the interference between the backscattered electrons.

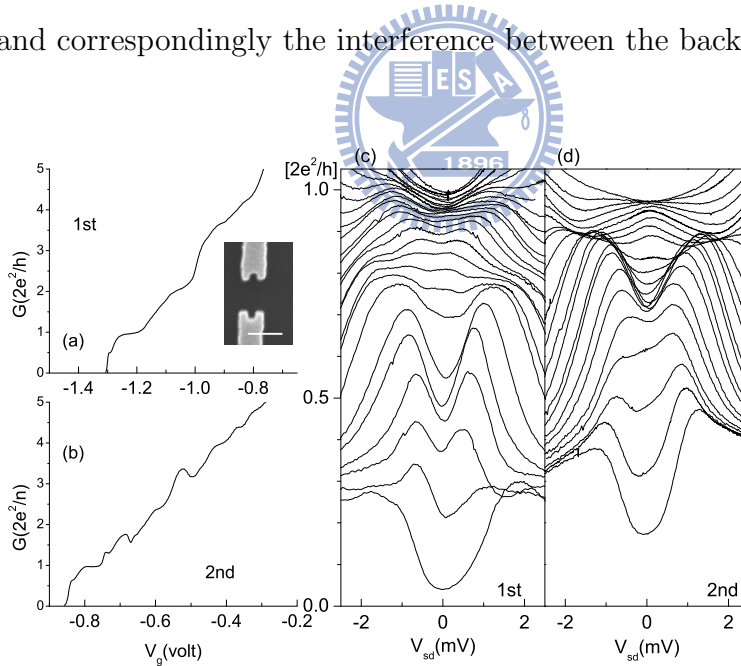


Figure 4.11: $G(V_g)$, (a)-(b), and source drain bias spectroscopy, (c)-(d), in two separate cooldowns of a QW with a small local widening at 0.3 K. Inset in (a): micrograph of the device with the white scale bar indicating a length of $0.5 \mu\text{m}$. (c) $V_g = -1.140 \sim -1.248$ V in 4 mV steps. (d) $V_g = -0.780 \sim -0.845$ V in 3 mV steps.

The ZBA is a peculiar phenomenon of QWs. One dimensional Kondo model, which was based on the assumption of a spin dependent localized potential resulting in a spontaneous

magnetic impurity, was proposed to explain the experimental findings.[37, 48, 49, 50, 51] According to the 1D Kondo model, ZBA was expected to split in parallel magnetic fields while the splitting width was about the Zeeman energy. More recently, however, several groups reported more intricate features of the ZBA.[52, 53, 54] In some devices, splitting occurs in magnetic fields, but two split peaks can resolve back into a single peak by laterally shifting the QW. In some other devices, splitting even occurs in zero magnetic fields.[53, 54] Chen *et al.* claimed that disorder is related with the splitting of the ZBA in magnetic fields.[53] Sarkozy *et al.* suggested that resonant backscatterings and length resonances could result in split ZBA.[54, 115] As we demonstrated here, impurities presenting in QWs indeed lead to these complicated features.

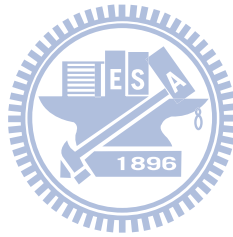
4.5 Conclusions

In conclusion, ZBA is robust in clean QWs against lateral shifting and thermal cycling. On the other hand, impurities can cause resonances leading to complicated source-drain spectroscopies. These resonant features are sensitive to thermal cycling and lateral shifting of QWs revealing the random nature of impurities in ballistic QWs. The double split peaks due to resonant levels affect the characteristics of ZBA. The results indicate that cleanness is crucial for studying the intrinsic behaviors of ZBA in quasi-one dimensional systems.

Chapter 5

Time dependent electric fields generated DC currents in a large gate-defined open dot

5.1 Introduction



In my PH.D research, efforts were also devoted to realizing quantum charge pump in an quantum dot (QD). Although whether genuine quantum charge pumping was realized is still controversial, interesting result is found in our investigation. A charge pump in general generates a dc current by driving a system with two out of phase ac electric fields by analogy with a water pump.[116] The *classical* charge pump in a closed QD has been realized for quite a long time.[117] In a closed QD where the potential barriers between the leads and the dot are oscillating out of phase in the same frequency, electrons can transport discretely. A finite external bias is required to develop potential difference between the source and drain so as to provide current. Classical charge pump was also realized in a one dimensional semiconductor wire recently, while a traveling wave-like potential was generated to drive the electrons without bias.[118] Besides the classical charge pump, pumping charge *quantum mechanically* was of particular interests since the current is expected to be dissipationless, i.e. the power consumption would be

infinitesimal.[119] The experimental report of adiabatic quantum pump in an open QD has intrigued huge amount of theoretical works.[120] The wavefunction of an open QD configured in e^2/h corresponding to one transmission mode in the source and drain leads for each were periodically deformed. However, it turned out that the results were confused with another classical mechanism, *rectification*, which is basically a spurious electrical circuitry effect.[121] Dicarolo *et al.* claimed that at high enough frequencies photovoltaic effect which is also a quantum mechanical effect dominates. On the other hand, at low frequencies it is rectification that told the story.[122, 123] Rectification current is induced from the coupling between time-varying conductance and chemical potentials of reservoirs of a QD. To the best of our knowledge, experiments are still scarce and quantum charge pump has not yet been truly accomplished for the time this dissertation is prepared.

Technically speaking, charge pump in mesoscopic devices converts time-dependent signals to dc. For two dimensional systems, Höhberger *et al.* and Müller *et al.* used interdigitated ratchets fabricated on top of a large 2DEG to produce dc currents.[124, 125] These techniques may be useful, since such transformations may serve the operations of power rectification and signal processing in integrated circuits[126] or signal modulation in telecommunications[127]. Therefore, it is important to understand comprehensively those interfering effects before further practical and industrial applications in nanoscale semiconductor devices.

In this chapter, we present the performance of generated dc current I_{dc} by two fast oscillating electric fields in an open dot for two different electrical configurations. In the first setup, the ac voltages are applied on two side gates, resembling the typical charge pump; in the other, one ac voltage is relocated to the source lead, alike the condition of rectification. Both setups demonstrate a sinusoidal dependence of I_{dc} on the phase difference between the two ac voltages, $\Delta\phi$. Additionally, I_{dc} is proportional to the product of the voltage amplitudes. However, the dependences on frequency, coupling strength, and magnetic field in the two setups show opposite features. The results indicate that the currents are generated by different mechanisms, but not any circuitry effects for the pumping-type current.

5.2 Electrical configurations

The 2DEG is the same as in other chapters. Electron beam lithography was used to pattern the surface of GaAs/Al_xGa_{1-x}As heterostructure with numerous geometrical arrangements. As shown in the inset of Fig. 5.1(a), there are four corner gates to confine an area with two quantum point contacts (QPCs) serving as the entrance and exit to reservoirs. The gap width of the QPCs are $\sim 0.4 \mu\text{m}$. The other two gaps where the side gates, s1 and s2, are lying between have a width of $\sim 0.35 \mu\text{m}$. This design ensures that when both QPCs are confined, constrictions are also developed at the two side gaps. When the voltage excitations are applied to the side gates, the induced potentials superimpose on the confinement created by other four gates, being able to disturb the electrons inside the confined dot. The lithographic area of the dot is about $1 \mu\text{m}^2$ resulting in an average level spacing $\Delta = 2\pi\hbar^2/m^*A \sim 7.2 \mu\text{eV}$. Experiments were carried out in a pumped ³He refrigerator with a base temperature of 0.28 K. Data presented here were taken at 0.3 K.

In setup 1 which resembles the typical charge pump[116, 119], two fast oscillating voltages with an equal frequency ($f \sim 0.1-10$ MHz) were applied to the two side gates. $V_{s1}(t) = V_{s1,ac} \sin(\omega t + \Delta\phi)$ and $V_{s2}(t) = V_{s2,ac} \sin(\omega t)$. As shown in Fig. 5.1(a), the signals were fed through coaxial cables in the fridge with the nominal attenuation of 12.7 dB/m at 0.5 GHz. (18.7 dB/m @ 1GHz.) By separate measurements, the attenuation in our system for the applied frequencies were calibrated. Loss is ~ 6.8 dB at 10 MHz from the signal generators to the sample. To allow a sensitive lock-in measurement, the signals from the signal generators are chopped by a low frequency square wave at 101 Hz. The dc current I_p was amplified by a current preamplifier before being input into the lock-in amplifier. The measurement methods in the setup 2 are the same as in setup 1, except one oscillating voltage was applied to the source lead as shown in Fig. 5.1(b). The conductance of the dot is expected to oscillate as a function of time corresponding to the oscillating side gate voltage, as well as the source chemical potential. The setup resembles the rectification effect.[121] The generated current I_r is expected to flow to the ground passing through the current preamplifier. These two signal generators were synchronized in order to sweep the phase difference $\Delta\phi$ between them.

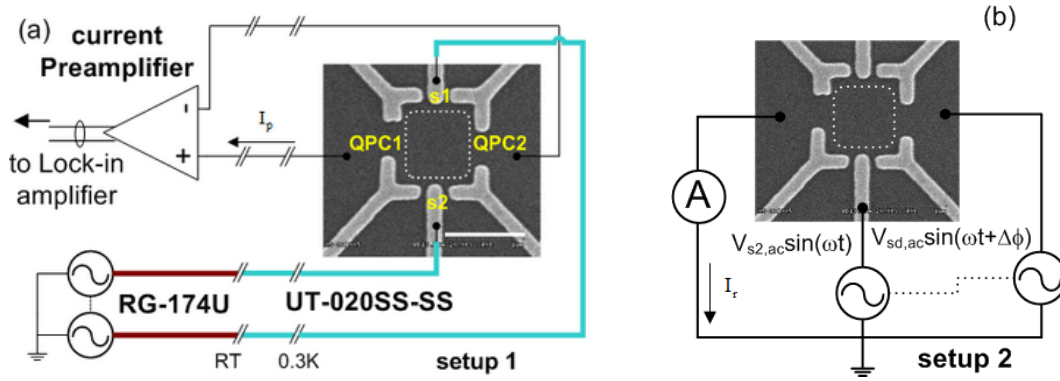


Figure 5.1: (a) SEM image of the device and a detailed drawing for the electrical setup 1. The white bar indicates 1 μm . (b) Simplified sketch of setup 2.

In the inset of Fig. 5.2, the resistance of the quantum point contacts shows clear steps as a function of gate voltage $V_{qpc1(2)}$. The resistance is quantized at $\frac{1}{i} \left(\frac{h}{2e^2} \right) = \frac{12.9}{i} k\Omega$, where $i=1, 2, \dots$, indicating well defined transmission mode in the QPCs. Fig. 5.2 shows the resistance when both QPCs are confined and the large dot is developed. The electron number is estimated to be ~ 2000 in the dot. To systematically characterize the mode number N of the confined open dot, V_{qpc1} was first fixed at a certain plateau and then V_{qpc2} was swept. As an example, V_{qpc1} is fixed on the 4.3 kΩ plateau, corresponding to a mode number of three in QPC1. (The lowest trace in the figure.) The dot resistance, R_{dot} , increases with the decreasing V_{qpc2} revealing several steps along the trace. The mode number of QPC2 in the dot is determined by counting the steps from the pinch-off. For the step labeled '1', the resistance is about 16.7 kΩ when the dot has a mode number $N = (N_{qpc1}, N_{qpc2}) = (3, 1)$. In the trace of $R_{qpc1}=12.7 k\Omega$ (or $N_{qpc1}=1$), the resistance plateaus are more smooth but still discernible. The steps have a resistance larger than the addition of the separate QPCs' resistances. Step '1' is about 30 kΩ for $N=(1, 1)$; step '2' is about 21 kΩ for $N=(1, 2)$.

5.3 Pumped charge and rectification

Scattered points in Fig. 5.3(a) are the typical result of the measured dc current as a function of the phase difference. I_{dc} as a function of $\Delta\phi$ has the sinusoidal form with a small offset in the period of 2π . To systematically characterize the current amplitude, the

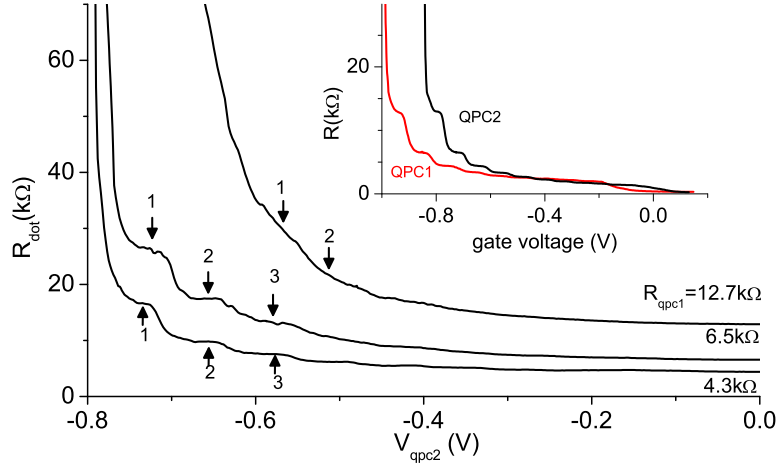


Figure 5.2: Dot resistance as a function of gate voltage V_{qpc2} when QPC1 is confined at 4.3, 6.5, and 12.7 k Ω . The mode number of QPC1, N_{qpc1} , is 3, 2, and 1 respectively. The mode number of QPC2 was counted and labeled on the trace by the numbers. Inset: Resistance of the independent quantum point contacts vs. gate voltage. The red(black) trace is for QPC1(2).

data is numerically fit with the form $I_{dc}(\Delta\phi) = I_{p(r)} \sin(\Delta\phi + \phi_0) + I_{p(r)}^0$. The solid line in the panel is the fit to the dataset by least square regression. The current generated in setup 1, I_p , as a function of voltage amplitude for $N=(2,2)$ and $f=7$ MHz is presented in Fig. 5.3(b). Equal voltage amplitude is applied on the side gates, i.e. $V_{s1,ac} = V_{s2,ac} = V_{ac}$. In this log-log plot, the data points follow a straight line of slope of 2 indicating a bilinear dependence, $I_p \propto (V_{ac})^2$. I_p increases from as low as tens of pA for $V_{ac}=1$ mV to tens of nA for $V_{ac}=40$ mV. For $V_{ac} > 40$ mV, nonlinear effect becomes significant and $I_{dc}(\Delta\phi)$ does not follow the sinusoidal form. The inset of Fig. 5.3(b) shows $I_r(V_{sd,ac}, V_{s2,ac} = 15mV)$ in setup 2 for $N=(2,2)$, $f=5$ MHz. The slope of the trace is ~ 1.05 , also suggesting a bilinear dependence of the current on the voltage amplitude.

Although the phase difference and amplitude dependences of I_p and I_r are similar, the relations with frequency, coupling strength and magnetic fields diversify. In Fig. 5.4(a), the five datasets represent I_p as a function of frequency for various coupling strengths between the dot and the reservoirs. From top down, the mode number of QPC1 and QPC2 are (1, 1), (1, 2), (1, 3), and so on. I_p is about linearly dependent with frequency for $f \lesssim 8$ MHz. The current begins to saturate for higher frequencies. The dc current is the largest for $N = (1, 1)$ and decreases by increasing the mode number. There is one thing worth

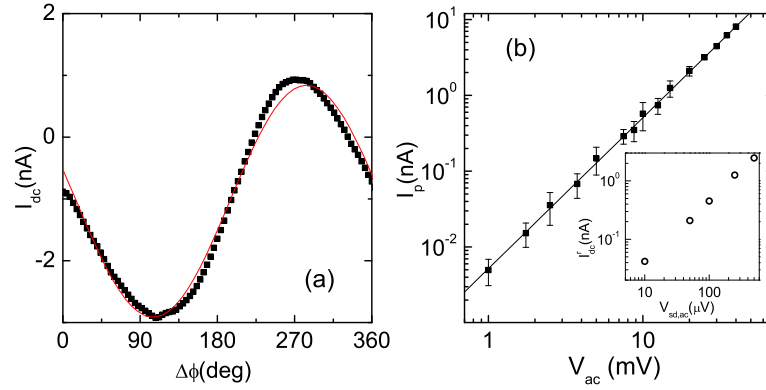


Figure 5.3: (a) Typical plot of the measured $I_{dc}(\Delta\phi)$ (squares) along with the fit of the form $I_{dc}(\Delta\phi) = I_{p(r)} \sin(\Delta\phi + \phi_0) + I_{p(r)}^0$ (solid curve). (b) Logarithmic plot of $I_p(V_{ac})$ with a power law fit. The least square root fit gives a power of 1.99 ± 0.06 . In this device, the channel number of both entrance and exit of the dot is controlled to be 2 and the frequency of the ac voltage is 7 MHz. Inset: logarithmic plot of $I_r(V_{sd,ac})$ for $N=(2, 2)$, $f=5$ MHz and $V_{s2,ac}=15$ mV for setup 2.

mentioning: I_p drops rapidly as soon as the dot is closed when R_{dot} is slightly larger than h/e^2 while $N = (0, 0)$. Although the measured R_{dot} is still finite ~ 100 k Ω , the measured current reduces to almost beyond the experimental resolution. Interestingly, I_p is found to follow a specific relation with the total mode number of the dot $N_{tot} = N_{qpc1} + N_{qpc2}$. The ratio of N_{tot} for the last four datasets to $N = (1, 1)$ is 3/2, 2, 2, and 3 respectively. Fig. 5.4(b) shows the rescaled data of I_p multiplied by the factor of the ratio. e.g. $I_p^*[N = (1, 2)] = \frac{3}{2}I_p[N = (1, 2)]$. All datasets fall onto one trace. I_p not only decreases with increasing N_{tot} (or the increasing coupling strength between the dot and reservoirs), it is proportional to N_{tot}^{-1} as demonstrated in the inset of Fig. 5.4(b). The results imply that the generated current is a type of charge pump as argued in the following. (1) The escape rate Γ_{esc} of electron in an open quantum dot is determined by the total channel number N_{tot} and follows $\Gamma_{esc} \sim \frac{N_{tot}\Delta}{2\pi^2}$. The escaping or leaking of electrons from the dot increases with the increasing coupling strength which also reduces the time electrons relax to the reservoirs. One would expect a the performance of pumping to be suppressed by an increased coupling strength due to the opening of the dot [128, 129, 130, 131], or the dephasing due to the inelastic scattering from a third fictitious voltage probe[132]. (2) If the current is a result of any circuitry effect (e.g. classical dependence of the resistance on

the applied electric fields or cross talk between the electric fields), I_p would increase with increasing the dot resistance regardless of the mode number N , and $I_p [N = (0, 0)]$ should be greater than $I_p [N = (1, 1)]$. But this scenario does not apply to our results here.

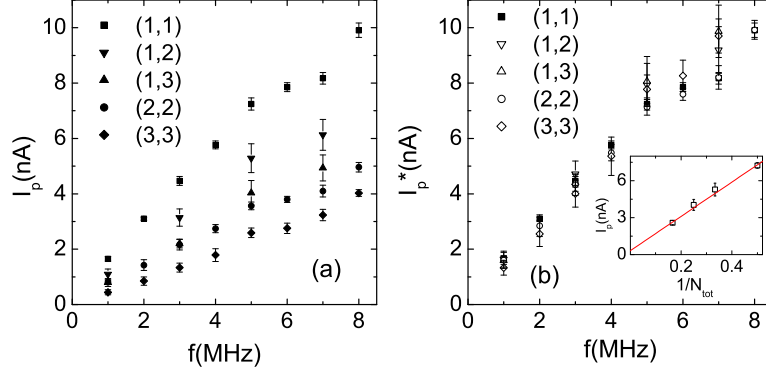


Figure 5.4: (a) DC current generated in setup 1, I_p , as a function of frequency for an open dot having different transmission mode numbers in QPC1 and QPC2. Each data point are averaged over five dataset of $I_{dc}(\Delta\phi)$. N are (1, 1)■, (1, 2)▼, (1, 3)▲, (2, 2)● and (3, 3)◆ respectively. $V_{ac}=15$ mV. (b) Rescaled current, I_p^* , vs. f for the same mode numbers. $I_p^*(N) = \frac{(N_{qpc1}+N_{qpc2})}{2} I_p$. I_p of $N=(1, 2)$, (1, 3), (2, 2), and (3, 3) are multiplied by the total mode number ratio to $N=(2, 2)$. Inset: I_p vs. N_{tot}^{-1} for 5 MHz.

The current generated in setup 2 has completely different features. As shown in Fig. 5.5, I_r decreases with increasing frequency for $f \sim 100$ kHz–1 MHz, and then increases very slightly from 1 MHz to 5 MHz for various mode numbers. For comparison, $I_p(f)$ for $N=(2, 2)$ is also plotted in the same panel as the starry points. I_r is presenting a very dissimilar frequency dependence compare to I_p . In addition, as opposed to setup 1, I_r is the smallest for $N=(1, 1)$ at a fixed frequency, increases with N , and saturates at higher mode number for $N \geq (3, 3)$. No specific relation between the current and the mode number is noticed. In this setup, the source-drain voltage V_{sd} , and the dot conductance $G = R_{dot}^{-1}$ is expected to oscillate with the same frequency. Similar to the rectification mechanism, the current $I_r = \frac{\omega}{2\pi} \int_0^{2\pi/\omega} V_{sd}(t)G[V_{s2}(t)]dt$, where $V_{sd}(t) = V_{sd,ac} \sin(\omega t + \Delta\phi)$ and $V_{s2}(t) = V_{s2,ac}(\omega t)$. For small driving amplitude, $G[V_{s2}(t)] \approx G + \frac{\partial G}{\partial V_{s2}} \delta V_{s2}$ and $I_r \approx V_{sd,ac} V_{s2,ac} \frac{\partial G}{\partial V_{s2}} \frac{\cos \phi}{2}$, independent of ω . As shown in Fig. 5.5 I_r has a rarely slow response to f compared with I_p for $1 \text{ MHz} < f < 6 \text{ MHz}$. Besides, the rate of increase in I_r with respect to f is almost the same for different transmission modes N .

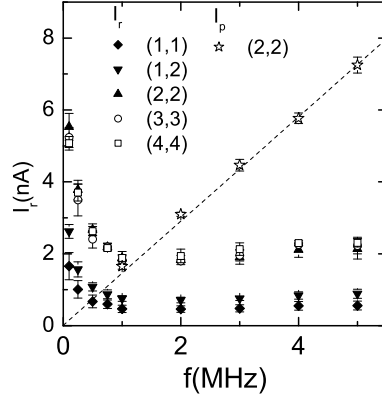


Figure 5.5: DC current I_r as a function of frequency for various mode number. $N=(1,1)$ ◆, $(1,2)$ ▼, $(2,2)$ ▲, $(3,3)$ ○ and $(4,4)$ □ respectively. $V_{sd,ac}=1$ mV and $V_{s2,ac}=25$ mV. For comparison, $I_p(f)$ for $V_{ac}=15$ mV and $N=(2,2)$ ☆ and its linear fit (dashed line), are also plotted.

To further investigate the characteristics of the two dc currents, transport in perpendicular magnetic fields B was also studied. The magnetic field is normal to the plane of the 2DEG (open dot). The dot resistance as a function of B is presented in Fig. 5.6(a) for $N = (2,2)$ and $(3,3)$. Both traces are symmetric in magnetic field. R_{dot} decreases with increasing B due to weak localization for $|B| \lesssim 130$ mT. [133, 134] R_{dot} decreases from ~ 12 k Ω at $B=0$ to ~ 10.8 k Ω for $N=(2,2)$ and from ~ 8.4 k Ω at $B=0$ to ~ 7.3 k Ω for $N=(3,3)$. Then resistance increases with increasing field for $|B| \gtrsim 130$ mT. Figs. 5.6(b) and 5.6(c) show the magnetic field dependence of I_p and I_r for various frequencies. Compared with Fig. 5.6(a), $I_p(B)$ and $I_r(B)$ show no direct correlation with $R_{dot}(B)$. Additionally, I_r becomes asymmetric with respect to B with the increased frequency while the magnetoresistance of the dot is symmetric about B . E.g. the 3 MHz trace is more asymmetric than the 100 kHz trace. The results again suggest that the possibility of the circuitry effects can be ruled out here for both I_p and I_r . On the other hand, the magnetic field dependences of the current show discrepancies in I_p and I_r . I_p overall increases but I_r decreases with increasing $|B|$. This difference further support that I_p and I_r are indeed generated by different mechanisms.

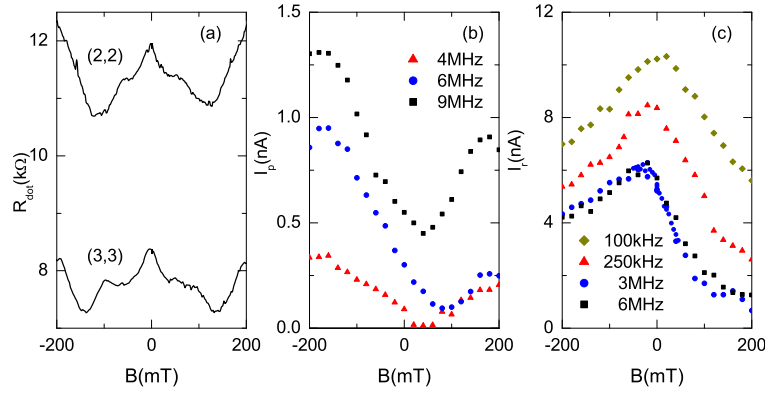


Figure 5.6: (a) Dot resistance as a function of perpendicular magnetic field for $N=(2,2)$ and $(3,3)$. (b) I_p vs. B for three frequencies at $N=(2,2)$ for $V_{ac}=30$ mV. (c) I_r vs. B for four frequencies at $N=(3,3)$ for $V_{s2,ac}=25$ mV and $V_{sd,ac}=1.25$ mV.

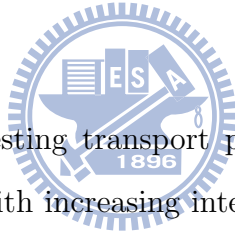
5.4 Summary

In summary, dc currents in an open dot are generated from two time dependent electric fields in two different electrical setups. The currents show different dependences on frequency, mode number, and perpendicular magnetic field. I_p increases linearly with increasing frequencies for $f \lesssim 8$ MHz. It decreases with the total mode number (or the coupling strength) in the relation of $I_p \propto (N_{qpc1} + N_{pqc2})^{-1}$, which may be attributed to the relaxation of the electrons from the dot. As soon as the dot is closed while the resistance is still finite, I_p drops quickly close to the experimental resolution. I_p on the whole increases with increasing magnetic field. On the contrary, I_r decreases with increasing f and becomes insensitive to frequency for $f \gtrsim 1$ MHz. It increases with the increasing mode number, and saturates at higher mode number for $N \geq (3,3)$. I_r decreases with the increasing $|B|$. Moreover both $I_p(B)$ and $I_r(B)$ can be asymmetric and have no direct correlation with the dot resistance $R_{dot}(B)$. We believe that the classical circuitry effects can be ruled out for the current generation. The results suggest that I_p and I_r are indeed originated from different mechanisms, and can be distinguished by the experimental configurations presented here. Our results should provide a new direction for the applications of ac-dc signals converting.

Chapter 6

Ballistic transport in double quantum point contacts in series

6.1 Introduction



In the previous chapters, interesting transport phenomena in a single quantum point contact have been discussed. With increasing interest in nanostructures and their scope for novel functionality, the exploration of the ballistic and coherent natures of transmission through these gate confined nanostructures will never suffice. In this chapter, we extend to more intricate cases of ballistic transport, specifically, transport of coupled QPCs. We present measurements of two arrangements of coupled QPCs; devices A and B: two QPCs are coupled in series and separated by a two dimensional electron sea, and device C: one *narrow* QPC placed next to the other *wide* constriction.

Transport through two serially placed QPCs was investigated experimentally and theoretically around two decades ago.[105, 135, 136, 137, 138, 139, 140] However, the influences of system property and coupling between system and environment on the adiabatic transport are still not yet explored. The ballistic transport can be greatly affected by the details of shape and arrangement of the device. Previous studies reveal that the direct transmission (T_d) across two serially connected QPCs decays monotonically with the increasing spacing (L) between them and transport behaves ohmically when $L \gtrsim 1.1\mu\text{m}$,

about one tenth of mean free path.[141] We show that T_d is inversely dependent with L as predicted by Beenakker *et al.* in Ref.[136] due to the dependence of L on electron collimation. In addition, the electrical transport of double QPCs in series with various coherent lengths which are controlled by carrier density is also studied. T_d decreases with the decreasing carrier density.

When two QPCs with different widths are placed next to each other, the conductance is demonstrated to oscillate as the subband energy of one QPC changes. The oscillations reflect the interference of incident and backscattering electrons due to mode mismatch. By reducing the carrier density with the top gate voltage, the amplitude of oscillations decreases accordingly resulting from the coherence suppression. With increasing source-drain voltage, the interference oscillation is suppressed due to enhanced inelastic scattering.

6.2 Device arrangements

Three sets of devices were exploited. Device A as shown in Fig. 6.1(a) contains two identical split gate pairs (sg1 and sg2) which have topological gap width of $0.45 \mu\text{m}$, channel length of $0.5 \mu\text{m}$, and edge-to-edge spacing of $\sim 0.6 \mu\text{m}$. Device B as shown in Fig. 6.1(b) has four pairs of split gates with various separation distances. By selecting different pairs of split gates, the edge-to-edge distance (L) of two QPCs ranges from $\sim 0.3 \mu\text{m}$ to $2.4 \mu\text{m}$.

Device C contains four Ti/Au gates (A, B, R, and L) and four independent sets of ohmic contacts (1–4) as shown in Fig. 6.1(c). When gates B, R, and A are applied with a negative voltage, a wide confinement containing many transmission modes is created by gates B and A next to a second narrow QPC created by gates R and A. On top of the metal gates of devices A and C, being isolated by a $\sim 100 \text{ nm}$ thick dielectric layer of cross-linked Polymethylmethacrylate[142], a top metallic gate (tg) was fabricated to control the carrier concentration. Differential conductance was carried out by the four-terminal ac lock-in technique with a small ac excitation voltage of $5 - 10 \mu\text{V}$ in the cryostat Heliox VT at the base temperature of 0.3 K .

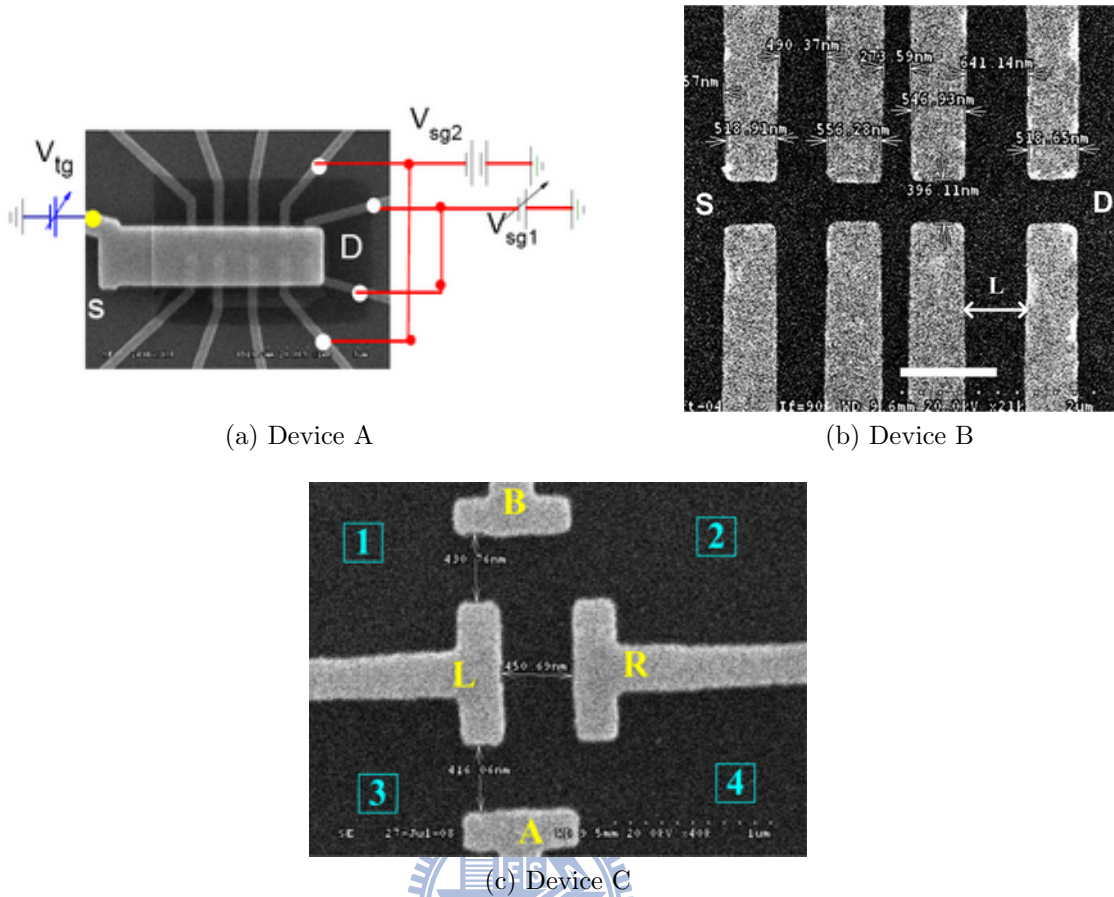


Figure 6.1: SEM images and schematics of gate configuration for three different devices. (a) Device A: Two pairs of $0.5 \mu\text{m}$ long split gates separated by $\sim 0.6 \mu\text{m}$. (b) Device B: four pairs of $0.5 \mu\text{m}$ long split gates with various separation distances. The white bar indicates a length of $1 \mu\text{m}$. (c) The gray areas represent four Ti/Au gates, while the number indicates four separate sets of ohmic contacts.

6.3 Density and length dependences of ballistic transport

When the negative voltage is applied to a pair of split gates, the potential depletes 2DEG to form the 1D channel resulting in the typical quantized conductance. As shown in Fig. 6.2, there are conductance plateaus in units of $2e^2/h$ due to the transmission of 1D subbands for QPC1 of Device A. As known, 1D transport is sensitive to the carrier density which can be effectively tuned by the biasing top gate voltage V_{tg} . The more negative V_{tg} is, the less carrier density n is and vice versa. The more positive V_{tg} is, the more carrier density n is. Quantized conductance for a series of V_{tg} is also demonstrated in Fig. 6.2. The carrier density is smoothly decreased from left to right corresponding to

that the threshold V_{sg} for pinching off becomes less negative continuously. The number of plateau is determined by the number of subband with energy less than Fermi energy E_F . As seen in the inset of Fig. 6.2, the reduction of V_{tg} leads to the decrease of the observed plateau number implying the decrease of E_F . Besides, when carrier density is large the conductance plateaus are more clear. Once carrier density is severely reduced, the plateau disappears.

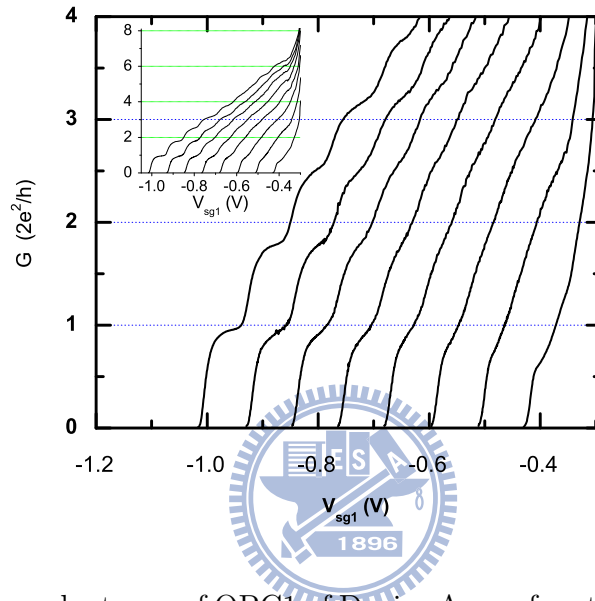


Figure 6.2: Quantized conductance of QPC1 of Device A as a function of split gate voltage at $T=0.3$ K for different top gate voltages. From left to right: V_{tg} decreases from $+0.4$ V to -1 V in steps of 0.2 V. Inset: Selected data curves are shown in larger y-scale.

It has been well known that the carrier density depends on V_{tg} in heterostructures in either 1D or 2D.[85] Fermi energy is determined by carrier density and dimensionality following $E_F = \pi^2 \hbar^2 n_{1D}^2 / 8m^*$ in 1D and $E_F = \pi n_{2D} / 2m^*$ in 2D where n_{1D} and n_{2D} are carrier densities in 1D and 2D, respectively. m^* is the effective mass of carrier. Here, the transconductance as a function of V_{tg} against V_{sd} referred to as the half-plateau method¹ based on Glazman and Khaetskii model[26] is used to obtain the subband energy level spacing and the corresponding Fermi energy.[27] Both calculated carrier densities versus V_{tg} in 1D and 2D models are plotted in Fig. 6.3. As seen, carrier density is indeed effectively changed by tuning V_{tg} .

As illustrated in Fig. 6.1(a), all pairs of split gates were made nearly identical. Features

¹See section 1.3.3 for more detailed discussion.

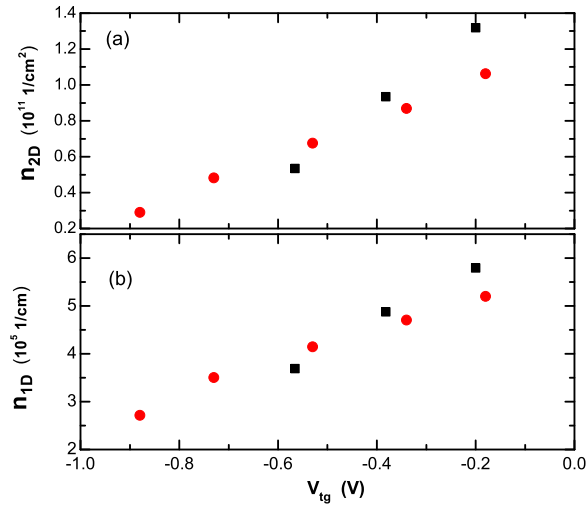


Figure 6.3: (a) Calculated two dimensional carrier density versus top gate voltage for QPC1 of Device A at 0.3 K. (b) Calculated one dimensional carrier density versus top gate voltage for QPC1 at $T=0.3$ K. Subband index of QPC1 is confined at $N=4$ (black squares) and $N=6$ (red circles), respectively.

of ballistic transport through each QPC, e.g. quantized conductance versus gate voltage, is nearly the same. In the following, we focus on the transmission through serially connected QPC1 and QPC2. Conductance as a function of split gate voltage applied to one QPC was measured with the other kept in some specific 1D subbands N . In Fig. 6.4, we show a typical result of the conductance G_{series} of the serially connected pair of QPCs versus V_{sg1} against a series of V_{tg} while QPC2 is confined to a particular subband number $N=2$ (V_{sg2} is held constant). The arrangement of gate voltage is also sketched in Fig. 6.1(a). From the adiabatic transmission point of view, the device conductance is completely determined by the narrowest QPC with the least number of subbands for transmission.[105] Only two plateaus are expected since QPC2 is confined at $N=2$. However, there are more than two plateaus for all curves in Fig. 6.4. In addition, the series conductance at the plateau is less than the quantized conductance value of single QPC at the corresponding N . These differences indicate that the transmission through this device is not completely adiabatic.

The ballistic transport can be characterized by the direct transmission probability T_d which reflects the probability of electrons traveling directly from QPC1 to QPC2 without momentum relaxation and loss of coherence. The completely adiabatic transport of $T_d=1$

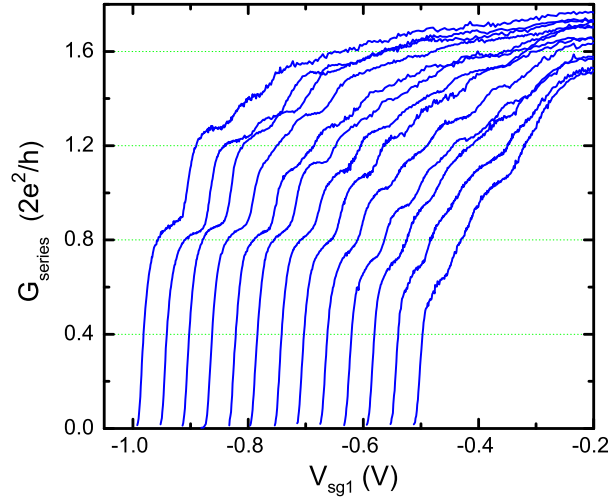


Figure 6.4: Conductance of two serially connected QPCs of Device A as a function of V_{sg1} against a series of V_{tg} at 0.3 K. V_{tg} decreases from +0.4 V to -0.8 V in steps of 0.1 V. QPC2 is confined at $N=2$.

was reported by van Wees *et al.* in high magnetic fields such that electrons have a high degree of collimation.[135] In the absence of magnetic field, the completely adiabatic transport was rarely observed. With the consideration of real geometry that two identical quantum point contacts facing each other at opposite boundaries of 2DEG by Beenakker *et al.* and Beton *et al.*[136, 137], the series conductance through serially connected two identical QPCs of conductance G can be written as

$$G_{series} = \frac{1}{2} \left(G + \frac{2e^2}{h} T_d \right) \quad (6.1)$$

Therefore, we can obtain T_d from series of traces as those shown in Fig. 6.4. For instances, we find the value of G_{series} at the second plateau in Fig. 6.4 and substitute in Eq. 6.1 to calculate T_d for $N=2$. We demonstrate all calculated values of T_d in Fig. 6.5. The normalized transmission probability T_d/N decreases continuously from 0.6 to 0.1 with decreasing top gate voltage (carrier density) when both QPCs are confined at only one 1D subband ($N=1$). The transport is partially adiabatic in high electron densities and transits to nearly complete ohmic ($T_d \sim 0$) in low densities. When both QPCs are confined at more than one 1D subband ($N>1$), T_d/N is smaller than that for $N=1$, but seems to be insensitive to N for $N=2, 3$, and 4. Moreover, T_d/N saturates and is about

0.3 for positive top gate voltages. When the top gate voltage is negative, T_d/N decreases with decreasing V_{tg} similar to that for $N=1$.

According to Eq. 6.1, when $T_d = 1$, $G_{series} = G$ indicating a completely adiabatic transport. When $T_d = 0$, Eq. 6.1 leads to that $G_{series} = G/2$ for a completely ohmic transport. In the theoretical model, the reality that the two QPCs are separated by a region of large unrestricted 2D electron sea was taken into account.[136] For the completely adiabatic transport, the electrons should travel ballistically across the 2DEG region from one QPC to the other while preserving their 1D momenta. Hence, the transmission through a series of pairs of QPCs depends on the details of confinement potentials and 2DEG. Takagaki and Ferry predicted that T_d/N becomes smaller with increasing N because the opening angle of the constriction increases as W/L increases where W is the effective gap width and $N=k_F W/\pi$. [105] However, the variation is less pronounced in the quantum-mechanical calculation since the lower-lying mode are most likely to be transmitted. Here, both QPCs are at a distance of $L=600$ nm that is much longer than the Fermi wavelength ($\lambda_F=57$ nm) at $V_{tg}=0.4$ V. Moreover, calculation of T_d/N in terms of L/W in Ref.[139] gives much smaller value. For example, $T_d/N < 0.05$ using Takagaki's method which is about 0.58 in Fig.6.5 for $N=1$ and $V_{tg}=0.4$ V. The effect of the electron collimation seems be either overestimated or less important in our case.

In our device, the negative split gate voltage was applied to produce electrostatic 1D confinement. The top gate voltage determined the carrier density of the unconstricted 2DEG as well as both quantum point contacts. In quantum devices, electron-electron interaction becomes more important in low carrier densities. As reported by Kane *et al.*, both mobility and mean free path decrease when the top gate tuned carrier density is less than a critical value.[85] The trend is similar to the data curves of T_d/N for $N=2, 3$, and 4 in Fig. 6.5. Mean free path is about $10 \mu\text{m}$, much longer than some characteristic lengths such as L and W , and has no direct relevance with T_d . On the other hand, the coherent length is closely related to mobility and mean free path. For completely adiabatic transport, the phase of scattering electrons should be preserved across the unconstricted 2DEG. However, the electron-electron interactions introduce the effect of dephasing and hence,

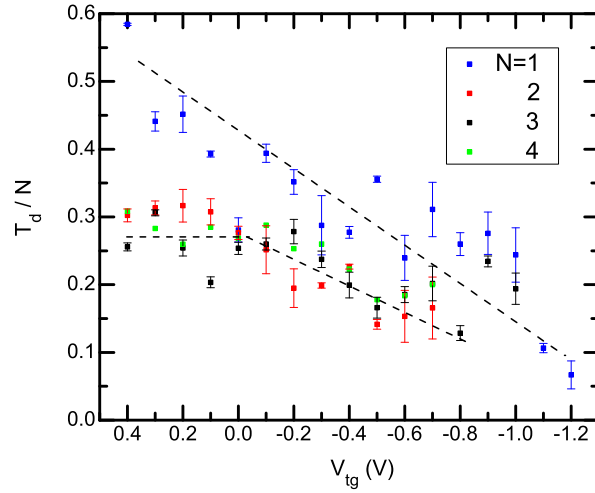


Figure 6.5: Normalized transmission probability T_d/N versus top gate voltage V_{tg} for serial QPCs of some identical confined subband indices N of device A. Dashed lines are guides to the eye.

transport approaches to ohmic regime. This may explain qualitatively the experimental findings that T_d/N saturates in high carrier densities, decreases with decreasing carrier density in low carrier densities, and is insensitive to the effective gap width W (subband index N). As for $N=1$, the large values of T_d/N compared with other mode number is probably due to the lack of inter-mode scattering. Further investigation is required on this issue.

Direct transmission across two QPCs separated intermittently by 2DEG is expected to decrease with increasing edge-to-edge distance L between two QPCs due to decreasing collimation angle.[136] When T_d decreases, it implies that the ratio of coherent electrons traveling across two QPCs decreases as well. Fig. 6.6 shows the conductance of double QPCs after subtracting the resistance contributed from the second quantum point contact by aligning the last plateau to $2e^2/h$. The conductance of QPC2 is fixed at $\sim 4e^2/h$ with a mode number of two. G_s^* as a function of V_{qpc1} , the gate voltage applied on QPC1, shows five robust quantization steps for $L = 2.4 \mu m$ in the left panel and six steps in the middle panel.

At higher subbands for $N \gtrsim 5$, conductance oscillations are observable suggesting quantum interference. The interference at higher subbands becomes stronger as L decreases,

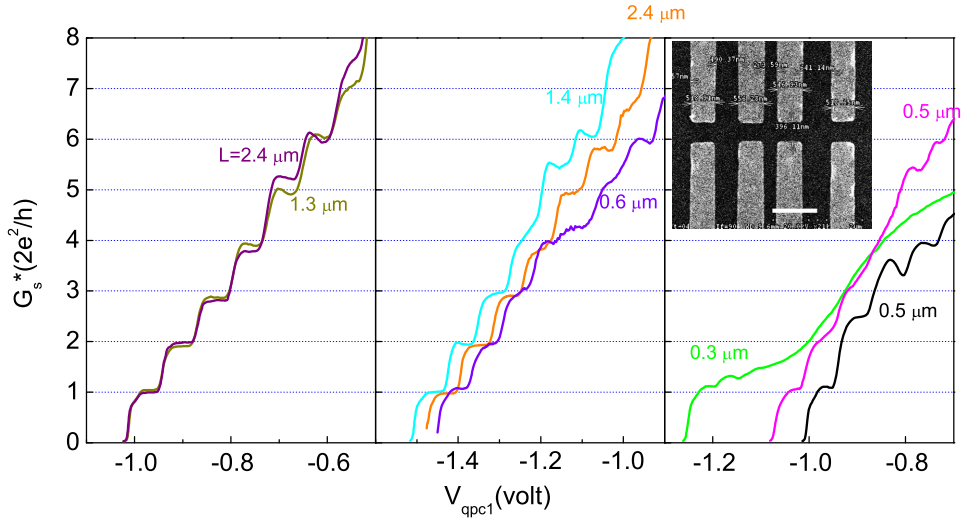


Figure 6.6: G_s^* vs. V_{qpc1} when QPC2 is controlled at $\sim 4e^2/h$ ($N_{qpc2} = 2$) for various QPC selections with different separation distances in Device B. The measured conductance across two QPCs is subtracted by a serial resistance of $\sim 6 k\Omega$ aligning the last plateau to $2e^2/h$ to obtain G_s^* .

e.g. the $L = 1.4$ and $0.6 \mu m$ traces in the middle panel. The transport resolves from ohmic regime into adiabatic regime when L reduces down to $L \lesssim 0.5 \mu m$. The adiabatic transport manifests as more missing plateaus and less well defined quantization as the G_s^* traces in the right panel demonstrated. Notice that two steps are developed for $L = 0.5 \mu m$ but only one step is observed for $L = 0.3 \mu m$.

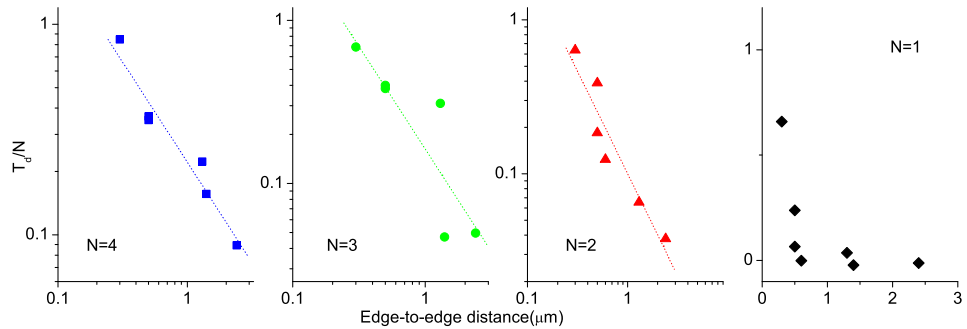


Figure 6.7: Normalized direct transmission T_d/N as a function of edge-to-edge distance between two QPCs for $N = 4$ (leftmost) to $N = 1$ (rightmost). ($N = N_{qpc1} = N_{qpc2}$.) The dashed lines are the fit to $T_d/N \propto L^{-\alpha}$ by least square regression. $N=4-2$ are plotted in logarithmic scale, while $N=1$ is plotted in linear scale.

The direct transmission probability T_d can be analyzed in the same way as previously

discussed. T_d was expected to be proportional to L^{-1} since the collimation angle decreases as L increases.[136] Fig. 6.7 shows the normalized transmission factor T_d/N as a function of L for mode number $N_{qpc1} = N_{qpc2} = N=4$ to $N=1$. T_d decreases from ~ 0.6 – 0.8 to less than 0.1 as L increases to $\sim 2.4 \mu m$ for $N=4$ – 2 . The data in the logarithmic plot follows a relation of $T_d \propto L^{-\alpha}$ where α extracted from numerical fitting is ~ 0.95 – 1.3 . The extracted value of α is comparable with the theoretical prediction of unity, however dephasing in 2DEG and the detailed geometrical structure may account for the deviation. For $N = 1$, T_d/N drops more rapidly with increasing L and reaches close to zero for $L \gtrsim 0.6 \mu m$. Due to the insufficient resolution for $L \leq 0.5 \mu m$, numerical fitting for determining α is unreliable. The mechanism of faster decay of T_d for $N = 1$ than higher mode numbers remains to be explored.

6.4 Density dependence of quantum interference

In the following, we discuss the transport across two QPCs without unrestricted 2DEG in between. Fig. 6.8(a) shows the conductance of a narrow QPC as a function of V_{R-B} ($V_R = V_B = V_{R-B}$) while gate L and A are not functioning in device C. G_{12} reveals several quantization steps. When a gate voltage V_A is applied in addition to V_{R-B} a wider QPC is formed next to the narrow QPC. In contrast to devices A and B, the 2D electron sea separating the QPCs is absent here and the two QPCs are coupled directly. Analysis by the direct transmission method is therefore not appropriate here. As the illustration in the lower inset of Fig. 6.8(a) demonstrates, electrons would be backscattered due to misaligning subband bottoms of two QPCs. The incident wave interferes with the backscattered wave and the transmission across both QPCs oscillates by continuously changing one of the energy levels.

The conductance G_{12} oscillates as a function of V_A as expected when V_{R-B} is fixed. Fig. 6.8(b) presents the conductance variation $\Delta G_{12} = G_{12} - \overline{G}_{12}$ against V_{tg} while V_{R-B} is set to keep the conductance of the narrow QPC at $\sim 2.7G_0$. The averaged conductance of a dataset \overline{G}_{12} was subtracted in order to present the results more effectively. For $V_{tg} = 0$, ΔG_{12} reveals about seven conductance oscillations with amplitude of $\sim 0.067G_0$. When

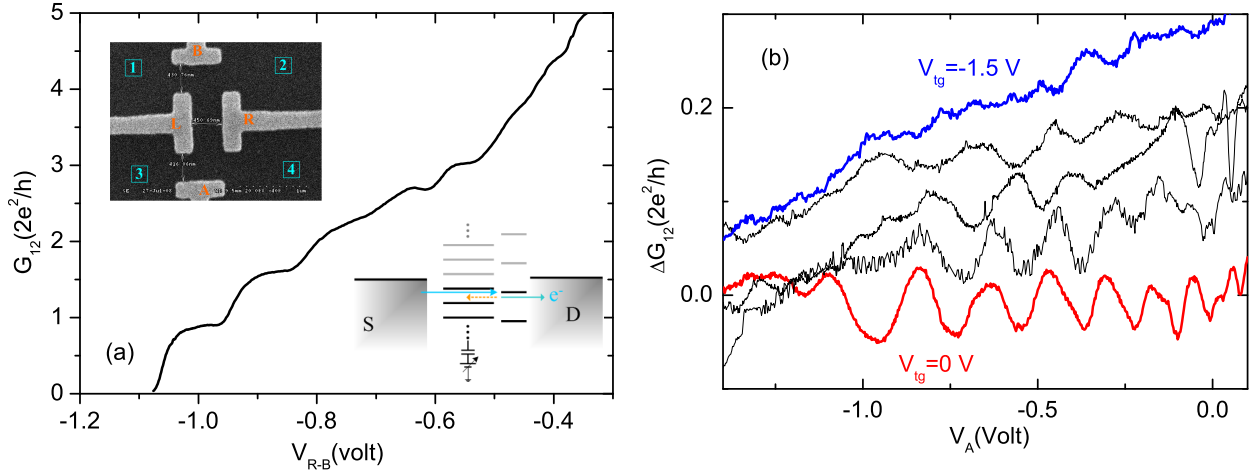


Figure 6.8: (a) Linear conductance of a single QPC confined by gates B and R of Device C as a function of gate voltage V_{B-R} . Lower inset: illustration of energy states when two QPCs are coexisting. (b) The conductance variation measured by lead 1 and 2 as a function of V_A for various V_{tg} while two QPCs are developed next to each other. The imposed V_{B-R} is for $G_{12} \sim 2.67 G_0$ when V_A is not functioning. $V_{tg} = 0, -0.5, -0.8, -1.2$ and -1.5 V, respectively. Traces are offset for clarity.



the density is reduced by decreasing V_{tg} from 0 to -1.5 V, the oscillations are getting weaker and smoother. For $V_{tg} = -1.5$ V, oscillations are mostly suppressed except a slight peak at $V_A \sim -0.35$ V. Since quantum interference requires the coherence of electrons, the data suggest that the coherence is strongly destroyed in low electron densities or large negative V_{tg} . The result is in consistence with the previous discussions in Refs. [7, 85].

It is also well known that inelastic scattering is detrimental to quantum coherence and therefore leads to dephasing. Fig. 6.9 presents $\Delta G_{12}(V_A)$ for $V_{sd} = 0$ to 1.7 mV. With V_{sd} being increased, the inelastic scattering is increased as well. Clearly, the oscillations are suppressed with V_{sd} . When V_{sd} is as large as -1.7 mV, the oscillations are quite imperceptible. Additionally, the last three peaks for $V_{sd} = 0$ move linearly with respect to V_{sd} for $V_{sd} \lesssim 1.2$ mV as indicated by the guide lines. This implies that the position of the peaks reflects the relative energy difference of the QPCs and further confirms the scenario of two QPCs coupled in series in this device.

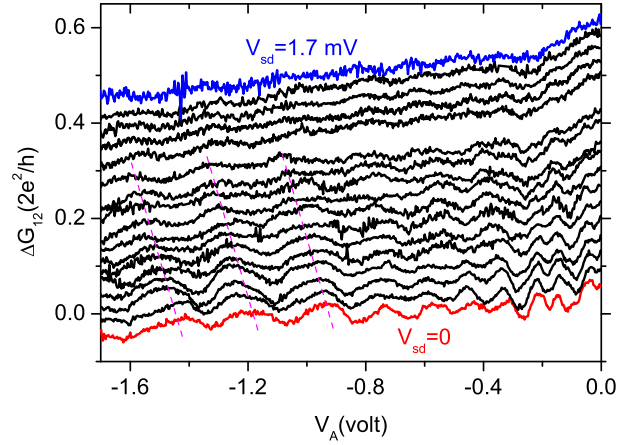


Figure 6.9: Conductance variation ΔG_{12} as a function of V_A against V_{sd} for $V_{tp} = 0$ when two QPCs are developed next to each other in Device C. Traces are offset for clarity. $V_{B-R} = -0.8V$; $G_{12}(V_A = 0) = 2.63G_0$.

6.5 Summary

We have measured electric transport of serially connected two quantum point contacts for three types of devices. When the two QPCs are separated by an unrestricted 2D electron sea, the transmission probability T_d is obtained according to the theoretical model proposed by Beenakker *et al.*. The results show that the normalized transmission probability T_d/N decreases with decreasing carrier density or increasing separation and the transport transits to be nearly ohmic ($T_d \sim 0$). When the two QPCs are coupled directly to each other, the conductance oscillations reveal the interference between the incident and backscattered electrons. The quantum interference is suppressed by either decreasing the electron density or increasing the bias voltage V_{sd} . We suggest that low carrier density may enhance electron-electron interaction resulting in short coherence length which is detrimental to ballistic transport.

Chapter 7

Conclusions and future work

7.1 Summary


This dissertation demonstrate series of experiments that evince the ballistic and quantum essences as well as electron-electron interactions in mesoscopic devices. The experiments took advantages of long coherence length and mean free path of 2DEG together with the advanced modern nanofabrication technologies and low temperature techniques.

In the first experiment (Chapter 3), the source drain bias spectroscopy shows ZBA in short and high density QWs. The feature is suppressed with the decreasing carrier density by tuning a top gate voltage. ZBA is suppressed as well For the channel length elongated to more than $0.8 \mu m$. The characteristic temperatures, activated temperature T_a and cut off temperature T_c , scale with the ZBA width. These features are describable by the enhanced electron-electron scattering in QWs. The second experiment (Chapter 4) presents the effect of impurities on the linear and nonlinear conductances of QWs. The linear conductance displays lowered quantized steps, smeared plateaus, and resonances in disordered QWs. The bias spectroscopy of non-equilibrium transport shows trace crossing and peak splitting. The transport characteristics vary with respect to different impurity configurations by lateral shifting and thermal cycling. In contrast, both linear and nonlinear conductances of clean QWs are relatively robust. The results are congruent with theoretical predictions and describable by the existence of quasibound states.

In the third experiment (Chapter 5), dc currents generated from two time dependent

electric fields in the absence of external bias in open dots were studied. The dependences of dc currents on coupling strength between the dot and reservoirs, frequency, and out-of-plane perpendicular magnetic fields diversify between charge-pump-like and rectifier-like setups. The results distinguish charge pumping type current from rectification. In the final experiment (Chapter 6), coherent transport consequentially across two QPCs is presented. When the two QPCs are separated by 2DEG, the coherent transport can be analyzed and characterized by ‘direct transmission’ which is affected by the 2DEG coherence length and physical geometries of device arrangement. Transport becomes completely ohmic in low carrier densities or with long separation distances. When the two QPCs are placed closely next to each other, conductance oscillations due to quantum interference are observable. The interference is suppressed due to coherence suppression with decreasing carrier density.

7.2 Future work



The understanding of mesoscopic physics is far from over. As far as the fundamental physics is concerned, unresolved issues of transport still remain in low electron densities and require further commitment. In one of the issues, for instance, our devices show weak Zeeman-splitting steps at $B \sim 8 - 9$ T unlike several other published works that spin-resolved conductance quantization manifests at $B_{in} \gtrsim 8$ T. Similar problems were also noticed by J. P. Bird according to private communications. In another issue, our experiments on the 0.7 anomaly do not show consistent result with respect to the device geometries which is contradicted to other reports. The exact factor that influences the 0.7 anomaly is not yet certain. Since the effects of geometrical arrangements relative to the lattice direction on the magnetotransport of 0.7 anomaly has not been discussed, it may be worth to systematically investigate.

As discussed in section 3.3, it has been demonstrated that magnetic moments in two QPCs coupled by the overlapping of wave functions leaking across a tunneling barrier lead to conductance resonance.[73, 74, 75, 76] Inspired by these works, I believe that the study of more intricate systems will help discover more interesting physics. One can impose the

arrangements presented in appendix A that two QPCs couple to each other mediating via a 1D conducting channel. One can also adopt electron focusing technique to aim the electron flow from one QPC to the other. Rather than the tunneling hybridization of wavefunctions, another mechanism is expected to play the dominant role. In these cases, RKKY interaction may be the potential candidate. Detailed investigations are required and worth a study.

With the accumulated and matured experience of measurement and fabrication of low dimensional semiconductor devices, it is sensible and plausible to extend the research to more challenging fields and to expand our perspectives. Exploiting wet etching with PMMA as the mask, it is easy to fabricate Aharonov-Bohm rings with sub-micron resolution in GaAs/AlGaAs or other types of 2DEGs. Dephasing and phase shifting of AB interference in low magnetic fields have been studied.[143, 144] Imposing split gate QPCs together with top gate to the etched AB rings, it is possible to further investigate the influences of mode occupation and electron density on dephasing. In high magnetic fields when the edge states were developed, the velocity of edge-state electrons were obtained from the transport data of Fabry-Perót interferometers.[145] In the quantum hall regime, a AB ring may also become a Fabry-Perót interferometer or somewhere in between. It is worth studying the transport of the edge-state electrons in different carrier densities and geometrical arrangements.

Finally, it is worth mentioning that graphene is gaining massive attention in recent years. Due to the high quality electrical characteristics, graphene is considered as a candidate to replace silicon for the next generation of electronic applications. [146, 147] It may also provide a tool to study richer low dimensional physics or verify particle physics in condensed matters.[148] Therefore, research of transport in graphene is also worth devoting to.

Appendix A

Two QPCs coupled by a 1D channel

Refs. [73, 74, 76, 75, 149] demonstrated a series of experiments and theory on two QPCs coupled via wavefunction overlapping. Either being coupled by a quantum dot or a wide 2D electron sea, a conductance resonance is observed whenever a second QPC is closed around pinch-off. In parallel, energy spectroscopy of coupled QPCs has also been reported by other groups. Two coupled QPCs can be created by a tunneling barrier developed by biased metal gates[150], two vertically stacked quantum wells forming two layers of 2DEGs[151], or a broad quantum well that contains one ground state and one excited state[152, 153]. Due to state hybridization, crossing and anti-crossing were observed in the energy spectrum. Inspired by the works, we tried reproducing the results and extending to two QPCs coupled by a 1D channel. It is interesting to explore how far the wavefunction of a QPC can stretch out? Are two QPCs coupled via wavefunction overlapping or propagation of quantum information? For the latter, it is prospective for future application of quantum computing.

Here, I presented the preliminary results of two QPCs coupled by a $\sim 0.8 \mu m$ long 1D quantum channel. The data shows that the information of states can propagate from one QPC to the other along the 1D channel. The inset of Fig. A.1 presents the layout of the device which contains four independent groups of ohmic contact 1–4. Gate L and R were used to confine the mediating 1D channel. As shown in Fig. A.1, conductance G_{13} vs. $V_{L-R} = V_L = V_R$ reveals more than eight quantization steps. Also indicated on the plot are the four V_{L-R} used to control the 1D channel for a specific transmission mode

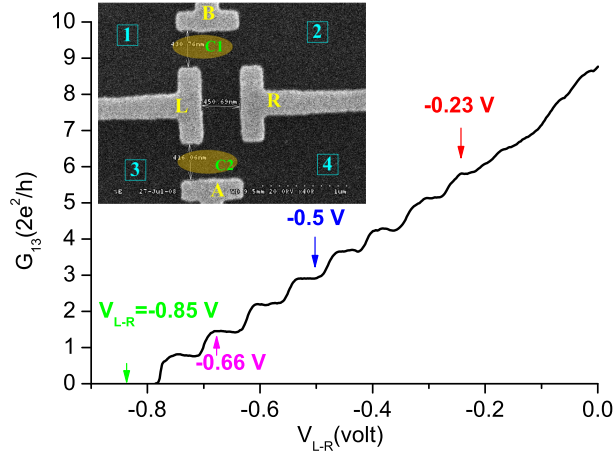


Figure A.1: Conductance of the $0.8 \mu\text{m}$ QW as a function of gate voltage V_{L-R} . Also indicated on the graph are the voltages used for coupling the two QPCs. Inset: SEM images of the device and schematics of electrical configuration.

number N . $N = 8, 4, 2$ and 0 for $V_{L-R} = -0.23, -0.5, -0.66$, and -0.85 V, respectively.

When a negative voltage is applied on gates B and A after the 1D channel is developed, G_{12} measures the transmission of confinement C1 while G_{34} measures the transmission of confinement C2. From Figs. A.2(a)–(d), V_A is swept with V_B fixed while G_{12} and G_{34} are measured separately. From the pinchoff, G_{34} shows several conductance steps along the trace in Fig. A.2(a) when $N = 8$. Interestingly, $G_{12}(V_A)$ presents conductance oscillations that seem to correlate with the G_{34} plateaus. Similar result can be observed in Fig. A.2(b) for $N = 4$. Further reducing the mode number to 2, G_{34} presents stronger conductance resonances as shown in Fig. A.2(c). However, $G_{12}(V_A)$ still reveals peaks that follow the resonances of G_{34} . The correlation is almost broken when the 1D channel is pinched off. G_{34} presents even stronger conductance resonances, but G_{12} does not show correlations with confinement C2 in Fig. A.2(d) when $N=0$.

Due to the geometric design, confinements C1 and C2 are not exactly a QPC. The edge is not straight and zero-dimensional states may exist due to possibly local potential minimum. Therefore, the G_{34} plateaus are lower than the multiples of $2e^2/h$ and contain resonances on the traces. This study would be further improved by appropriately redesigning the device and can be expanded to more intricate cases to investigate subtler physics.

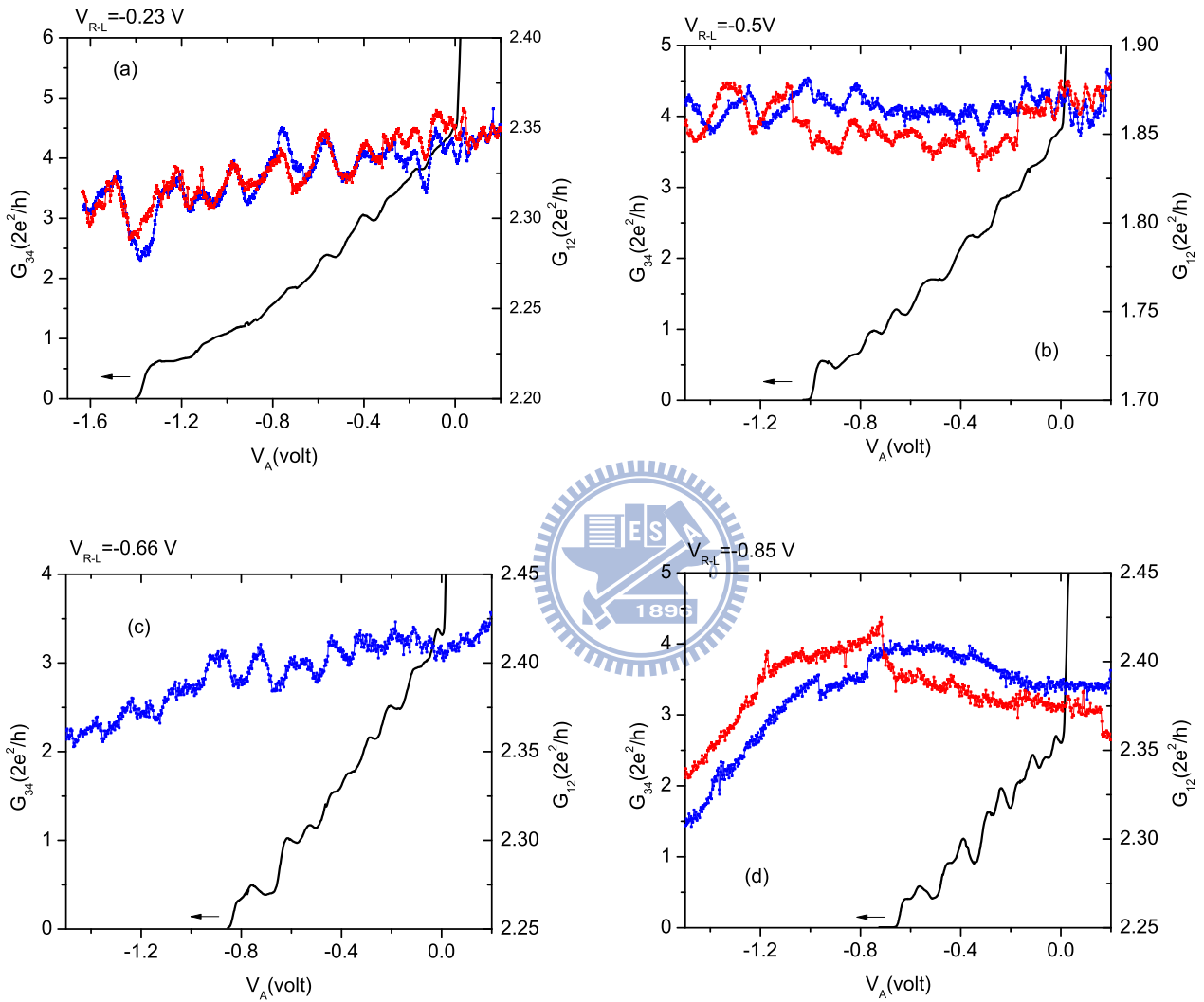


Figure A.2: Conductance of confinement C1, G_{12} and confinement C2, G_{34} as a function of V_A when the $0.8 \mu\text{m}$ QW is confined in various mode numbers N . $N =$ (a) 8, (b) 4, (c) 2 and (d) 0 (pinched off).

Appendix B

Fabrication Recipes

B.1 Photolithography, Wet etch, and Ohmic Contacts

Photolithography



1. Spin coat photoresist AZ5214E by two steps. 1000 rpm for 10 seconds, and 5000 rpm for 40 seconds.
2. **Prebake** Hardbake the on the hotplate at 90°C for 90 seconds.
3. **Exposure** 1.2-1.5 sec in 20 mW/cm² (i-line) and 30 mW/cm² (g-line).
4. **Reverse bake**: 120-125°C for 90 seconds.
5. **Flood exposure**: 20 mW/cm², 10-15 sec.
6. **Develop**. AZ400K:DI Water=1:4. Developing time~ 20-30 sec.

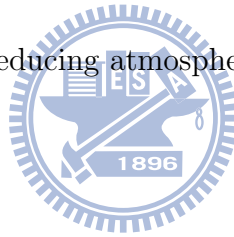
Wet Etching

Wet etch by $H_2SO_4 : H_2O_2 : H_2O = 1 : 8 : 160$ at ~ 4 °C.¹ Etch only a sufficient depth to evacuate the donor layer only. Do not evacuate the 2DEG layer (*shallow etch*) in case of leakage issues. For substrate 5-70, control the etched depth at ~ 500 – 600 Å.

¹The etch rate is ~ 18 Å/sec for GaAs. Notice that the etch rate differs for various layer structures.

Ohmic Contact

- Clean the impurities on the substrate by dipping in NH_4 solution(NH_4 :DI water=1:15) for 20 sec, clean by DI water, and blow dry.
- Photolithography-pattern transferring.
- Clean the residue resist by UV Ozone at 100°C for 2-3 mins.
- Before metal deposition, dip in HCl (HCl:DI water=1:1) for just a very short time. Clean it with DI water for about 30 sec, and blow dry.
- **Metal Deposition:** Materials from the bottom are Ni(10 nm)-Au(200nm)-Ge(100 nm)-Ni(70 nm).
- Lift-off.
- **Anneal** 450°C for 13 min² in reducing atmosphere of forming gas³.



Gate

Metal Deposition: Au/Ti=1500/100 Å

B.2 E-beam lithography

Resist and thin film thickness

In order to have better yield after the lift-off, the resist thickness should correspond to the desired thickness of thin film. The following tables give some favorite resist parameters.

Au/Ti=700/100 Å	
Coating	PMMA A5 6000rpm 30 sec(one step only)
Bake	~180°C 5min
Resist Thickness	~ 2100 Å

²450°C is the temperature on the controlling panel while the temperature on the quartz boat was measured to be ~ 430 °C.

³90% N₂ and 10% H₂.

Au/Ti=1000/100 Å	
Coating	6% PMMA (mw. 950K) 6000rpm 30 sec(one step only)
Bake	~180°C 5min
Resist Thickness	~ 3000 Å

Au/Ti=1800/100 Å	
Coating	10% PMMA (mw. 950K) 6000rpm 90 sec(one step)
Bake	~180°C 5min
Resist Thickness	~ 9500 Å

Standard operation procedures

1. Focus the beam with Au atoms
2. Set the dose set of pattern.
3. Adjust the beam current to 10pA.
4. Set "measure beam current" to the one measured by pico-amper meter with the electron beam being completely in Faraday Cup.
5. Tune the voltage of beam blander: set "beam off" and modify the voltage until the beam current is almost 0pA. Current leakage is not allowed.
6. Before process begins, turn off beam, change control switch to "NPGS" and "Slow4" in SEM program.
7. Process "Run file"

B.3 Insulating Layer

Exposing PMMA with electron beam with large enough dosage transforms PMMA into an insulator which solves neither in acetone nor in MIBK developer. The critical dosage of the transformation is roughly ~ 15 nC/cm.

Leakage

The resistance of the dielectric layer should be large enough to ensure good isolation between gates, otherwise heating of the sample during the measurement may happen.

From Fig.B.1, the resistance can be well above 100 GΩ. The tested resist is 5% PMMA.

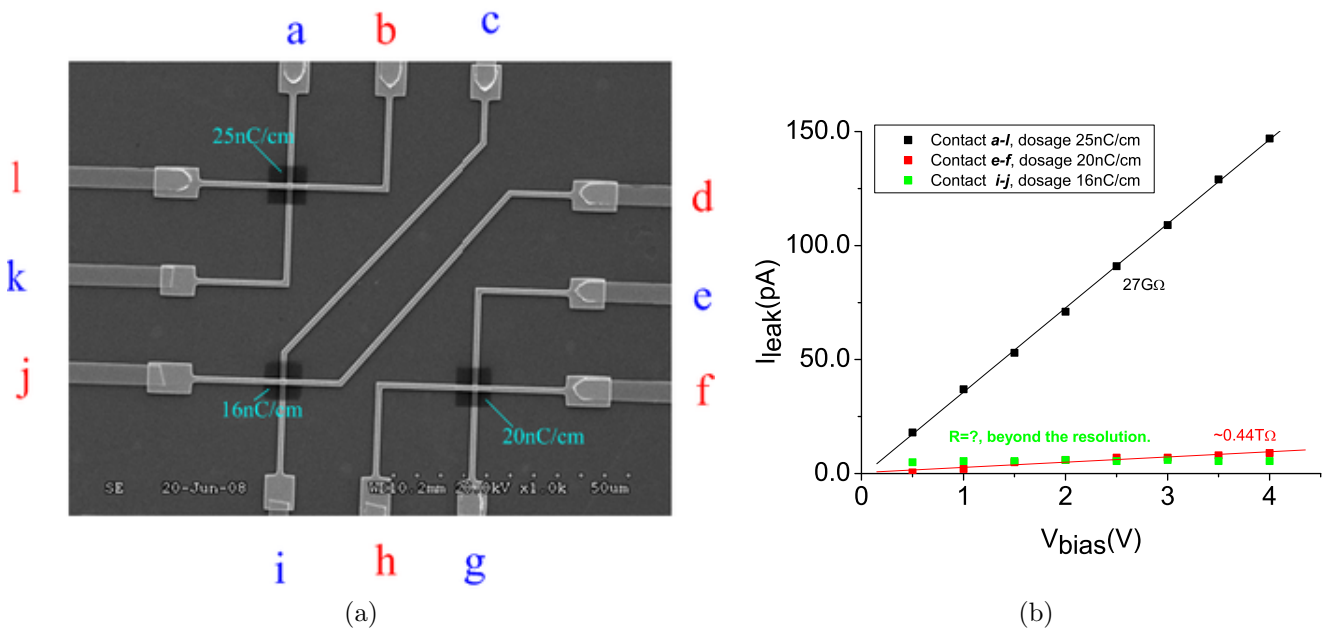
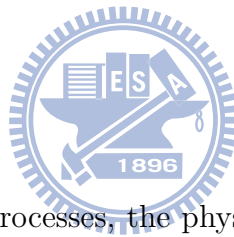


Figure B.1: (a) Layout of the device used to test the current leakage. (b) I-V of the insulating layers for different dosages at 77 K.



Thickness

Since the fabrication includes many processes, the physical structures of the devices are in three dimensions, such as metal gates climbing over a step of mesa. Cares should be taken on the step height for each process, otherwise broken leads or short circuit may happen. Fig.B.2 shows step height as a function of dosage.

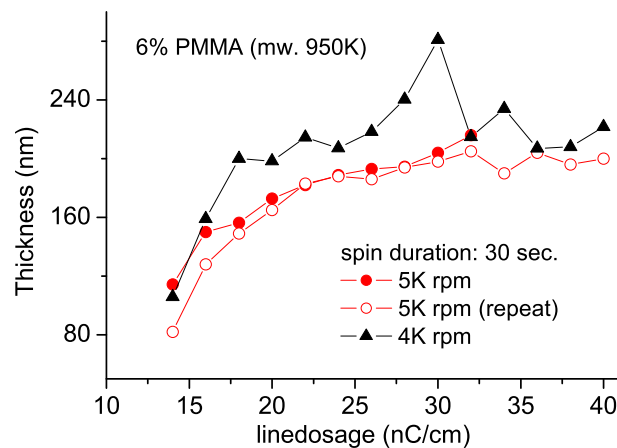


Figure B.2: Thickness of PMMA insulator as a function of exposed dosage.

Appendix C

Some Measurement Tips

C.1 Ground Loops

‘*Virtual ground*’ can induce very severe noises in the fine signal measurement. Although the electrical configurations seemed correct, it had taken plenty of time for us to figure out the workable grounding. The current fluctuations in our system can be as low as ~ 700 fA which guaranteed reliable measurement. One way to judge this criteria is that the *sensitivity* of Ithaco 1211 current preamplifier should be able to be set at the highest sensitivity, 10^{-12} A/V, without the overload indicator lightening. Poor grounding between instruments, cables, and the homemade electric circuit box leads to ground loops. Ground loops cause severe noises, as well as *cross talks* between instruments, and could completely ruin the data acquisitions. Great care should be taken on the ground loops. Notice that a large source drain bias V_{sd} , for instance a several meV dc V_{sd} applied across a device, would give the device a large dc current. In this case, the sensitivity can not reach as low as 10^{-12} A/V.

GPIB (General Purpose Interface Bus) and RS-232 are two generally default protocol for communications between instruments and x86 computers. However, the computer is easy to pick up subtle noises or signal pulses that may bring up discontinuity of data. The installation of isolators to isolate the electrical connections between the computer and instruments provides more stable signals. CP-114EL-I-DB9M manufactured by MOXA is the isolator for serial port (RS-232/422/485); GPIB-120A is the isolator for GPIB

manufactured by National Instruments. The electrical signals are bridged by electrical-optical converters.

C.2 Telegraph Noises

Another challenge for measurement of nano scale devices is the unavoidable impurities in semiconductors. Fixating all parameters such as gate voltages, magnetic field, and temperature, the conductance of devices as a function of time can show bistability at low temperatures. ‘*Deep centers*’ (or Deep defects) in semiconductors are believed to be the major cause of such telegraph noises (or switching noises). The occurrence of the ‘switching’ was somewhat stochastically, and was especially inclined to happen at low carrier densities. Based on experience, there are a couple of ways to alleviate the noises. One can exploit slow cooling (introduce a very small amount of exchange gas), and apply a small positive voltage on all gates during the cooling process. Although not systematically tested, it was found that either rapid cooling (the temperature reaches 77 K within half an hour, and reaches 4.2 K within another half hour), or cooling the devices without positively biasing the gates often ended with severe switching noises.

Appendix D

Device Inventory

2DEG

The following table presents the complete structure of 5-70 and 5-66 2DEG wafers. The density is $\sim 2.4 \times 10^{11} \text{ cm}^{-2}$ with mobility about $1.7 \times 10^6 \text{ cm}^2/\text{V} \cdot \text{s}$.

surface cap	GaAs	10 nm
gate barrier	37% AlGaAs	8 nm
doping layer (2.6×10^{18})	37% AlGaAs	15 nm
spacer	37% AlGaAs	60 nm
buffer layer	GaAs	1.5 μm

Table D.1: Structures of 2DEG 5-70 and 50-66.

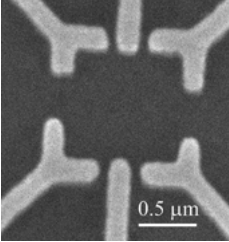
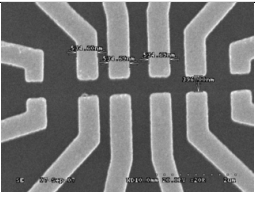
The following table presents the complete structure of 5-98 and 5-99 2DEG wafers. The density is $1.2 \sim 1.3 \times 10^{11} \text{ cm}^{-2}$ with mobility about $7 \times 10^5 \text{ cm}^2/\text{V} \cdot \text{s}$.

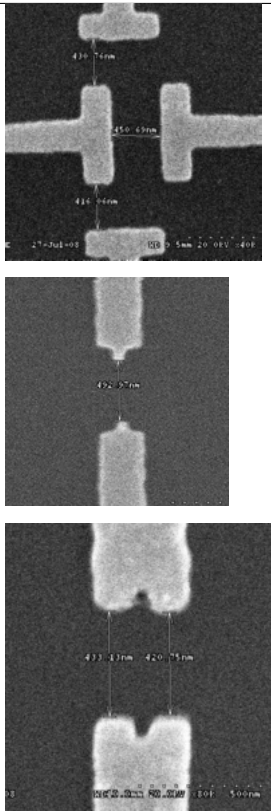
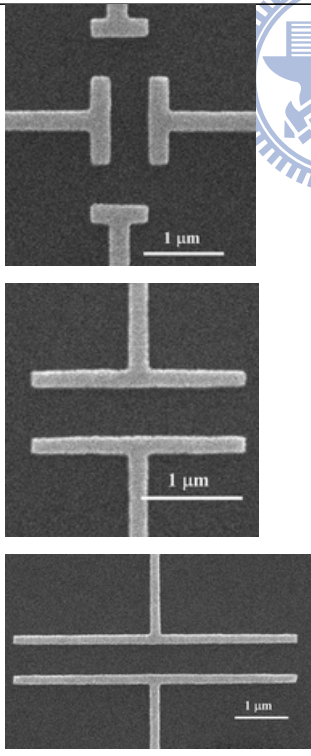
surface cap	GaAs	10 nm
gate barrier	36% AlGaAs	8 nm
doping layer (2.6×10^{18})	36% AlGaAs	15 nm
spacer	36% AlGaAs	50 nm
buffer layer	GaAs	1.5 μm

Table D.2: Structures of 2DEG 5-98 and 5-99.

Fabricated Devices

The devices that were studied are listed here.

Index	Layout	Subject(s)
5-70r-II2	Multi-gate chaotic quantum dots	Coulomb Blockade in QDs .
5-70r-I2	Pairs of split gates that are separated far way.	Transport in double QPCs in series.
5-70r-I2	Pairs of $0.5 \mu\text{m}$ long split gates with various edge to edge distances.	Transport in double QPCs in series
5-70t-II4, 5-70t-I2, 5-70t-I4, 6-102a-I2		Time-dependent fields generated dc currents in QDs. Disordered QWs. Scattering Effects on ZBA.
5-70aa-I2		Two QPCs in series. Scattering Effects on ZBA. Disordered QWs.

<p>5-70aa-II4</p>		<p>Scattering Effects on ZBA. Two coupled QPCs.</p>
<p>5-70ab-2</p>		<p>Scattering Effects on ZBA. Two coupled QPCs.</p>

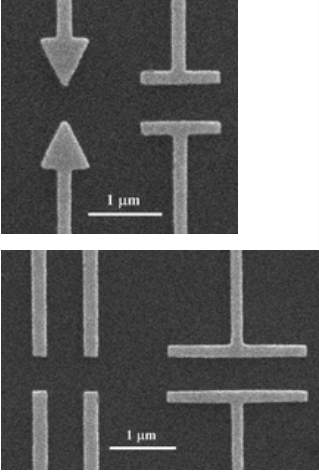
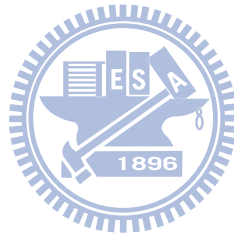
5-70ab-5		Scattering Effects on ZBA. Two coupled QPCs. Disordered QWs
5-70ab-4	square quantum dots with various sizes.	Coulomb blockade in QDs.

Table D.3: Device list.



Bibliography

- [1] J. Chelikowski, *Silicon: evolution and future of a technology*, Springer, 2004.
- [2] Z. Alferov, The history and future of semiconductor heterostructures from the point of view of a Russian scientist, *Physica Scripta T* **68**, 32 (1996).
- [3] K. v. Klitzing, G. Dorda, and M. Pepper, New Method for High-Accuracy Determination of the Fine-Structure Constant Based on Quantized Hall Resistance, *Phys. Rev. Lett.* **45**, 494 (1980).
- [4] S. Datta, *Electronic Transport in Mesoscopic Systems*, Cambridge University Press, 1995.
- [5] D. K. Ferry and S. M. Goodnick, *Transport in Nanostructures*, Cambridge University Press, 1997.
- [6] D. Yoshioka, *The Quantum Hall Effect*, volume 133 of *Solid-State Sciences*, Springer, 1998.
- [7] A. Yacoby, M. Heiblum, H. Shtrikman, V. Umansky, and D. Mahalu, Dephasing of ballistic electrons as a function of temperature and carrier density, *Semicond. Sci. Technol.* **9**, 907 (1994).
- [8] R. Landauer, Spatial Variation of Currents and Fields due to Localized Scatterers in Metallic Conduction, *IBM J. Res. Dev.* **1**, 233 (1957).
- [9] R. Landauer, Electrical Resistance of Disordered One-Dimensional Lattices, *Philos. Mag.* **21**, 863 (1970).



- [10] M. Büttiker, Y. Imry, R. Landauer, and S. Pinhas, Generalized many-channel conductance formula with application to small rings, *Phys. Rev. B* **31**, 6207 (1985).
- [11] Y. Takagaki, K. Gamo, S. Namba, S. Takaoka, K. Murase, and S. Ishida, Overshoot of four-terminal magnetoresistance at GaAs—AlGaAs narrow wire junctions, *Solid State Commun.* **71**, 809 (1989).
- [12] G. L. Timp and R. E. Howard, Quantum-mechanical aspects of transport in nano-electronics, *Proc. IEEE* **79**, 1188 (1991).
- [13] R. de Picciotto, H. Stormer, L. Pfeiffer, K. Baldwin, and K. West, Four-terminal resistance of a ballistic quantum wire, *Nature* **411**, 51 (2001).
- [14] B. J. van Wees, H. van Houten, C. W. J. Beenakker, J. G. Williamson, L. P. Kouwenhoven, D. van der Marel, and C. T. Foxon, Quantized conductance of point contacts in a two-dimensional electron gas, *Phys. Rev. Lett.* **60**, 848 (1988).
- [15] D. Wharam, T. Thornton, R. Newbury, M. Pepper, H. Ahmed, J. Frost, D. Hasko, D. Peacock, D. Ritchie, and G. Jones, One-dimensional transport and the quantization of the ballistic resistance, *J. Phys. C: Solid State Physics* **21**, L209 (1988).
- [16] D. M. Pozar, *Microwave Engineering*, John Wiley & Sons, 3rd edition, 2005.
- [17] J. C. Wu, M. N. Wybourne, W. Yindeepol, A. Weisshaar, and S. M. Goodnick, Interference phenomena due to a double bend in a quantum wire, *Appl. Phys. Lett.* **59**, 102 (1991).
- [18] J. C. Wu, M. N. Wybourne, A. Weisshaar, and S. M. Goodnick, Waveguide effects in quantum wires with double-bend discontinuities, *J. Appl. Phys.* **74**, 4590 (1993).
- [19] C. S. Chu and R. S. Sorbello, Effect of impurities on the quantized conductance of narrow channels, *Phys. Rev. B* **40**, 5941 (1989).
- [20] P. F. Bagwell, Evanescent modes and scattering in quasi-one-dimensional wires, *Phys. Rev. B* **41**, 10354 (1990).

- [21] J. A. Nixon and J. H. Davies, Potential fluctuations in heterostructure devices, *Phys. Rev. B* **41**, 7929 (1990).
- [22] J. A. Nixon, J. H. Davies, and H. U. Baranger, Breakdown of quantized conductance in point contacts calculated using realistic potentials, *Phys. Rev. B* **43**, 12638 (May 1991).
- [23] L. P. Kouwenhoven, B. J. van Wees, C. J. P. M. Harmans, J. G. Williamson, H. van Houten, C. W. J. Beenakker, C. T. Foxon, and J. J. Harris, Nonlinear conductance of quantum point contacts, *Phys. Rev. B* **39**, 8040 (1989).
- [24] N. K. Patel, L. Martin-Moreno, M. Pepper, R. Newbury, J. E. F. Frost, R. D. A., J. G. A. C., J. T. M. B. Janssen, J. Singleton, and J. A. A. J. Perenboom, Ballistic transport in one dimension: additional quantisation produced by an electric field, *Journal of Physics: Condensed Matter* **2**, 7247 (1990).
- [25] L. I. Glazman and A. V. Khaetskii, Nonlinear quantum conductance of a point contact, *Jetp Lett.* **48**, 591 (1988).
- [26] L. I. Glazman and A. V. Khaetskii, Nonlinear quantum conductance of a lateral microconstraint in a heterostructure, *Europhys. Lett.* **9**, 263 (1989).
- [27] N. K. Patel, J. T. Nicholls, L. Martin-Moreno, M. Pepper, J. E. F. Frost, D. A. Ritchie, and G. A. C. Jones, Evolution of half plateaus as a function of electric field in a ballistic quasi-one-dimensional constriction, *Phys. Rev. B* **44**, 13549 (1991).
- [28] L. Martin-Moreno, J. T. Nicholls, N. K. Patel, and M. Pepper, Non-linear conductance of a saddle-point constriction, *J. Phys.: Condens. Matter* **4**, 1323 (1992).
- [29] H. Grabert and M. H. Devoret, editors, *Single Charge Tunneling*, NATO ASI Series B294, New York, 1992, Plenum.
- [30] L. L. Sohn, L. P. Kouwenhoven, and G. Schön, editors, *Electron transport in quantum dots*, Kluwer Series E345, 1997.

- [31] Y. Alhassid, The statistical theory of quantum dots, *Rev. Mod. Phys.* **72**, 895 (2000).
- [32] L. P. Kouwenhoven, D. G. Austing, and S. Tarucha, Few-electron quantum dots, *Reports on Progress in Physics* **64**, 701 (2001).
- [33] R. Hanson, L. P. Kouwenhoven, J. R. Petta, S. Tarucha, and L. M. K. Vandersypen, Spins in few-electron quantum dots, *Rev. Mod. Phys.* **79**, 1217 (2007).
- [34] K. J. Thomas, J. T. Nicholls, M. Y. Simmons, M. Pepper, D. R. Mace, and D. A. Ritchie, Possible Spin Polarization in a One-Dimensional Electron Gas, *Phys. Rev. Lett.* **77**, 135 (1996).
- [35] D. J. Reilly, G. R. Facer, A. S. Dzurak, B. E. Kane, R. G. Clark, P. J. Stiles, R. G. Clark, A. R. Hamilton, J. L. O'Brien, N. E. Lumpkin, L. N. Pfeiffer, and K. W. West, Many-body spin-related phenomena in ultra low-disorder quantum wires, *Phys. Rev. B* **63**, 121311 (2001).
- [36] D. J. Reilly, T. M. Buehler, J. L. O'Brien, A. R. Hamilton, A. S. Dzurak, R. G. Clark, B. E. Kane, L. N. Pfeiffer, and K. W. West, Density-Dependent Spin Polarization in Ultra-Low-Disorder Quantum Wires, *Phys. Rev. Lett.* **89**, 246801 (2002).
- [37] S. M. Cronenwett, H. J. Lynch, D. Goldhaber-Gordon, L. P. Kouwenhoven, C. M. Marcus, K. Hirose, N. S. Wingreen, and V. Umansky, Low-Temperature Fate of the 0.7 Structure in a Point Contact: A Kondo-like Correlated State in an Open System, *Phys. Rev. Lett.* **88**, 226805 (2002).
- [38] R. Akis and D. K. Ferry, Simulations of spin filtering effects in a quantum point contact, *Journal of Physics: Condensed Matter* **20**, 164201 (2008).
- [39] A. A. Starikov, I. I. Yakimenko, and K. F. Berggren, Scenario for the 0.7-conductance anomaly in quantum point contacts, *Phys. Rev. B* **67**, 235319 (2003).

- [40] K. F. Berggren and I. I. Yakimenko, Effects of exchange and electron correlation on conductance and nanomagnetism in ballistic semiconductor quantum point contacts, *Phys. Rev. B* **66**, 085323 (2002).
- [41] P. Jaksch, I. Yakimenko, and K.-F. Berggren, From quantum point contacts to quantum wires: Density-functional calculations with exchange and correlation effects, *Phys. Rev. B* **74**, 235320 (2006).
- [42] A. Lassel, P. Schlagheck, and K. Richter, Effects of short-range interactions on transport through quantum point contacts: A numerical approach, *Phys. Rev. B* **75**, 045346 (2007).
- [43] P. Havu, M. J. Puska, R. M. Nieminen, and V. Havu, Electron transport through quantum wires and point contacts, *Phys. Rev. B* **70**, 233308 (2004).
- [44] D. J. Reilly, Phenomenological model for the 0.7 conductance feature in quantum wires, *Phys. Rev. B* **72**, 033309 (2005).
- [45] Y. Tokura and A. Khaetskii, Towards a microscopic theory of the 0.7 anomaly, *Physica E* **12**, 711 (2002).
- [46] K. A. Matveev, Conductance of a quantum wire at low electron density, *Phys. Rev. B* **70**, 245319 (2004).
- [47] K. A. Matveev, Conductance of a Quantum Wire in the Wigner-Crystal Regime, *Phys. Rev. Lett.* **92**, 106801 (2004).
- [48] Y. Meir, K. Hirose, and N. S. Wingreen, Kondo Model for the “0.7 Anomaly” in Transport through a Quantum Point Contact, *Phys. Rev. Lett.* **89**, 196802 (2002).
- [49] K. Hirose, Y. Meir, and N. Wingreen, Local moment formation in quantum point contacts, *Phys. Rev. Lett.* **90**, 026804 (2003).
- [50] T. Rejec and Y. Meir, Magnetic impurity formation in quantum point contacts, *Nature* **442**, 900 (2006).

- [51] J. H. Hsiao, K. M. Liu, S. Y. Hsu, and T. M. Hong, 0.7 anomaly due to the Rashba interaction in a nonuniform electric field, *Phys. Rev. B* **79**, 033304 (2009).
- [52] F. Sfigakis, C. J. B. Ford, M. Pepper, M. Kataoka, D. A. Ritchie, and M. Y. Simmons, Kondo effect from a tunable bound state within a quantum wire, *Phys. Rev. Lett.* **100**, 026807 (2008).
- [53] T. M. Chen, A. C. Graham, M. Pepper, I. Farrer, and D. A. Ritchie, Non-Kondo zero-bias anomaly in quantum wires, *Phys. Rev. B* **79**, 153303 (2009).
- [54] S. Sarkozy, F. Sfigakis, K. D. Gupta, I. Farrer, D. A. Ritchie, G. A. C. Jones, and M. Pepper, Zero-bias anomaly in quantum wires, *Phys. Rev. B* **79**, 161307 (2009).
- [55] A. Kristensen, H. Bruus, A. E. Hansen, J. B. Jensen, P. E. Lindelof, C. J. Marckmann, J. Nygård, C. B. Sørensen, F. Beuscher, A. Forchel, and M. Michel, Bias and temperature dependence of the 0.7 conductance anomaly in quantum point contacts, *Phys. Rev. B* **62**, 10950 (2000).
- [56] J. C. Chen, Y. Lin, K. T. Lin, T. Ueda, and S. Komiyama, Effects of impurity scattering on the quantized conductance of a quasi-one-dimensional quantum wire, *Appl. Phys. Lett.* **94**, 012105 (2009).
- [57] D. Hartmann, L. Worschech, and A. Forchel, Tunable magnetic-field asymmetry of nonlinear mesoscopic transport: Field-effect controlled backscattering in a quantum wire, *Phys. Rev. B* **78**, 113306 (2008).
- [58] L. P. Rokhinson, L. N. Pfeiffer, and K. W. West, Spontaneous Spin Polarization in Quantum Point Contacts, *Phys. Rev. Lett.* **96**, 156602 (2006).
- [59] K. Hirose, S. S. Li, and N. S. Wingreen, Mechanisms for extra conductance plateaus in quantum wires, *Phys. Rev. B* **63**, 033315 (2001).
- [60] A. C. Graham, K. J. Thomas, M. Pepper, N. R. Cooper, M. Y. Simmons, and D. A. Ritchie, Interaction Effects at Crossings of Spin-Polarized One-Dimensional Subbands, *Phys. Rev. Lett.* **91**, 136404 (2003).

- [61] A. C. Graham, M. Pepper, M. Y. Simmons, and D. A. Ritchie, Anomalous spin-dependent behavior of one-dimensional subbands, *Phys. Rev. B* **72**, 193305 (2005).
- [62] A. C. Graham, D. L. Sawkey, M. Pepper, M. Y. Simmons, and D. A. Ritchie, Energy-level pinning and the 0.7 spin state in one dimension: GaAs quantum wires studied using finite-bias spectroscopy, *Phys. Rev. B* **75**, 035331 (2007).
- [63] G. F. Giuliani and G. Vignale, *Quantum Theory of the Electron Liquid*, Cambridge University Press, 1st edition, 2005.
- [64] C. K. Wang and K.-F. Berggren, Spin splitting of subbands in quasi-one-dimensional electron quantum channels, *Phys. Rev. B* **54**, R14257 (1996).
- [65] L. DiCarlo, Y. Zhang, D. T. McClure, D. J. Reilly, C. M. Marcus, L. N. Pfeiffer, and K. W. West, Shot-Noise Signatures of 0.7 Structure and Spin in a Quantum Point Contact, *Phys. Rev. Lett.* **97**, 036810 (2006).
- [66] P. Roche, J. Ségala, D. C. Glatthli, J. T. Nicholls, M. Pepper, A. C. Graham, K. J. Thomas, M. Y. Simmons, and D. A. Ritchie, Fano Factor Reduction on the 0.7 Conductance Structure of a Ballistic One-Dimensional Wire, *Phys. Rev. Lett.* **93**, 116602 (2004).
- [67] K. J. Thomas, J. T. Nicholls, M. Pepper, W. R. Tribe, M. Y. Simmons, and D. A. Ritchie, Spin properties of low-density one-dimensional wires, *Phys. Rev. B* **61**, R13365 (2000).
- [68] K. S. Pyshkin, C. J. B. Ford, R. H. Harrell, M. Pepper, E. H. Linfield, and D. A. Ritchie, Spin splitting of one-dimensional subbands in high quality quantum wires at zero magnetic field, *Phys. Rev. B* **62**, 15842 (2000).
- [69] E. Wigner, On the Interaction of Electrons in Metals, *Phys. Rev.* **46**, 1002 (1934).
- [70] A. D. Klironomos, J. S. Meyer, and K. Matveev, Spontaneous spin polarization in quantum wires, *Europhys. Lett.* **74**, 679 (2006).

- [71] H. Bruus and K. Flensberg, *Many-Body Quantum Theory in Condensed Matter Physics*, Oxford University Press, 2004.
- [72] W. G. van der Wiel, S. D. Franceschi, T. Fujisawa, J. M. Elzerman, S. Tarucha, and L. P. Kouwenhoven, The Kondo Effect in the Unitary Limit, *Science* **289**, 2105 (2000).
- [73] T. Morimoto, Y. Iwase, N. Aoki, T. Sasaki, Y. Ochiai, A. Shailos, J. Bird, M. Lilly, J. Reno, and J. Simmons, Nonlocal resonant interaction between coupled quantum wires, *Appl. Phys. Lett.* **82**, 3952–3954 (2003).
- [74] J. P. Bird and Y. Ochiai, Electron Spin Polarization in Nanoscale Constrictions, *Science* **303**, 1621 (2004).
- [75] Y. Yoon, L. Mourokh, T. Morimoto, N. Aoki, Y. Ochiai, J. L. Reno, and J. P. Bird, Probing the Microscopic Structure of Bound States in Quantum Point Contacts, *Phys. Rev. Lett.* **99**, 136805 (2007).
- [76] V. I. Puller, L. G. Mourokh, A. Shailos, and J. P. Bird, Detection of Local-Moment Formation Using the Resonant Interaction between Coupled Quantum Wires, *Phys. Rev. Lett.* **92**, 096802 (2004).
- [77] G. Seelig and K. A. Matveev, Electron-Phonon Scattering in Quantum Point Contacts, *Phys. Rev. Lett.* **90**, 176804 (2003).
- [78] A. M. Lunde, A. De Martino, A. Schulz, R. Egger, and K. Flensberg, Electron-electron interaction effects in quantum point contacts, *New J. Phys.* **11**, 023031 (2009).
- [79] A. M. Lunde, K. Flensberg, and L. I. Glazman, Three-particle collisions in quantum wires: Corrections to thermopower and conductance, *Phys. Rev. B* **75**, 245418 (2007).
- [80] D. Meidan and Y. Oreg, Multiple-particle scattering in quantum point contacts, *Phys. Rev. B* **72**, 121312 (2005).

- [81] J. Rech, T. Micklitz, and K. A. Matveev, Conductance of Fully Equilibrated Quantum Wires, *Phys. Rev. Lett.* **102**, 116402 (2009).
- [82] T. Micklitz, J. Rech, and K. A. Matveev, Transport properties of partially equilibrated quantum wires, *Phys. Rev. B* **81**, 115313 (2010).
- [83] K. Aryanpour and J. E. Han, Ferromagnetic Spin Coupling as the Origin of 0.7 Anomaly in Quantum Point Contacts, *Phys. Rev. Lett.* **102**, 056805 (2009).
- [84] T. Giamarchi, *Quantum Physics in One Dimension*, Oxford University Press, 2003.
- [85] B. E. Kane, G. R. Facer, A. S. Dzurak, N. E. Lumpkin, R. G. Clark, L. N. Pfeiffer, and K. W. West, Quantized conductance in quantum wires with gate-controlled width and electron density, *Appl. Phys. Lett.* **72**, 3506 (1998).
- [86] K. M. Liu, H. I. Lin, V. Umansky, and S. Y. Hsu, Carrier density dependent electric transport of serially connected two quantum point contacts, *Physica E: Low-Dimensional Systems and Nanostructures* **42**, 1122 (2010).
- [87] B. L. Altshuler and A. G. Aronov, Zero bias anomaly in tunnel resistance and electron-electron interaction, *Solid State Commun.* **30**, 115 (1979).
- [88] T. Morimoto, M. Henmi, R. Naito, K. Tsubaki, N. Aoki, J. P. Bird, and Y. Ochiai, Resonantly Enhanced Nonlinear Conductance in Long Quantum Point Contacts near Pinch-Off, *Phys. Rev. Lett.* **97**, 096801 (2006).
- [89] E. J. Koop, A. I. Lerescu, J. Liu, B. J. Van Wees, D. Reuter, A. D. Wieck, and C. H. Van Der Wal, The influence of device geometry on many-body effects in quantum point contacts: Signatures of the 0.7 anomaly, exchange and Kondo, *J. Supercond. Nov. Magn* **20**, 433 (2007).
- [90] H. Bruus, V. Cheianov, and K. Flensberg, The anomalous 0.5 and 0.7 conductance plateaus in quantum point contacts, *Physica E* **10**, 97 (2001).

- [91] D. Schmeltzer, A. Saxena, A. R. Bishop, and D. L. Smith, Electron transmission through a short interacting wire: 0.7 conductance anomaly, *Phys. Rev. B* **71**, 045429 (2005).
- [92] J. Rech and K. A. Matveev, Resistivity of Inhomogeneous Quantum Wires, *Phys. Rev. Lett.* **100**, 066407 (2008).
- [93] D. van der Marel and E. G. Haanappel, Model calculations of the quantum ballistic transport in two-dimensional constriction-type microstructures, *Phys. Rev. B* **39**, 7811 (1989).
- [94] K. Nikolić and A. MacKinnon, Conductance and conductance fluctuations of narrow disordered quantum wires, *Phys. Rev. B* **50**, 11008 (1994).
- [95] T. T. N. and B. G.A.D., Effects of compositional impurities and width variation on the conductance of a quantum wire, *J. Phys.: Condens. Matter* **6**, 2559 (1994).
- [96] S. A. Gurvitz and Y. B. Levinson, Resonant reflection and transmission in a conducting channel with a single impurity, *Phys. Rev. B* **47**, 10578 (1993).
- [97] P. McEuen, B. Alphenaar, R. Wheeler, and R. Sacks, Resonant transport effects due to an impurity in a narrow constriction, *Surf. Sci.* **229**, 312 (1990).
- [98] E. Tekman and S. Ciraci, Theoretical study of transport through a quantum point contact, *Phys. Rev. B* **43**, 7145 (1991).
- [99] Y. B. Levinson, M. I. Lubin, and E. V. Sukhorukov, Short-range impurity in a saddle-point potential: Conductance of a microjunction, *Phys. Rev. B* **45**, 11936 (1992).
- [100] J. H. Bardarson, I. Magnusdottir, G. Gudmundsdottir, C. S. Tang, A. Manolescu, and V. Gudmundsson, Coherent electronic transport in a multimode quantum channel with Gaussian-type scatterers, *Phys. Rev. B* **70**, 245308 (2004).

- [101] V. Vargiamidis and H. M. Polatoglou, Conductance of a quantum wire with a Gaussian impurity potential and variable cross-sectional shape, *Phys. Rev. B* **71**, 075301 (2005).
- [102] Y. Takagaki and D. K. Ferry, Conductance of quantum point contacts in the presence of disorder, *Phys. Rev. B* **46**, 15218 (1992).
- [103] D. R. Mace, M. P. Grimshaw, D. A. Ritchie, C. J. B. Ford, M. Pepper, and G. A. C. Jones, Electron conduction characteristics of split-gate structures fabricated on pseudomorphic GaAs-In_xGa_{1-x}As-AlGaAs heterostructures, *J. Phys.: Condes. Matter* **5**, L227 (1993).
- [104] R. J. Brown, M. J. Kelly, R. Newbury, M. Pepper, B. Miller, H. Ahmed, D. G. Hasko, D. C. Peacock, D. A. Ritchie, J. E. F. Frost, and G. A. C. Jones, The one dimensional quantised ballistic resistance in GaAs/AlGaAs heterojunctions with varying experimental conditions, *Solid-State Electronics* **32**, 1179 (1989).
- [105] Y. Takagaki and D. K. Ferry, Double quantum point contacts in series, *Phys. Rev. B* **45**, 13494 (1992).
- [106] T. Y. and F. D. K., Conductance of quantum waveguides with a rough boundary, *J. Phys.: Condes. Matter* **4**, 10421 (1992).
- [107] D. Csontos and H. Xu, Effects of boundary roughness on the conductance of quantum wires, *App. Phys. Lett.* **77**, 2364 (2000).
- [108] F. Wakaya, J. Takahara, S. Takaoka, K. Murase, and K. Gamo, Confinement potential in an asymmetrically biased quantum point contact, *Jpn. J. Appl. Phys.* **35**, 1329 (1996).
- [109] L. I. Glazman and I. A. Larkin, Lateral position control of an electron channel in a split-gate device, *Semicond. Sci. Technol.* **6**, 32 (1991).

- [110] D. H. Cobden, N. K. Patel, M. Pepper, D. A. Ritchie, J. E. F. Frost, and G. A. C. Jones, Noise and reproducible structure in a GaAs/Al_xGa_{1-x}As one-dimensional channel, *Phys. Rev. B* **44**, 1938 (1991).
- [111] D. H. Cobden, A. Savchenko, M. Pepper, N. K. Patel, D. A. Ritchie, J. E. F. Frost, and G. A. C. Jones, Time-irreversible random telegraph signal due to current along a single hopping chain, *Phys. Rev. Lett.* **69**, 502 (1992).
- [112] T. Sakamoto, Y. Nakamura, and K. Nakamura, Distributions of single-carrier traps in GaAs/Al_xGa_{1-x}As heterostructures, *Appl. Phys. Lett.* **67**, 2220 (1995).
- [113] M. P. Jura, M. A. Topinka, L. Urban, A. Yazdani, H. Shtrikman, L. N. Pfeiffer, K. W. West, and D. Goldhaber-Gordon, Unexpected features of branched flow through high-mobility two-dimensional electron gases, *Nat. Phys.* **3**, 841 (2007).
- [114] K. M. Liu, V. Umansky, and S. Y. Hsu, Effect of scattering on zero-bias anomaly and conductance reduction in quasi-one-dimensional quantum wires, *Phys. Rev. B* **81**, 235316 (2010).
- [115] P. E. Lindelof and M. Aagesen, Measured deviations from the saddle potential description of clean quantum point contacts, *J. Phys.: Condens. Matter* **20**, 164207 (2008).
- [116] B. L. Altshuler and L. I. Glazman, Pumping electrons, *Science* **283**, 1864 (1999).
- [117] L. P. Kouwenhoven, A. T. Johnson, N. C. van der Vaart, C. J. P. M. Harmans, and C. T. Foxon, Quantized current in a quantum-dot turnstile using oscillating tunnel barriers, *Phys. Rev. Lett.* **67**, 1626 (1991).
- [118] M. D. Blumenthal, B. Kaestner, L. Li, S. Giblin, T. J. B. M. Janssen, M. Pepper, D. Anderson, G. Jones, and D. A. Ritchie, Gigahertz quantized charge pumping, *Nat. Phys.* **3**, 343 (2007).
- [119] P. W. Brouwer, Scattering approach to parametric pumping, *Phys. Rev. B* **58**, R10135 (1998).

- [120] M. Switkes, C. M. Marcus, K. Campman, and A. C. Gossard, An adiabatic quantum electron pump, *Science* **283**, 1905 (1999).
- [121] P. W. Brouwer, Rectification of displacement currents in an adiabatic electron pump, *Phys. Rev. B* **63**, 121303 (2001).
- [122] L. DiCarlo, C. M. Marcus, and J. S. Harris, Photocurrent, Rectification, and Magnetic Field Symmetry of Induced Current through Quantum Dots, *Phys. Rev. Lett.* **91**, 246804 (2003).
- [123] M. G. Vavilov, L. DiCarlo, and C. M. Marcus, Photovoltaic and rectification currents in quantum dots, *Phys. Rev. B* **71**, 241309 (2005).
- [124] E. M. Höhberger, A. Lorke, W. Wegscheider, and M. Bichler, Adiabatic pumping of two-dimensional electrons in a ratchet-type lateral superlattice, *Appl. Phys. Lett.* **78**, 2905 (2001).
- [125] T. Müller, A. Würtz, A. Lorke, D. Reuter, and A. D. Wieck, Wave-form sampling using a driven electron ratchet in a two-dimensional electron system, *Appl. Phys. Lett.* **87**, 042104 (2005).
- [126] A. S. Sedra and K. C. Smith, *Microelectronic Circuits*, Oxford University Press, 5th edition, 2004, chap. 3.
- [127] R. E. Ziemer and W. H. Tranter, *Principles of Communications*, John Wiley & Sons, 4th edition, 1995, chap. 3.
- [128] J. N. H. J. Cremers and P. W. Brouwer, Dephasing in a quantum pump, *Phys. Rev. B* **65**, 115333 (2002).
- [129] C. S. Tang, Y. H. Tan, and C. S. Chu, Transport spectroscopy in a time-modulated open quantum dot, *Phys. Rev. B* **67**, 205324 (2003).
- [130] E. Faizabadi and F. Ebrahimi, Charge pumping in quantum wires, *J. Phys.: Condens. Matter* **16**, 1789 (2004).

- [131] S. Banerjee, A. Mukherjee, S. Rao, and A. Saha, Adiabatic charge pumping through a dot at the junction of N quantum wires, *Phys. Rev. B* **75**, 153407 (2007).
- [132] M. Moskalets and M. Büttiker, Effect of inelastic scattering on parametric pumping, *Phys. Rev. B* **64**, 201305 (2001).
- [133] A. M. Chang, H. U. Baranger, L. N. Pfeiffer, and K. W. West, Weak Localization in Chaotic versus Nonchaotic Cavities: A Striking Difference in the Line Shape, *Phys. Rev. Lett.* **73**, 2111 (1994).
- [134] A. G. Huibers, M. Switkes, C. M. Marcus, K. Campman, and A. C. Gossard, Dephasing in Open Quantum Dots, *Phys. Rev. Lett.* **81**, 200 (1998).
- [135] B. J. van Wees, E. M. M. Willems, C. J. P. M. Harmans, C. W. J. Beenakker, H. van Houten, J. G. Williamson, C. T. Foxon, and J. J. Harris, Anomalous integer quantum Hall effect in the ballistic regime with quantum point contacts, *Phys. Rev. Lett.* **62**, 1181 (1989).
- [136] C. W. J. Beenakker and H. v. Houten, Magnetotransport and nonadditivity of point-contact resistances in series, *Phys. Rev. B* **39**, 10445 (1989).
- [137] P. Beton, B. Snell, P. Main, A. Neves, J. Owers-Bradley, L. Eaves, M. Henini, O. Hughes, S. Beaumont, and C. Wilkinson, The resistance of two quantum point contacts in series, *J. Phys.: Condens. Matter* **1**, 7505 (1989).
- [138] D. A. Wharam, M. Pepper, H. Ahmed, J. E. F. Frost, D. G. Hasko, D. C. Peacock, D. A. Ritchie, and G. A. C. Jones, Addition of the one-dimensional quantised ballistic resistance, *J. Phys. C: Solid State Phys.* **21**, L887 (1988).
- [139] L. P. Kouwenhoven, B. J. van Wees, W. Kool, C. J. P. M. Harmans, A. A. M. Staring, and C. T. Foxon, Transition from Ohmic to adiabatic transport in quantum point contacts in series, *Phys. Rev. B* **40**, 8083 (1989).

- [140] R. P. Taylor, A. S. Sachrajda, J. A. Adams, P. T. Coleridge, and P. Zawadzki, Zero- and low-magnetic-field transport characterization of $\text{Al}_x\text{Ga}_{1-x}\text{As}/\text{GaAs}$ lateral dots, *Phys. Rev. B* **47**, 4458 (1993).
- [141] W. R. Chen, Electrical transport in multiple gated quantum point contacts, Master's thesis, National Chiao Tung University, Taiwan, 2005.
- [142] I. Zailer, J. Frost, V. Chabasseur-Molyneux, C. Ford, and M. Pepper, Crosslinked PMMA as a high-resolution negative resist for electron beam lithography and applications for physics of low-dimensional structures, *Semicond. Sci. Technol.* **11**, 1235 (1996).
- [143] A. E. Hansen, A. Kristensen, S. Pedersen, C. B. Sørensen, and P. E. Lindelof, Mesoscopic decoherence in Aharonov-Bohm rings, *Phys. Rev. B* **64**, 045327 (2001).
- [144] Y. Yamauchi, M. Hashisaka, S. Nakamura, K. Chida, S. Kasai, T. Ono, R. Leturcq, K. Ensslin, D. C. Driscoll, A. C. Gossard, and K. Kobayashi, Universality of bias- and temperature-induced dephasing in ballistic electronic interferometers, *Phys. Rev. B* **79**, 161306 (2009).
- [145] D. T. McClure, Y. Zhang, B. Rosenow, E. M. Levenson-Falk, C. M. Marcus, L. N. Pfeiffer, and K. W. West, Edge-State Velocity and Coherence in a Quantum Hall Fabry-Pérot Interferometer, *Phys. Rev. Lett.* **103**, 206806 (2009).
- [146] A. Geim, Graphene: Status and prospects, *Science* **324**, 1530 (2009).
- [147] F. Schwierz, Graphene transistors, 2010, online publication.
- [148] A. K. Geim and K. S. Novoselo, The rise of graphene, *Nat. Material* **6**, 183 (2007).
- [149] Y. Yoon, M.-G. Kang, P. Ivanushkin, T. Mourokh, L. abd Morimoto, N. Aoki, J. Reno, Y. Ochiai, and J. Bird, Nonlocal bias spectroscopy of the self-consistent bound state in quantum point contacts near pinch off, *Appl. Phys. Lett.* **94**, 213103 (2009).

- [150] A. Ramamoorthy, L. Mourokh, J. L. Reno, and J. P. Bird, Tunneling spectroscopy of a ballistic quantum wire, *Phys. Rev. B* **78**, 035335 (2008).
- [151] K. J. Thomas, J. T. Nicholls, M. Y. Simmons, W. R. Tribe, A. G. Davies, and M. Pepper, Controlled wave-function mixing in strongly coupled one-dimensional wires, *Phys. Rev. B* **59**, 12252 (1999).
- [152] S. Fischer, G. Apetrii, U. Kunze, D. Schuh, and G. Abstreiter, Energy spectroscopy of controlled coupled quantum-wire states, *Nature Physics* **2**, 91 (2006).
- [153] G. Salis, T. Heinzel, K. Ensslin, O. J. Homan, W. Bächtold, K. Maranowski, and A. C. Gossard, Mode spectroscopy and level coupling in ballistic electron waveguides, *Phys. Rev. B* **60**, 7756 (1999).

